Long-Term Monitoring of Atmospheric Water Vapor and Methane

Petra Hausmann

KIT-Campus Alpin
IMK-IFU: Atmospheric Environmental Research

Long-Term Monitoring of Atmospheric Water Vapor and Methane

Petra Hausmann

Dissertation
in Climate and Environmental Sciences

submitted to the
Faculty of Applied Computer Science
University of Augsburg

by Petra Hausmann

July 2017

First Reviewer:	PD Dr. Ralf Sussmann, KIT/IMK-IFU
Second Reviewer:	Prof. Dr. Jucundus Jacobeit, University of Augsburg
Date of Oral Exam:	19 July 2017

You must be the change
you wish to see in the world.

Mahatma Gandhi

Kurzfassung

Eine der größten globalen Herausforderungen, die es zu bewältigen gilt, ist die Begrenzung des vom Menschen verursachten Klimawandels. Hierfür ist es erforderlich, den anthropogenen Ausstoß von Treibhausgasen nachhaltig zu verringern. In der Erdatmosphäre absorbieren Treibhausgase einen Teil der Infrarotstrahlung, indem die Gasmoleküle zu höherenergetischen Schwingungs- und Rotationszuständen angeregt werden. Erhöht sich die Konzentration dieser Spurengase, nimmt das Wärmerückhaltevermögen der Atmosphäre zu und es kommt zur globalen Erwärmung. Um die anthropogenen Emissionen wirksam zu senken, benötigen wir detailliertes Wissen über Trends, Budgets und Transport von Treibhausgasen in der Atmosphäre. In diesem Zusammenhang leistet die vorliegende Dissertation einen wesentlichen Beitrag zu einem verbesserten Verständnis hinsichtlich der wichtigen Treibhausgase Wasserdampf und Methan. Der Schwerpunkt der vorgestellten Untersuchungen liegt dabei in der Auswertung von Langzeit-Messungen, die mittels solarer Absorptionsspektrometrie am Gipfelobservatorium Zugspitze (47.42° N, 10.98° E; 2964 m ü. NN) durchgeführt wurden.

Seit Beginn der Industrialisierung hat sich die weltweite Konzentration von Methan, dem zweitwichtigsten anthropogenen Treibhausgas, mehr als verdoppelt. Nach einer Periode der Stagnation (1999–2006) ist seit 2007 erneut ein starker Anstieg zu beobachten. Die Quellenzuordnung dieser Trends wird erschwert durch die große Vielfalt an Methan-Quellen, die sowohl natürlichen (z.B. Sümpfe, geologische Ausgasungen, Waldbrände) als auch anthropogenen Ursprung haben (z.B. Förderung fossiler Energieträger, Viehhaltung, Reisanbau). Aktuelle Studien identifizieren zwei Hauptursachen für den neuerlichen Methan-Anstieg: steigende Emissionen durch natürliche Feuchtgebiete und durch die Gewinnung fossiler Brennstoffe. Deren relativer Beitrag konnte jedoch noch nicht ausreichend quantifiziert werden. Im Rahmen der vorliegenden Dissertation gelingt es mit Hilfe eines innovativen Ansatzes den Beitrag von Emissionen der Erdöl- und Erdgasförderung zum erneuten Methan-Zuwachs abzuschätzen. Dabei werden Langzeit-Trends von Methan in Relation gesetzt zu Zeitserien von Ethan – einem Indikator für fossile Methan-Emissionen. Aufgrund der geringen Variabilität von säulen-gemitteltem Methan sind hochgenaue Messungen für die korrekte Trendanalyse unabdingbar. In diesem Kontext kommt eine neue Korrekturmethode zum Einsatz, um Messfehler zu eliminieren, die sich aus Ungenauigkeiten in der Ausrichtung des Spektrometers auf die Sonne ergeben. Um die so abgeleiteten Methan- und Ethan-Trends an der Zugspitze sowie an einer Referenzstation auf der Südhalbkugel zu simulieren, wird ein atmosphärisches Zwei-Box-Modell entwickelt. Dieses Modell erlaubt es darüber hinaus, die beobachteten Trends optimierten Emissionsszenarien zuzuordnen. Das zentrale Resultat dieser Simulationen zeigt, dass der erneute Methan-Anstieg seit 2007 zu einem signifikanten Anteil von mindestens 39 % durch Öl- und Gas-Emissionen verursacht wurde.

Neben Methan spielt Wasserdampf als dominantes natürliches Treibhausgas eine Schlüsselrolle im Energiehaushalt der Erde. Durch die positive Rückkopplung zwischen Wasserdampfgehalt und Lufttemperatur trägt Wasserdampf zudem wesentlich zur Verstärkung der anthropogenen Erderwärmung bei. Mit voranschreitendem Klimawandel werden auch Änderungen atmosphärischer Zirkulationsmuster prognostiziert. Wertvolle Informationen über die zugrundeliegenden Transportprozesse können aus Wasserdampf-Isotopen-Messungen gewonnen werden. In diesem Zusammenhang erforscht die vorliegende Dissertation, inwieweit derartige Messungen an der Zugspitze neue Einblicke in Transportprozesse nach Mitteleuropa erlauben. Mit Hilfe umfangreicher Simulationen von Rückwärtstrajektorien gelingt es, für bestimmte Isotopen-Zusammensetzungen verschiedene Transportwege zu identifizieren, auf denen Wasserdampf in die freie Troposphäre über Mitteleuropa gelangt. Neben dem Transport von Wasserdampf sind Ferntransport-Prozesse maßgeblich für den Import verschiedener Spurenstoffe (z.B. Aerosole, Ozon) nach Mitteleuropa verantwortlich und beeinflussen somit das regionale Klima sowie Luftqualität und Gesundheit. Für die hier untersuchten Ferntransport-Kategorien (stratosphärische Intrusionen, interkontinentaler Transport von Nordamerika und Nordafrika) ergeben sich signifikant unterschiedliche Signaturen in der Verteilung der Wasserdampf-Isotopen-Messungen an der Zugspitze. Zur erfolgreichen Validierung dieses auf Trajektorien basierten Resultats werden Lidar- und In-situ-Messungen herangezogen, die Aufschluss über Transport-Ereignisse in die nordalpine Region geben. Die erzielten Ergebnisse verdeutlichen das Potential von Wasserdampf-Isotopen-Messungen für die systematische Erfassung und Erforschung von atmosphärischen Transportprozessen. Dies ist insbesondere wichtig, um klimabedingte Änderungen im globalen Wasser-Kreislauf besser zu verstehen und internationale Vereinbarungen über Treibhausgas-Emissionen zu kontrollieren. Somit tragen die Ergebnisse dieser Dissertation dazu bei, konkrete Schritte zur Umsetzung des 2016 in Kraft getretenen Klimaabkommens von Paris zu definieren.

Abstract

Mitigation of climate change demands a high priority and requires a sustained reduction of anthropogenic greenhouse gas emissions. In the Earth's atmosphere, greenhouse gases substantially absorb infrared radiation by molecular transitions to higher-energy vibration and rotation states. If atmospheric concentrations of these trace gases increase, the amount of radiation energy lost to space is diminished, resulting in global warming. To develop effective strategies for emission reduction, it is essential to gain an accurate understanding of greenhouse gas budgets, trends, and atmospheric transport processes. In this context, the present dissertation contributes to improving our knowledge with regard to two major greenhouse gases – water vapor and methane. Investigations performed focus on the long-term monitoring of these trace gases by means of solar absorption spectrometry at the high-altitude observatory Zugspitze (47.42° N, 10.98° E; 2964 m a.s.l.).

The global concentration of methane – the second most important anthropogenic greenhouse gas – has more than doubled since preindustrial times. After a period of near-zero growth (1999–2006), a renewed methane increase has been observed since 2007. The source attribution of these trends is highly complex due to the large variety of methane sources, which have either natural (e.g., wetlands, geologic seepage, forest fires) or anthropogenic origins (e.g., fossil fuel production, livestock farming, rice cultivation). Recent studies provide evidence that the renewed methane increase is primarily driven by increasing emissions from natural wetlands and from the production of fossil fuels. However, the relative contribution of these two drivers has not yet been accurately quantified. In the present dissertation, an innovative approach is employed to estimate the contribution of oil and natural gas emissions to the renewed methane increase. For this purpose, long-term trends of methane are assessed in relation to time series of ethane – an indicator for fossil-fuel methane emissions. Methane trend analysis requires highly precise measurements due to the low variability of column-averaged methane. In this context, a novel correction method is applied to eliminate errors that are caused by inaccuracies in the alignment of the spectrometer to the solar disk. The resulting methane and ethane trends at Mt. Zugspitze and at a reference site in the Southern Hemisphere are simulated with the help of an atmospheric two-box model developed within the scope of this dissertation. This model enables the assignment of observed trends to optimized emission scenarios. Simulations performed reveal that oil and natural gas emissions have significantly contributed by at least 39 % to the renewed methane increase since 2007.

In addition to methane, water vapor plays a key role in the Earth's energy budget. Water vapor is not only the dominant natural greenhouse gas, but also enhances anthropogenic climate forcing due to the positive feedback between water vapor concentration and air temperature. Under changing climate conditions, patterns of atmospheric circulation

are expected to be modified as well. Valuable information on the underlying transport processes can be obtained from observations of water vapor and its isotopic composition. In that context, the present dissertation investigates to what extent water vapor isotope measurements at Mt. Zugspitze provide further insight into transport processes to Central Europe. Based on extensive backward trajectory simulations, different moisture transport patterns to the Central European free troposphere are identified for distinct water vapor isotopic compositions. In addition to the transport of water vapor, long-range transport processes are responsible for the import of various trace species (e.g., ozone, aerosols) to Central Europe and, therefore, affect regional climate, air quality and human health. Significantly different signatures in the distribution of water vapor isotope measurements are found for the long-range transport categories considered: stratospheric intrusions, intercontinental transport from North America, and transport from Northern Africa. For the successful validation of this trajectory-based result, lidar and in situ measurements are analyzed, which reveal transport events reaching the Northern Alps. These findings highlight the potential of water vapor isotope measurements for a systematic recording and investigation of atmospheric transport processes. This is of particular importance to enhance our understanding of climate-induced changes in the global water cycle, as well as to control international treaties on emission regulations. Consequently, results achieved within the scope of this dissertation can contribute to define specific steps for the implementation of the Paris Climate Agreement, which was ratified in 2016.

Contents

Chapter 1

Introduction

1.1 Background and Motivation

> *"I'm convinced that we'll solve the climate crisis, but the longer we take, the more grave the risks we're taking with humankind."*
>
> — Al Gore, Nobel Peace Prize 2007

Warming of the Earth's climate system is unequivocal. On global average, surface temperature increased by 0.85 °C in the period from 1880 to 2012. According to the latest assessment report of the Intergovernmental Panel on Climate Change (IPCC, 2013), the dominant driver of global warming is the increase in atmospheric greenhouse gas concentrations due to human activities. Anthropogenic emissions have substantially enhanced the natural greenhouse effect. Continued greenhouse gas emissions will result in further warming and in altering various components of our climate system, including the activation of feedback mechanisms in response to climate change.

At the Paris climate conference in December 2015, a historic global climate deal was adopted, which has already entered into force in November 2016. In the Paris Agreement governments of 195 countries agreed to limit the global temperature increase well below 2 °C relative to preindustrial levels to avoid negative impacts of climate change. This aim will require substantial and sustained reductions of greenhouse gas emissions. Therefore, national climate action plans will be set and regularly strengthened starting in 2020. Additionally, for the second commitment period of the Kyoto Protocol (2013–2020), 38 countries have taken on binding targets to reduce their greenhouse gas emissions by 20 % compared to 1990 – a treaty that has not yet been ratified by all parties (UNFCCC, 2016). Reduction strategies focus on anthropogenic emissions of well-mixed greenhouse gases including carbon dioxide (CO_2), methane (CH_4), and nitrous oxide (N_2O), among others.

Greenhouse gases play an important role in variations of the global energy budget, which govern climate change. Under present-day climate conditions, the global mean energy budget is not balanced (Stephens et al., 2012; Wild et al., 2013), as illustrated in Fig. 1.1. Radiative forcing is a measure for the net change in the Earth's energy balance in response to an external perturbation. As the total radiative forcing induced by all drivers of climate change is positive, energy is taken up by the Earth's climate system resulting in global warming. The major inflow of energy entering the system is due to incoming solar radiation.

As the Earth's atmosphere is relatively transparent to shortwave radiation, it is largely transmitted to the Earth's surface, whereas minor parts are absorbed in the atmosphere or are reflected back to space. In contrast, the atmosphere is less transparent with respect to thermal radiation emitted by the Earth's surface. This longwave radiation can only partially escape to space as it interacts with atmospheric constituents including clouds, aerosols, and greenhouse gases. The molecular structure of these gases enables them to absorb radiation in certain spectral regions. Atmospheric components re-emit thermal radiation in all directions and at lower temperatures than at the Earth's surface, which implies a downward longwave flux component and diminishes the amount of outgoing longwave radiation escaping to space. This fundamental mechanism in the Earth's atmosphere is known as greenhouse effect and is responsible for the prevailing moderate surface temperatures, which facilitate life on Earth. The energy budget of the atmosphere is closed by turbulent fluxes of sensible and latent heat related to the global hydrological cycle.

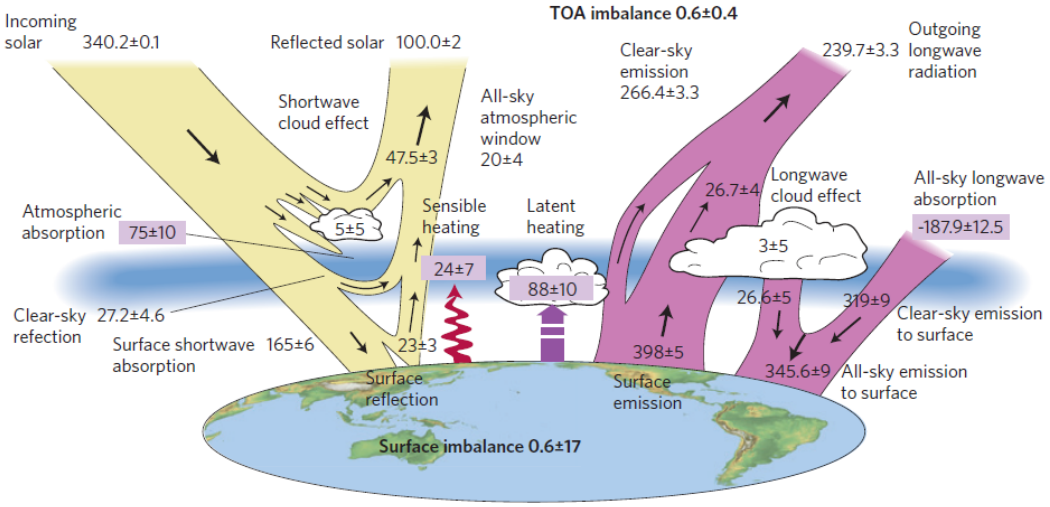

Figure 1.1: Global annual mean energy budget of the Earth under present-day climate conditions (2000–2010). All flux estimates are given in $\mathrm{W\,m^{-2}}$. Solar fluxes are depicted in yellow and longwave (infrared) fluxes in pink. The four flux quantities in purple-shaded boxes represent the principal components of the atmospheric energy balance. Reprinted by permission from Macmillan Publishers Ltd: Nature Geosciences (Stephens et al., 2012), copyright 2012.

After carbon dioxide, methane is the second most important anthropogenic greenhouse gas. Its radiative forcing amounts to $0.48 \pm 0.10\,\mathrm{W\,m^{-2}}$ for the period 1750–2011 (concentration-based estimate). Thereby, methane accounts for roughly one-fifth of the total radiative forcing induced by anthropogenic emissions of well-mixed greenhouse gases in this period (IPCC, 2013). Apart from this direct radiative forcing, methane indirectly affects climate as precursor of tropospheric ozone (O_3) and stratospheric water vapor (H_2O). About 50–65 % of total methane emissions are caused by anthropogenic activities. Since preindustrial times, global atmospheric methane concentrations have increased by 150 %. After a decade of stagnation (Dlugokencky et al., 2011), global methane concentrations started to rise again in 2007 (Nisbet et al., 2014). With a relatively short atmospheric lifetime of about 9 years (Prather et al., 2012), methane is an attractive target for short-term climate change mitigation. Emission regularization strategies require an accurate understanding of the global methane budget, but large uncertainties in the magnitude of individual sources give rise to an ongoing scientific debate. Among the dominant drivers of the renewed methane

increase since 2007 are likely growing methane emissions from natural wetlands and from the prospering fossil fuel industry (Kirschke et al., 2013). However, the relative contributions of these drivers are still poorly quantified. Major methane leakage from oil and natural gas wells as well as from pipelines and natural gas consumption would seriously question the climate benefit of natural gas usage compared to coal (Howarth, 2014). Only recently, a large well blowout in the Los Angeles basin resulted in a massive methane release (Conley et al., 2016). High uncertainty remains also in estimating possible methane feedbacks to climate change, which likely include increasing methane emissions from wetlands, thawing permafrost regions, and methane hydrates (O'Connor et al., 2010; Schuur et al., 2015).

Atmospheric water vapor is an even more effective greenhouse gas than methane and acts as dominant contributor to the global greenhouse effect (Kiehl and Trenberth, 1997). However, water vapor is not considered as a climate forcing, but as positive feedback process to anthropogenic climate change (IPCC, 2013). This reflects the fact that water vapor concentrations in the atmosphere are mainly controlled by air temperature and not by anthropogenic emissions. Increasing temperatures intensify the main source of atmospheric water vapor, i.e., the evaporation from ocean surfaces. Resulting higher water vapor concentrations, in turn, further enhance the greenhouse effect (Held and Soden, 2000). In the stratosphere, however, water vapor is also produced by the oxidation of methane and is therefore perceived as radiative forcing agent. Especially, water vapor in the lowermost stratosphere determines the amount of longwave radiation that can escape to space and is therefore highly relevant for surface climate (Harries et al., 2008; Solomon et al., 2010). Within the global hydrological cycle, water vapor is removed from the atmosphere after a typical residence time of about 10 days by condensation or sublimation and subsequent precipitation. As key component of our climate system, the global water cycle is mainly responsible for the formation of climate zones due to distinct distribution of precipitation, for the transport of energy from the Earth's surface to the atmosphere in form of latent heat, and for driving the global atmospheric circulation. Within these large-scale circulation patterns, water vapor and other atmospheric trace gases can be transported over long distances from source regions to receptor regions. Such transport processes are highly relevant for emission reduction regularizations (e.g., TF-HTAP, 2010). Despite this fundamental importance of the global water cycle, details on its coupling with general circulation patterns and its response to climate change are still not fully understood and introduce major uncertainties in climate modeling (Bony et al., 2015).

Overall, effective climate change mitigation requires more accurate quantification of greenhouse gas sources and sinks as well as a more comprehensive understanding of atmospheric transport, among others. Beside advancements in modeling capabilities, long-term monitoring of atmospheric trace species with high spatiotemporal resolution and global coverage is required. While global observations are available from satellite remote sensing (e.g., Wiegele et al., 2014; Scheepmaker et al., 2015; Turner et al., 2015), these data sets often suffer from inhomogeneities over longer time periods. However, homogeneous long-term time series are provided by means of solar absorption spectrometry within the Network for the Detection of Atmospheric Composition Change (NDACC; www.ndacc.org). Deriving trace gas profile information or total columns from these spectral measurements represents a major challenge for instrument requirements and retrieval algorithms. This is especially true for the species investigated in this thesis, which exhibit very different scales of atmospheric variability: while column-integrated methane exhibits very low variability, concentrations of water vapor may vary over several orders of magnitude in the Earth's atmosphere.

1.2 Objectives and Approach

The background given in the previous section suggests several highly relevant research topics concerning the role of atmospheric water vapor and methane in the global energy budget under the influence of climate change. Within the scope of this thesis, two main questions are addressed:

- How is it possible to quantify the contribution of methane emissions from the production of oil and natural gas to the renewed methane increase since 2007 and how large is this contribution?
- Can long-term observations of water vapor and its isotopes yield insight into long-range transport pathways of atmospheric air masses to Central Europe?

The basis to investigate these questions is formed by a unique data set of atmospheric trace gas measurements obtained at the high-altitude observatory Zugspitze (47.42° N, 10.98° E; 2964 m a.s.l.), where ground-based solar absorption measurements have been operated within NDACC for more than 20 years now. This facility offers an excellent opportunity to monitor undisturbed background conditions prevailing in the midlatitude free troposphere. The goal of this dissertation is to analyze long-term time series of atmospheric methane as well as water vapor and its isotopes as derived from measurements at Mt. Zugspitze with respect to the research questions stated above.

The innovative approach applied in this thesis to answer the first research question is the use of simultaneous observations of methane and ethane (C_2H_6). As ethane is co-emitted from fossil methane sources (i.e., natural gas and oil production), but not from biogenic sources (such as wetlands), it allows to attribute observed methane trends to the respective thermogenic methane source. Methane and ethane time series at Zugspitze are combined with observations at Lauder, New Zealand, as southern hemispheric reference. An atmospheric two-box model is developed in order to simulate hemispheric methane and ethane trends. Based on the latitudinal distribution of ethane sources and its relatively short lifetime compared to methane, it is derived that northern hemispheric methane sources have significantly contributed to the renewed methane increase since 2007. Very high accuracy requirements have to be met in order to monitor atmospheric methane and other trace gases by means of ground-based solar absorption spectrometry. Significant errors may arise from an inexact alignment of the spectrometer's line of sight to the center of the solar disk. In this thesis, an innovative correction method (Reichert et al., 2015) is applied to Zugspitze remote sensing data to eliminate trace gas column errors introduced by these pointing inaccuracies.

Investigating the second topic involves the application of novel retrieval strategies (Schneider et al., 2015) to derive time series of tropospheric water vapor and its isotopes from Zugspitze solar absorption spectra. In previous studies, such water vapor isotopic data have mainly been used to study subtropical moisture transport (e.g., Schneider et al., 2016). This thesis investigates the potential of this new transport tracer for studying midlatitude transport processes. Therefore, extensive backward trajectory modeling is performed and results are combined with Zugspitze water vapor isotopic measurements along with in situ and lidar measurements of various transport tracers (Trickl et al., 2010). The goal is to identify distinct fingerprints in the water vapor isotopic composition at Mt. Zugspitze for different

long-range transport patterns to the Central European free troposphere. Finding such signatures would qualify water vapor isotope measurements as operational indicator for transport events to Central Europe.

This dissertation was conducted at the Karlsruhe Institute of Technology (KIT), Institute of Meteorology and Climate Research, Atmospheric Environmental Research in Garmisch-Partenkirchen (KIT/IMK-IFU). The present thesis is structured as follows: Chapter 2 introduces the fundamental theory of atmospheric remote sensing, which is necessary to follow the investigations performed thereafter. Chapter 3 presents the results obtained from long-term monitoring of methane regarding its renewed increase since 2007. Subsequently, observations of water vapor and its isotopes are analyzed in Chapter 4 with respect to transport processes to the Central European troposphere. Finally, Chapter 5 summarizes results achieved within this dissertation and provides an outlook to prospective research activities.

Chapter 2

Remote Sensing Theory

Atmospheric trace gases interact with solar radiation by means of scattering and absorption processes which lead to attenuation of radiation reaching the Earth's surface. Only photons carrying a distinct amount of energy can be absorbed by gas molecules as their energy states are quantized. Resulting characteristic absorption spectra can be observed by ground-based solar absorption spectrometry. Such measurements contain information on the vertical distribution of various atmospheric trace constituents. This chapter provides the basis for understanding of essential concepts upon which this thesis is built. Section 2.1 describes relevant features of the atmosphere, of solar radiation, and of molecular absorption processes. Subsequently, an overview on the principles of the remote sensing technique applied is given in Section 2.2. The following explanations are based on detailed descriptions presented in, e.g., Davis et al. (2001), Liou (2002), and Wallace and Hobbs (2006).

2.1 Atmospheric Trace Gases and Solar Radiation

2.1.1 Structure and Composition of the Atmosphere

The Earth's atmosphere can be conceived as a mixture of gases surrounding our planet, which enable life by providing the air to breath, by absorbing ultraviolet solar radiation, and by trapping thermal radiation. For most purposes, atmospheric gases can be described by the ideal gas law which relates pressure p, volume V, and temperature T of a gas and can be written as

$$p\,V = n_{\mathrm{mol}}\,R^*\,T \tag{2.1}$$

where n_{mol} is the number of moles and R^* is the universal gas constant.

Air pressure results from the force per unit area exerted by the weight of the air column above the considered altitude. To good approximation, the atmosphere is in hydrostatic equilibrium which implies that the downward gravitational force on an air parcel is balanced by the upward pressure gradient force. The hydrostatic equation is given by

$$\frac{\mathrm{d}p}{\mathrm{d}z} = -\rho g \tag{2.2}$$

where z is the geometric height, ρ the air density, and g the acceleration due to gravity.

Integrating the hydrostatic equation yields a nearly exponential decrease of atmospheric pressure with altitude, i.e.,

$$p(z) \simeq p_0 \exp\left(-\frac{z - z_0}{H}\right) \tag{2.3}$$

where p_0 is the pressure at a reference altitude z_0, usually taken as sea level ($z_0 = 0\,\mathrm{m}$) and H is the scale height, which amounts to about 8 km in the lower atmosphere and is defined as the altitude in which pressure decreased by a factor of 1/e. Note that Eq. (2.3) is an approximation neglecting vertical variations of temperature and gravity acceleration.

The typical vertical distribution of temperature in the atmosphere provides the basis to define several distinct atmospheric layers as shown in Fig. 2.1. The lowest atmospheric layer is the relatively well-mixed troposphere which exhibits decreasing temperatures with height at a mean lapse rate of $6.5\,\mathrm{K\,km^{-1}}$. Meteorological weather phenomena occur primarily in the troposphere which contains nearly all atmospheric water vapor. The turbulent boundary layer extends from the Earth's surface to typically 2 km altitude and is followed above by the free troposphere. The upper boundary of the troposphere is defined by the tropopause (TP), i.e., a temperature minimum at approximately 10 km altitude in the extratropics. Above the tropopause, the stratosphere extends up to altitudes of about 50 km. In this layer temperature increases with height due to heating caused by the absorption of shortwave radiation in the ozone layer. Under these stable conditions, vertical mixing is strongly restricted. Compared to the troposphere, lower stratospheric air is extremely dry as water vapor enters mainly through the cold tropical tropopause region. Meso- and thermosphere are located at even higher altitudes and are not considered further in this thesis.

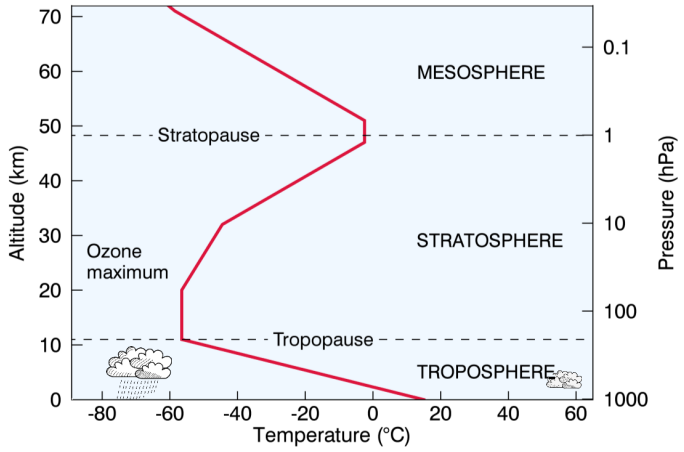

Figure 2.1: Vertical structure of the atmosphere: temperature profile and atmospheric layers.

Global atmospheric circulation patterns are driven by differences in incoming solar radiation. Large-scale motions strive to redistribute energy from low to high latitudes. Prominent features of the general circulation include westerly jet streams which are centered at tropopause altitudes in 30° latitude and formed by deflecting forces resulting from the Earth rotation. Midlatitude surface wind fields are also characterized by westerly winds superimposed by baroclinic waves, which form extratropical cyclones and anticyclones.

The Earth's atmosphere predominantly consists of nitrogen (78.1 %), oxygen (20.9 %), and argon (0.9 %, given as volume fraction of dry air). Remaining minor atmospheric constituents are referred to as trace gases, which include atmospheric greenhouse gases (e.g.,

water vapor, carbon dioxide, methane, and ozone). Greenhouse gases play a key role in the Earth's radiation budget as they are able to effectively trap outgoing thermal radiation. Increasing greenhouse gas concentrations caused by increasing anthropogenic emissions are the main driver of global warming since preindustrial times.

This thesis is focused on two important atmospheric greenhouse gases – water vapor and methane – which are briefly introduced in the following. As primary greenhouse gas, water vapor accounts for about 60 % of the natural greenhouse effect. Water vapor acts as major positive feedback mechanism to global warming as its concentrations are determined by atmospheric conditions and dynamics. In the atmosphere, water can occur as gas, liquid, or solid phase (ice). The global water cycle is illustrated in Fig. 2.2. The major source of atmospheric water vapor is evaporation from ocean surfaces. It is removed by condensation or sublimation at lower temperatures followed by precipitation. Latent heat transported in the global water cycle is critical for redistributing energy from the Earth's surface to the atmosphere. Surface climate is especially sensitive to water vapor perturbations in the lower stratosphere, where water vapor is controlled by transport through the cold tropical tropopause region and by stratospheric oxidation of methane (Solomon et al., 2010). Atmospheric water vapor exhibits a short lifetime of about 10 days and is a highly variable gas with concentrations spanning a range of more than three orders of magnitude.

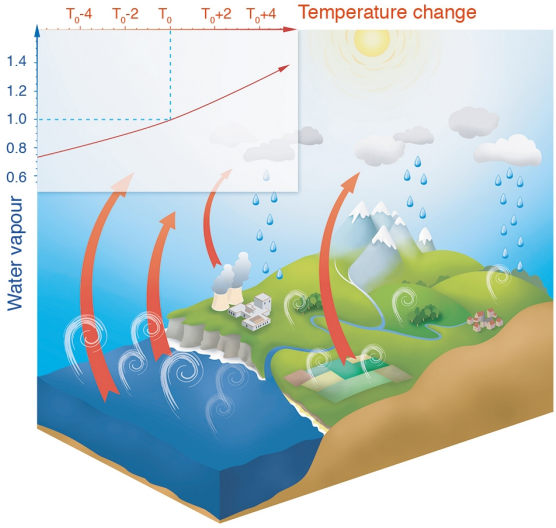

Figure 2.2: Schematic representation of the global water cycle: white curls illustrate evaporation which is compensated by precipitation to close the water budget. Red arrows illustrate the outgoing infrared radiation that is partly absorbed by water vapor and other greenhouse gases. Stratospheric processes are not included in this figure. The upper-left insert indicates the water vapor feedback to climate change, i.e., the relative increase of potential atmospheric water vapor content with increasing air temperature (IPCC, 2013, FAQ 8.1, Fig. 1).

In contrast to water vapor, atmospheric methane exhibits very low variability relative to its large background concentrations. The global mean methane concentration reached 1803 ppb in 2011 after having increased by a factor of 2.5 since preindustrial times (IPCC, 2013). Methane is the second most important anthropogenic greenhouse gas responsible for about 20 % of global warming since 1750. Figure 2.3 depicts an overview of the global methane cycle. Methane is emitted at the Earth's surface by a large variety of natural sources (e.g., wetlands, geological seeps, freshwaters, termites, and hydrates) and anthropogenic sources

(e.g., leakage in fossil fuel production, livestock, waste deposits, rice cultivation, and biomass burning). The primary methane sink is oxidation by hydroxyl radicals (OH) resulting in a tropospheric methane lifetime of about 9 years. Oxidation of methane in the stratosphere is a significant source of water vapor. Therefore, increasing methane concentrations also induce an anthropogenic forcing in this climate-sensitive altitude region.

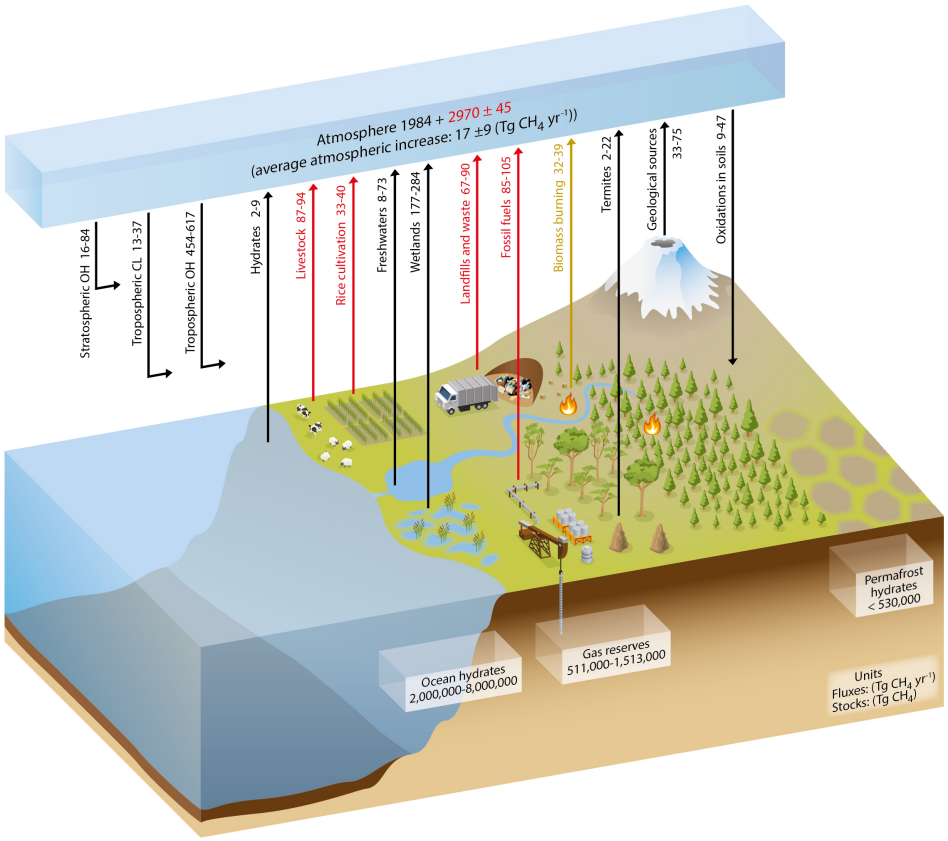

Figure 2.3: Schematic representation of the global methane cycle: natural (anthropogenic) fluxes are depicted as black (red) arrows and combined sources as brown arrows. Annual growth rates and fluxes (in $\mathrm{Tg\,yr^{-1}}$) are estimated for the time period 2000–2009 (IPCC, 2013, Fig. 6.2).

2.1.2 Molecular Absorption of Infrared Radiation

As shown in the previous section, the Earth's atmosphere is a mixture of gases, exposed to and interacting with the radiative energy of the sun. Solar radiation can be understood as an ensemble of waves propagating at the speed of light ($c = 2.998 \times 10^8\,\mathrm{m\,s^{-1}}$). An electromagnetic wave is characterized by its wavelength λ or its wavenumber ν, which is defined as reciprocal of wavelength ($\nu = 1/\lambda$) and commonly applied in solar absorption spectrometry. The energy carried by radiation per unit time interval in a specific direction (solid angle in units of steradian) through a unit area (normal to the direction considered) at a specific wavelength is referred to as spectral radiance I_λ in units of $\mathrm{W\,m^{-2}\,sr^{-1}\,nm^{-1}}$. To good approximation, the electromagnetic spectrum of solar radiation corresponds to the spectral radiance emitted by a blackbody at $T = 5780\,\mathrm{K}$, which is determined by Planck's radiation law. The spectrum of solar radiation exhibits a maximum in the visible spectral range and covers various spectral regions (see Fig. 2.4). While X Rays and ultraviolet

radiation lead to molecular ionization and dissociation, radiation in the visible, infrared, and microwave spectral regions induces transitions in the molecule's electronic configuration or causes the molecule to vibrate or rotate. This thesis is focused on the infrared spectral region, which can be further divided into near-infrared (14000–4000 cm^{-1}), mid-infrared (4000–400 cm^{-1}), and far-infrared (400–10 cm^{-1}) solar radiation.

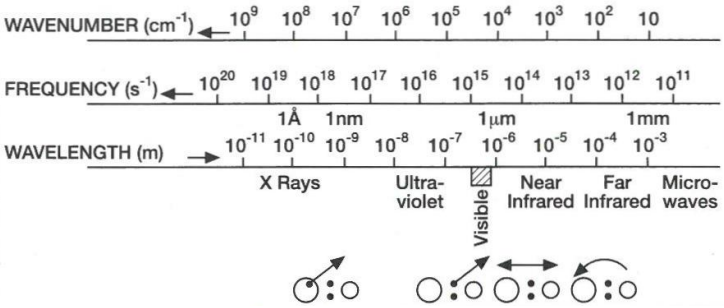

Figure 2.4: Regions of the electromagnetic spectrum and related interactions of radiation and molecules: ionization, dissociation, vibration, and rotation (Brasseur and Solomon, 2005, Fig. 4.1, with permission of Springer).

Radiative Transfer. In general, interaction of solar radiation with atmospheric molecules involves scattering, absorption and emission processes which lead to attenuation of solar radiation in the atmosphere as illustrated in Fig. 2.5. Radiative transfer describes the change in solar spectral radiance while passing an atmospheric volume element and comprises extinction by absorption and scattering as well as enhancements due to scattering into the considered direction and due to atmospheric thermal emission. For remote sensing techniques using direct solar radiation in the infrared spectral region, molecular absorption is the most relevant of these processes, while scattering and emission terms are weak compared to direct solar radiance and may be neglected.

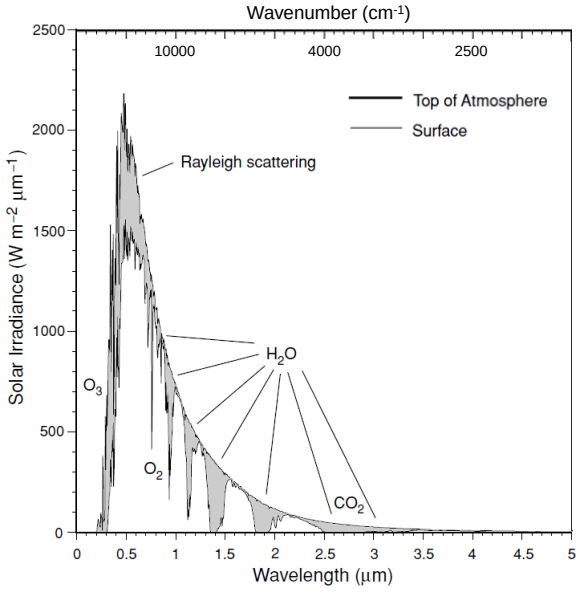

Figure 2.5: Solar spectral irradiance (flux density) at the top of atmosphere and at the surface for a solar zenith angle of 60° under cloud- and aerosol-free conditions. Spectral regions affected by molecular absorption are indicated for most important species (adapted from Liou, 2002, Fig. 3.9).

The fundamental equation in solar absorption infrared spectrometry is Lambert Beer's law which describes the exponential decay of spectral radiance passing through an absorbing medium, i.e.,

$$I_\lambda(s) = I_\lambda(\text{toa}) \exp\Big(- \int_{\text{toa}}^{s} \sigma_{\text{abs},\lambda}(s')\, n_{\text{abs}}(s')\, \mathrm{d}s' \Big) \tag{2.4}$$

where $I_\lambda(s)$ is the solar spectral radiance observed at an optical path length s, $I_\lambda(\text{toa})$ is the solar radiance incident at top of the atmosphere (toa), $\sigma_{\text{abs},\lambda}$ is the spectral absorption cross section of the medium, and n_{abs} is the number density of the absorbing species (units of m^{-3}). The absorption cross section (in units of m^2) depends on temperature and pressure along the optical path. Considering a gas mixture, the integrand in Eq. (2.4) becomes a sum over different absorbing species. For ground-based solar absorption measurements, integration is performed along the optical path of direct sunlight from the top of the atmosphere to the surface. As the optical path length increases with solar zenith angle (sza), attenuation of solar radiation increases with increasing zenith angle.

Molecular Absorption. As molecular energy states are quantized, molecular absorption occurs only in discrete parts of the solar spectrum. Each absorbing atmospheric species exhibits a characteristic absorption line signature. The energy content of radiation is proportional to its wavenumber and the number of photons. The energy of a single photon is described by means of photon energy $E_{\text{ph}} = hc\nu$ with the Planck constant $h = 6.626 \times 10^{-34}\,\text{J s}$. A specific photon may be absorbed by a molecule if the photon energy corresponds to the discrete energy difference ΔE between two molecular energy levels, i.e.,

$$\Delta E = hc\nu \tag{2.5}$$

The total energy E of a molecule is composed of its continuous translational energy (E_{tra}) and quantized energy levels of its electronic configuration (E_{ele}), its vibrational state (E_{vib}), and its rotational state (E_{rot}). It can be written as

$$E = E_{\text{tra}} + E_{\text{ele}} + E_{\text{vib}} + E_{\text{rot}} \tag{2.6}$$

Focusing on absorption of mid-infrared radiation, only transitions between vibrational and rotational states have to be considered, which are described in the following.

Rotational Energy Levels. Under typical atmospheric conditions many rotational modes of molecules are activated. Rotations of an exemplary diatomic molecule can be described by the model of a linear rigid rotator, i.e., two atoms rotating around their center of mass at a fixed distance. Based on quantum mechanics, quantized levels of rotational energy are given by

$$E_{\text{rot}}(J) = hc\, B\, J(J+1) \tag{2.7}$$

where J is the rotational quantum number ($J = 0, 1, 2, ...$) and $B = h/8\pi^2 c I_{\text{rot}}$ is the rotational constant with the moment of inertia I_{rot} of the rigid rotator. The magnetic quantum number m_{J} can take on values of $-J \leq m_{\text{J}} \leq +J$. Therefore, each rotational energy level is $(2J+1)$-fold degenerated, i.e., different sets of quantum numbers yield the same energy level.

Absorption requires the coupling of the absorbing molecule with the electromagnetic field. Therefore, molecular rotations can only be activated by absorption if the molecule has a

permanent electric dipole moment (i.e., an asymmetric charge distribution). As energy differences between rotational states are relatively small, pure rotational absorption lines are located in the far-infrared and microwave spectral region.

Vibrational Energy Levels. Vibrations of a diatomic molecule can be described by means of the quantum-mechanical analog of a harmonic oscillator, i.e., two atoms oscillating around their equilibrium position with a restoring force proportional to the displacement. Quantized vibrational energy levels are given by

$$E_{\text{vib}}(v) = hc\,\nu_0\,(v + {}^1\!/_2) \tag{2.8}$$

where ν_0 is the vibrational wavenumber and v is the vibrational quantum number ($v = 0, 1, 2, ...$). The selection rule for vibrational energy transitions is $\Delta v = \pm 1$. Most atmospheric molecules populate the vibrational ground state ($v = 0$) and absorption activates the first excited state ($v = 1$). A vibrational mode can only be activated by electromagnetic radiation if a change in the molecular dipole moment is induced. Vibrational energy transitions require photons with higher energies than rotational energy transitions and vibrational absorption lines occur in the mid-infrared spectral region.

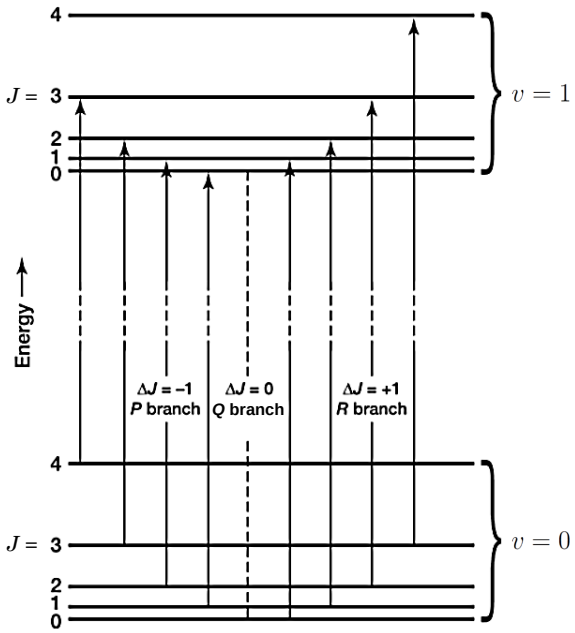

Figure 2.6: Schematic representation of molecular energy levels and allowed vibrational-rotational transitions (adapted from Brasseur and Solomon, 2005, Fig. 2.1.b, with permission of Springer).

Vibrational-Rotational Bands. As molecular vibrations result in an oscillating dipole moment, simultaneous molecular rotations can be activated – even for molecules without a permanent dipole moment. Combined vibration-rotation transitions generate complex vibrational-rotational bands, which are composed of many individual absorption lines in the vicinity of the fundamental vibrational wavenumber. Figure 2.6 illustrates such a vibrational-rotational transition from the vibrational ground-state ($v = 0$) to the first exited state ($v = 1$) superimposed by various rotational transitions. The P-branch of the absorption band corresponds to rotational transitions with selection rule $\Delta J = -1$,

while the R-branch corresponds to $\Delta J = +1$. The Q-branch of $\Delta J = 0$ is forbidden for linear diatomic molecules. In contrast, for linear (e.g., CO_2) or bent (e.g., H_2O) triatomic molecules the transition $\Delta J = 0$ is allowed, which results in the formation of a Q-branch at the vibrational wavenumber itself.

Deviations from the idealized harmonic oscillator and rigid rotator models give rise to even more complex transitions, e.g., overtone bands ($\Delta v = \pm 2, \pm 3, ...$), and differences between vibrational wavenumbers of ground-state and upper-state transitions. Molecules with more than two atoms have higher degrees of freedom resulting in additional vibrational modes, e.g., the deformation of bond angles. Isotopes of a molecular species can be distinguished by their distinct spectral fingerprints, as their absorption line positions deviate from each other in consequence of their differing masses determined by the number of neutrons.

Absorption by Water Vapor and Methane. Molecular absorption of infrared radiation by water vapor and methane is of particular interest within the scope of this thesis which focuses on these two important atmospheric trace gases.

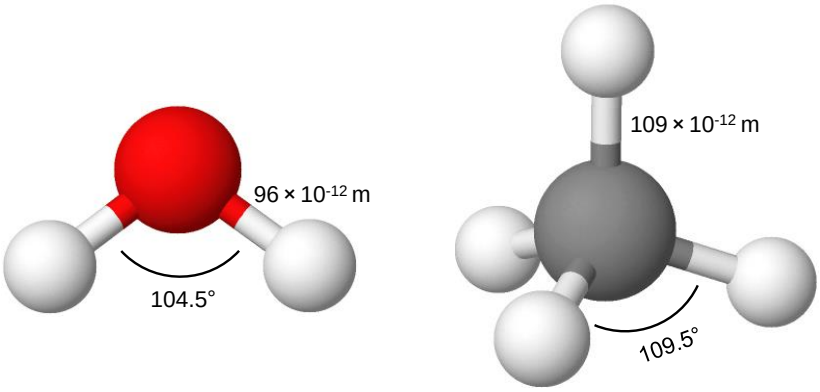

Figure 2.7: Visualization of the molecular structure of water vapor (H_2O; left) and methane (CH_4; right) with ground-state bond angles and lengths (http://molview.org).

Water vapor is a bent triatomic molecule (see Fig. 2.7) with a permanent electric dipole moment caused by its non-linear structure and the O-H bond polarity. Consequently, water vapor absorption includes a pure rotational band in the far-infrared ($<500\,\mathrm{cm}^{-1}$). Fundamental vibrational modes (in vacuum) occur at $\nu_1 = 3657\,\mathrm{cm}^{-1}$ (symmetric stretch), $\nu_2 = 1595\,\mathrm{cm}^{-1}$ (bending), and $\nu_3 = 3756\,\mathrm{cm}^{-1}$ (asymmetric stretch). Due to its pure rotational band and vibrational-rotational bands over the entire infrared spectral region, water vapor is the most potent greenhouse gas in the Earth's atmosphere. Methane exhibits a tetrahedral structure (see Fig. 2.7), which allows for two infrared-active vibration-rotation modes at $\nu_3 = 3019\,\mathrm{cm}^{-1}$ (asymmetric stretch, triply-degenerated) and $\nu_4 = 1306\,\mathrm{cm}^{-1}$ (deformation, triply-degenerated). In contrast to water vapor, methane does not have a permanent dipole moment and hence no pure rotational band. Methane vibration-rotation bands are located in "atmospheric window" regions and are still far from being saturated at current atmospheric methane levels. Therefore, additional methane very effectively absorbs infrared radiation and exhibits a global warming potential of 28–34 compared to CO_2 on per mass emitted basis over a 100-year time horizon (IPCC, 2013).

Absorption Line Broadening. Molecular absorption lines are characterized by line intensity and line shape. Line intensity depends on the quantum-mechanical probability of the transition to an excited state and on the population of the ground-state, which is a function of temperature. Absorption line shapes observed are not infinitely narrow spectral lines but extend over finite wavenumber regions. This broadening of spectral absorption lines is caused by different line broadening mechanisms, which are introduced in the following.

First, the natural line width is a direct consequence of Heisenberg's uncertainty principle which states that the energy E of an excited molecular state and its lifetime τ cannot be simultaneously determined with unlimited high precision, i.e.,

$$\Delta E \cdot \Delta\tau \geq h/2\pi \tag{2.9}$$

Hence, the finite natural lifetime of an excited molecular state implies a finite uncertainty in its energy. The corresponding spectral line is distributed over a narrow wavenumber interval. Natural line broadening is small compared to the following broadening effects and is therefore negligible under atmospheric conditions.

The second mechanism is pressure broadening. Molecular collisions may diminish the lifetime of an excited molecular state and therefore increase its energy uncertainty (see Eq. (2.9)). As collision frequency increases with pressure, pressure broadening dominates at altitudes below 20 km. Pressure broadening is described by a Lorentz line shape, i.e.,

$$f_{\mathrm{L}}(\nu - \nu_0) = \frac{1}{\pi} \cdot \frac{\alpha_{\mathrm{L}}}{\alpha_{\mathrm{L}}^2 + (\nu - \nu_0)^2} \tag{2.10}$$

where ν_0 is the wavenumber on which the line is centered and α_{L} is the half-width at half-maximum of the Lorentz line. α_{L} is a function of pressure and, to a lesser extent, of temperature and can be written as

$$\alpha_{\mathrm{L}}(p, T) = \alpha_{\mathrm{L}}(p_0, T_0)\, \frac{p}{p_0} \sqrt{\frac{T_0}{T}} \tag{2.11}$$

with standard pressure p_0 and temperature T_0.

Above 50 km altitude where pressure broadening is negligible, a third line broadening mechanism becomes dominant. Thermal broadening results from the Doppler effect caused by different velocity components of absorbing molecules relative to the radiation source. The velocity distribution depends on molecular mass and is determined by gas temperature. Doppler broadening yields a Gaussian line shape given by

$$f_{\mathrm{D}}(\nu - \nu_0) = \frac{1}{\alpha_{\mathrm{D}}\sqrt{\pi}} \exp\Big(- \frac{(\nu - \nu_0)^2}{\alpha_{\mathrm{D}}^2} \Big) \tag{2.12}$$

where α_{D} is the Doppler width of the line, i.e.,

$$\alpha_{\mathrm{D}}(T) = \frac{\nu_0}{c} \sqrt{\frac{2kT}{M}} \tag{2.13}$$

with the Boltzmann constant k and the mass M of the absorbing molecule. The corresponding half-width at half-maximum may be calculated as $(\alpha_{\mathrm{D}} \cdot \sqrt{\ln 2})$. Consequently, Doppler line width is independent of pressure but depends on temperature.

Finally, in the intermediate altitude region (20–50 km), pressure and Doppler broadening need to be taken into account. The resulting line shape can be obtained by convolution of Doppler and Lorentz line shapes and is referred to as Voigt profile, i.e.,

$$f_{\mathrm{V}}(\nu - \nu_0) = \frac{\alpha_{\mathrm{L}}}{\alpha_{\mathrm{D}}\,\pi^{3/2}} \int_0^{\infty} \frac{1}{\alpha_{\mathrm{L}}^2 + (\nu' - \nu_0)^2} \exp\Big(- \frac{(\nu - \nu')^2}{\alpha_{\mathrm{D}}^2} \Big)\, \mathrm{d}\nu' \tag{2.14}$$

The presented characteristic line shapes of different line broadening mechanisms are illustrated in Fig. 2.8. Doppler lines are more intense at the line center as compared to Lorentz lines which exhibit stronger contributions in the line wings. For saturated lines additional absorption can only occur in the line wings and is therefore mainly related to pressure broadening. As different line broadening effects are dominant in distinct altitude regions, absorption lines contain information on the altitude distribution of absorbing molecules. This important fact is utilized by solar absorption spectrometry in order to retrieve profiles of atmospheric trace gases from observed molecular absorption spectra.

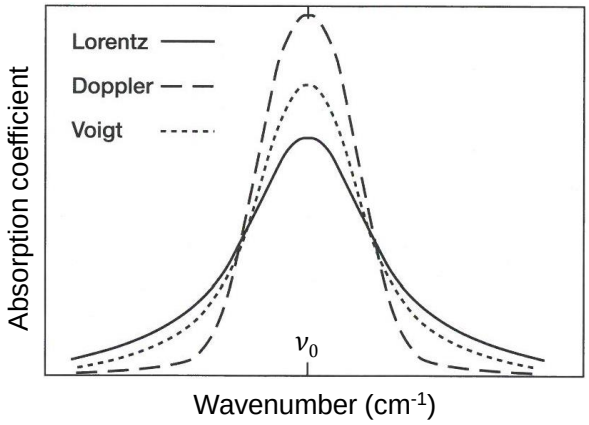

Figure 2.8: Lorentz, Doppler, and Voigt line shapes of molecular absorption lines with equal line widths and intensities (from Brasseur and Solomon, 2005, Fig. 4.23, with permission of Springer).

2.2 Ground-Based Infrared Spectrometry

Infrared remote sensing is a valuable method for atmospheric monitoring, as various atmospheric trace gases interact with solar radiation in this spectral region. Resulting characteristic solar absorption spectra can be measured by means of ground-based Fourier transform infrared (FTIR) spectrometry. The basic concepts of this measurement technique are introduced in Section 2.2.1. Subsequently, it is explained in Section 2.2.2, how to retrieve atmospheric trace gas profiles from FTIR observations.

2.2.1 Principles of Fourier Transform Spectrometry

Ground-based solar absorption FTIR spectrometry is a passive remote sensing method using the sun as light source and the atmosphere as absorbing medium. Such measurements require two main instrumental components: an optical device to track the exact position of the sun and a spectrometer to record the absorption signal. The basic setup of an

FTIR spectrometer is illustrated in Fig. 2.9. Direct solar radiation is traced by the solar tracker and directed into the core of the FTIR instrument, which is essentially a Michelson interferometer. First, the incoming beam of solar radiation is split into two parts by a semitransparent mirror (beam splitter). Subsequently, one of these beams is reflected at a fixed mirror, while the other beam hits a mirror moving at constant velocity. Both individually reflected beams are recombined after passing the beam splitter once more. Finally, the resulting interference pattern is recorded by the detector. Interference arises due to the optical path difference between the fixed mirror path and the moving mirror path. An interferogram is generated by recording the signal at many discrete positions of the moving mirror.

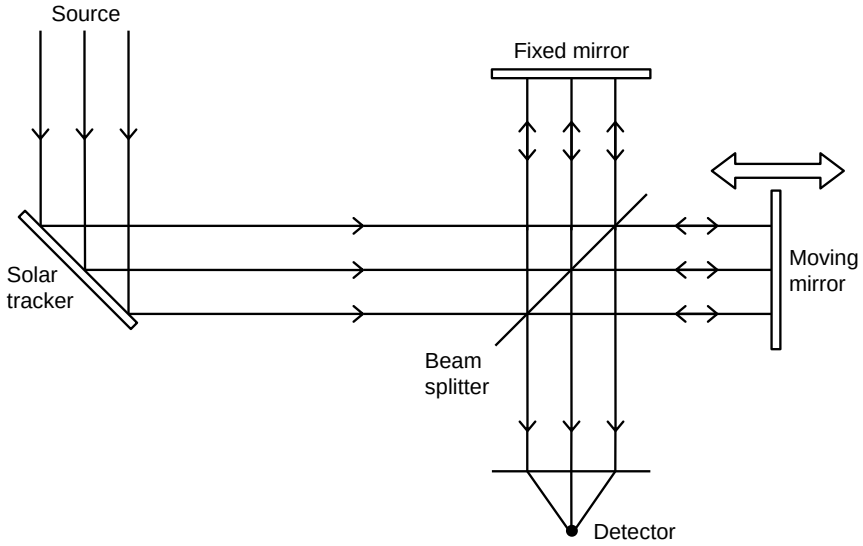

Figure 2.9: Schematic representation of a Fourier transform spectrometer as applied in solar absorption spectrometry.

To gain the spectral information of interest, the interferogram $I(\Delta x)$, i.e., intensity as function of mirror displacement Δx, has to be converted to a spectrum $I(\nu)$, i.e., intensity as function of wavenumber. This can be achieved by means of an inverse Fourier transformation. A Fourier transformation translates from the domain of wavenumbers to the domain of mirror displacement and can be written as

$$I(\Delta x) = \int_{-\infty}^{+\infty} I(\nu) cos(2\pi\nu\Delta x)\,\mathrm{d}\nu \tag{2.15}$$

We are interested in the inverse Fourier transformation given by

$$I(\nu) = \int_{-\infty}^{+\infty} I(\Delta x) cos(2\pi\nu\Delta x)\,\mathrm{d}\Delta x \tag{2.16}$$

The interferogram of an ideal monochromatic source is an infinite cosine wave and inverse Fourier transformation would result in a delta function at the respective wavenumber.

In reality, the interferogram is truncated at a finite maximum mirror displacement. Therefore, the FTIR spectrum of a monochromatic source yields a broadened spectral line with additional side lobes. The spectral resolution of an FTIR spectrometer depends on its

maximum optical path difference $\mathrm{OPD}_{\max}$ (i.e., twice the maximum moving mirror displacement). With increasing maximum optical path difference spectral resolution is improved, i.e., $\Delta\nu = 1/\mathrm{OPD}_{\max}$. Consequently, the FTIR absorption line shape is a combination of the physical line shape of the atmospheric spectrum (see Fig. 2.8) and the instrumental line shape (ILS). This characteristic line shape of an FTIR instrument resembles a cardinal sine function. The width of the ILS has to be small compared to the width of spectral lines that are to be observed. In practice, a trade-off needs to be found between optimizing spectral resolution, measurement duration, and signal-to-noise ratio.

Compared to dispersive spectrometers, the FTIR technique has several advantages. First, all wavenumbers are simultaneously recorded (Fellgett advantage) and, consequently, FTIR measurements are significantly faster than grating spectrometers which record each wavenumber separately. Second, FTIR spectra exhibit a higher signal-to-noise ratio for same resolution and measurement duration (Jacquinot advantage), as the throughput is not diminished by slits or apertures as narrow as applied in grating spectrometers. Third, FTIR uses a reference laser for permanent control of the optical path difference, which results in a built-in wavenumber calibration (Connes advantage).

FTIR measurements analyzed within the scope of this thesis are primarily obtained at the high-altitude observatory Zugspitze (47.42° N, 10.98° E; 2964 m a.s.l.), which offers unique possibilities for monitoring undisturbed free-tropospheric background conditions. As part of the Network for the Detection of Atmospheric Composition Change, a Bruker IFS 125HR FTIR spectrometer has been in operation at Mt. Zugspitze since 1995 (Sussmann and Schäfer, 1997). Mid-infrared FTIR spectra are recorded by cooled InSb detectors with a typical spectral resolution of $0.005\,\mathrm{cm}^{-1}$ ($\mathrm{OPD}_{\max} = 175\,\mathrm{cm}$). Six individual scans are averaged which results in an integration time of about seven minutes. For trace gas retrievals performed in this thesis, a spectral filter is applied covering the mid-infrared wavenumber region of 2400–3100 cm^{-1}.

2.2.2 Retrieval of Trace Gas Profiles

So far, we learned how to measure high-resolution solar absorption spectra by means of FTIR spectrometry. In this section, we aim at deriving vertical trace gas profiles from such mid-infrared spectra. The trace gas of interest is referred to as target species. As its absorption signatures, in general, partially overlap with absorption lines of other trace species, these so-called interfering species have to be considered as well. To minimize the number of relevant interfering species as well as computation time, narrow spectral regions (i.e., microwindows) are selected from FTIR spectra to perform the retrieval.

A schematic representation of the retrieval process is presented in Fig. 2.10. Essential components include the measurement vector $\boldsymbol{y}$ (i.e., an absorption spectrum), the atmospheric state vector $\boldsymbol{x}$ (i.e., a trace gas profile), and the forward model F. In general, F is a complex non-linear function which enables to simulate a measured spectrum by modeling the propagation of light through the atmosphere. For this purpose, the model atmosphere is divided into discrete levels and $\boldsymbol{x}$ becomes a discrete representation of the continuous atmospheric state at the moment of measurement. A synthetic spectrum can be computed using the forward model and a priori knowledge on the profiles of pressure, temperature

and trace gases contained in the atmosphere, i.e.,

$$\boldsymbol{y} = F(\boldsymbol{x}) + \boldsymbol{\epsilon} \tag{2.17}$$

where ϵ denotes the measurement noise. To estimate the true atmospheric state from the measurement, we are interested in the inversion of the forward model given as

$$\boldsymbol{x} = F^{-1}(\boldsymbol{y}) \tag{2.18}$$

In the retrieval process, the synthetic spectrum is compared to the measured FTIR spectrum. At first, this comparison will yield major discrepancies. In an iterative process, the calculated spectrum is then fitted to the measured spectrum by varying the vertical profiles of target and interfering species used in the forward calculation. By this means, a best estimate of the true atmospheric state can be obtained.

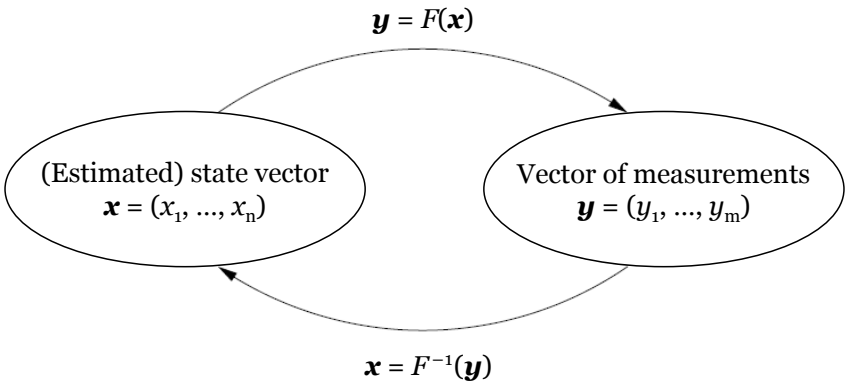

Figure 2.10: Forward and inverse problem in remote sensing applications. Solving the inverse problem provides only an estimate for the true atmospheric state (adapted from Zdunkowski et al., 2007, Fig. 11.1).

As the inverse problem is physically ill posed, various atmospheric state vectors would be consistent with a measurement and there is no exact solution of Eq. (2.18). Nevertheless, the most probable atmospheric state vector can be estimated by adding a priori knowledge of the state vector and minimizing a cost function which comprises two terms. First, the spectral error cost implies to minimize the deviation of the synthetic spectrum from the measurement. Second, the regularization cost acts to constrain the deviation between the estimated state vector and the a priori profile $\boldsymbol{x_a}$ which can be determined from measurement ensembles or model simulations. The resulting costfunction to be minimized can be expressed as least squares problem, i.e.,

$$\left(\boldsymbol{y} - F(\boldsymbol{x})\right)^T \mathbf{S}_\epsilon{}^{-1} \left(\boldsymbol{y} - F(\boldsymbol{x})\right) + \left(\boldsymbol{x} - \boldsymbol{x_a}\right)^T \mathbf{R} \left(\boldsymbol{x} - \boldsymbol{x_a}\right) \tag{2.19}$$

with the measurement error covariance matrix $\mathbf{S}_\epsilon$ and the regularization matrix $\mathbf{R}$.

The regularization matrix enables to include a priori knowledge of the target species profile and to avoid oscillating profiles as retrieval result. There are two approaches to construct the regularization matrix. In optimal estimation theory (Rodgers, 1976), $\mathbf{R}$ is set up as the inverse of the a priori covariance matrix $\mathbf{S_a}$, which can be derived from a measurement ensemble of true profiles covering the full range of possible atmospheric states. If such data are not available, alternatively, a smoothing constraint can be applied by means of Tikhonov

regularization (Tikhonov, 1963). In the case of first-order Tikhonov regularization, only the shape of the retrieved profile is constrained, while absolute profile values are not. Then, $\mathbf{R}$ is defined as

$$\mathbf{R} = \alpha\,\mathbf{L}^T\mathbf{L} \qquad \text{with } \mathbf{L} = \begin{pmatrix} 1 & -1 & 0 & \cdots & 0 \\ 0 & 1 & -1 & \ddots & \vdots \\ \vdots & \ddots & \ddots & \ddots & 0 \\ 0 & \cdots & 0 & 1 & -1 \\ 0 & \cdots & \cdots & \cdots & 0 \end{pmatrix} \tag{2.20}$$

where α is the regularization strength and $\mathbf{L}$ is the first derivative operator which is an $l \times l$ matrix in case of l atmospheric model levels. The magnitude of α can be optimized for different purposes (e.g., Steck, 2002). The limiting case of $\alpha \to \infty$ represents an infinitely strong constraint on the profile shape resulting in a scaling of the a priori profile. In contrast, the limiting case of $\alpha \to 0$ describes a retrieval without any regularization, which will result in a perfect spectral fit but heavily oscillating profiles.

Due to the non-linearity of radiative transfer and of the forward model, Newtonian iteration has to be applied to solve the least squares problem of Eq. (2.19), i.e.,

$$\boldsymbol{x}_{i+1} = \boldsymbol{x}_i + \left(\mathbf{K}_i^T\,{\mathbf{S}_\epsilon}^{-1}\,\mathbf{K}_i + \mathbf{R}\right)^{-1} \times \left(\mathbf{K}_i^T\,{\mathbf{S}_\epsilon}^{-1}\big(\boldsymbol{y} - F(\boldsymbol{x}_i)\big) - \mathbf{R}(\boldsymbol{x}_i - \boldsymbol{x_a})\right) \tag{2.21}$$

where the subscript i denotes the iteration index and $\mathbf{K} = \partial\boldsymbol{y}/\partial\boldsymbol{x}$ is the Jacobian matrix, which describes how the spectral measurement changes with a changing state vector. Convergence is reached if calculated and measured spectra deviate less than a defined convergence criterion. The solution, finally, provides us with the optimal estimate of the atmospheric state given the measurements and the a priori knowledge available.

The retrieval result can be characterized by means of the averaging kernel matrix $\mathbf{A}$ which relates the variability of the true state $\boldsymbol{x}_{\text{true}}$ at measurement time to the retrieved state variability relative to the a priori state vector, i.e.,

$$\boldsymbol{x} - \boldsymbol{x_a} = \mathbf{A}\,(\boldsymbol{x}_{\text{true}} - \boldsymbol{x_a}) \tag{2.22}$$

For an ideal remote sensing system, $\mathbf{A}$ is a unity matrix representing perfect sensitivity at each model level without inter-correlations between the levels. In practice, the vertical resolution of an FTIR system is limited. It can be determined by the full width at half-maximum of the averaging kernels (i.e., the rows of $\mathbf{A}$) which describe to what extent the retrieved state at a certain altitude is distorted by signals at other altitudes. The trace of the averaging kernel matrix yields the number of independent pieces of information provided by the measurement, which is referred to as degrees of freedom for signal (DOFS).

Error analysis for remote sensing systems is formulated in detail in Rodgers (1990, 2000). Several systematic and random error components cause the retrieved state vector to deviate from the true target profile. Briefly summarized, error sources consist of smoothing error (limited vertical resolution of the remote sensing system), model parameter error (uncertainties in applied model parameters, such as spectroscopic data), forward model error (incomplete representation of real physical processes in the model), and retrieval noise error (caused by measurement noise).

Within the scope of this thesis, trace gas profile retrievals are performed with the spectral fitting code PROFFIT (PROFile Fit; Hase et al., 2004). This level-based algorithm executes

the retrieval on the model levels and assumes linear interpolation of volume mixing ratio (VMR) profiles between the levels. The root mean square value of the spectral residual (difference between simulated and measured spectrum) is used as noise level to compensate for variations in measurement quality. Beside a priori profiles applied for regularization (see Eq. (2.19)), variable first guess profiles are implemented in PROFFIT to minimize the number of necessary retrieval iterations. Before the actual target species retrieval, solar absorption signatures are determined for each spectrum. The following paragraphs introduce details on the strategies applied in this thesis for the retrieval of considered target species from ground-based solar absorption FTIR measurements.

Retrieval Strategy for Water Vapor and its Isotopes. Progress achieved within the project MUSICA (MUlti-platform remote Sensing of Isotopologues for investigating the Cycle of Atmospheric water) offers retrieval methods for tropospheric profiles of water vapor and its isotopes from mid-infrared FTIR measurements (Schneider et al., 2012; Barthlott et al., 2017). In the context of this thesis, two stable water vapor isotopes are of particular interest: H_2O ($^1H_2{}^{16}O$) and HDO ($^1H^2H^{16}O$) with average abundances of 99.7 % and 0.03 %, respectively. Variations in the HDO-H_2O ratio of atmospheric water vapor are typically expressed in terms of δD, i.e., as relative deviation from a reference HDO-H_2O ratio standard (Craig, 1961; see Eq. (4.1)). The latest H_2O-δD retrieval version (v2015; Schneider et al., 2016) is applied in this thesis and can be briefly summarized as follows. As water vapor volume mixing ratios are log-normally distributed, optimal estimation is performed on logarithmic scale. A priori profiles are derived from LMDZ model runs and an inter-species constraint between H_2O and HDO is applied. Absorption line data from the high-resolution transmission molecular absorption database (HITRAN, version 2012; Rothman et al., 2013) are optimized for speed-dependent Voigt line shape parameterization. The retrieval comprises the analysis of 12 microwindows and a simultaneous fit of several interfering species (CO_2, O_3, N_2O, CH_4, HCl, and temperature). The model atmosphere is discretized in 22 altitude levels covering the range from observer altitude to about 60 km altitude. Two retrieval products are available: (i) optimal estimation of water vapor for maximum vertical resolution of H_2O profiles (type 1) and (ii) quasi optimal estimation of H_2O-δD pairs with consistent vertical profile sensitivity derived by a posteriori processing (type 2). The latter product is used to obtain consistent H_2O-δD time series from FTIR measurements at Mt. Zugspitze.

Retrieval Strategy for Methane and Ethane. In this thesis, methane column abundances are retrieved from mid-infrared FTIR spectra using the strategy developed by Sussmann et al. (2011). This retrieval method, which is recommended within NDACC, optimizes methane total column precision, while minimizing water vapor interference errors. Mid-infrared NDACC-type methane retrievals are in good agreement with near-infrared FTIR measurements from the Total Carbon Column Observing Network (TCCON) as shown by Sussmann et al. (2013) and Ostler et al. (2014). Methane profile retrievals are performed using first-order Tikhonov regularization (see Eq. (2.20)) with a regularization strength optimized for minimum diurnal variation and maximum vertical information content (i.e., maximum DOFS). Three spectral microwindows are analyzed, which cover the wavenumber regions of 2613.7–2615.4 cm^{-1}, 2835.5–2835.8 cm^{-1}, and 2921.0–2921.6 cm^{-1}, as illustrated in Fig. 2.11. Beside the target species, three interfering species (i.e., H_2O, HDO, and NO_2)

are fitted by scaling of the respective first guess profile. Additionally, five species (i.e., CO_2, O_3, N_2O, HCL, and OCS) are considered in the model atmosphere without fitting. Absorption line data are taken from HITRAN (version 2000) including its 2001 update (Rothman et al., 2003).

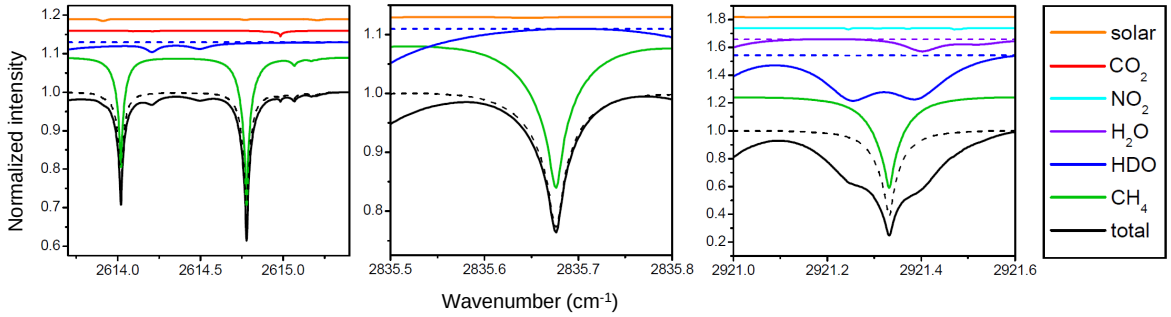

Figure 2.11: Spectral microwindows applied in the methane retrieval: spectral contributions from target and interfering species under moist (solid lines) and dry conditions (dashed lines) at a solar zenith angle of 65° (adapted from Sussmann et al., 2011).

A priori profiles are derived from a 40-year model run of the Whole Atmosphere Community Climate Model (WACCM version 6; García et al., 2007). The influence of the applied methane a priori profile on methane trend estimates has been shown to be negligible (Sussmann et al., 2013). Figure 2.12 presents a priori VMR profiles for Zugspitze site on a logarithmic scale. Methane is relatively well-mixed in the free troposphere and exhibits a strong negative gradient in the stratosphere. In addition, the ozone maximum at around 30 km altitude is clearly visible as well as the strong water vapor decrease between the moist lower troposphere and very dry conditions in the lower stratosphere.

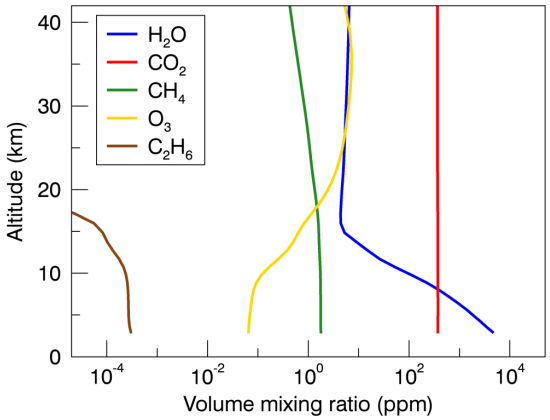

Figure 2.12: Typical vertical profiles of important trace gases at Zugspitze site: volume mixing ratio profiles in units of parts per million (ppm) as derived from the WACCM model.

Beside the retrieval of methane, atmospheric ethane time series are derived and utilized for the source attribution of methane trends in Chapter 3. The ethane retrieval strategy applied in this thesis follows the method described in Vigouroux et al. (2012). Two microwindows are analyzed covering the wavenumber regions of 2976.66–2976.95 cm^{-1} and 2983.20–2983.55 cm^{-1}. Ethane spectroscopic data are provided in form of a pseudo-line list by Franco et al. (2015), while data from HITRAN 2008 are taken for interfering species.

First-order Tikhonov regularization is applied with a regularization strength chosen to obtain maximum DOFS while avoiding profile oscillations. Following recommendations of the NDACC Infrared Working Group (IRWG, 2014), three interfering species are considered: while O_3 and CH_4 are included without fitting, for H_2O a simultaneous profile scaling retrieval is performed.

For methane and ethane retrievals, the atmosphere is discretized in 43 model levels covering an altitude region up to 120 km. Pressure and temperature data are compiled from hourly ground pressure measurements and four times daily temperature profiles provided by the National Center for Environmental Prediction (NCEP). Within PROFFIT, pressure and temperature input is interpolated to measurement time and the pressure profile is calculated assuming hydrostatic equilibrium. First guess profiles for water vapor are derived from four times daily NCEP humidity profiles. For all other species, daily first guess profiles are determined using the spectral fitting software GFIT 2014 (Wunch et al., 2011), which takes tropopause altitude variations into account.

Chapter 3

Renewed Methane Increase (2007–2014)

3.1 Introduction

Methane is the second most important anthropogenic greenhouse gas and responsible for about 20 % of global warming since preindustrial times (Kirschke et al., 2013). Due to its relatively short atmospheric lifetime of about 9 years, methane is an attractive target for climate change mitigation strategies in the next few decades (Dlugokencky et al., 2011). These require an accurate understanding of the global and regional atmospheric methane budget, which is determined by a large variety of natural and anthropogenic sources. About 60 % of total methane emissions originate from anthropogenic activities (IPCC, 2013). Northern hemispheric sources account for 70 % of global emissions (Kai et al., 2011). Three major processes of methane formation can be distinguished: biogenic methane produced by microbes from organic matter under anaerobic conditions (e.g., in wetlands, ruminants, and waste deposits), thermogenic methane formed in geological processes at elevated temperatures (fossil fuels), and pyrogenic methane produced by incomplete combustion processes, e.g., biomass burning (Kirschke et al., 2013).

The global atmospheric methane burden has more than doubled since 1750. After a decade of near-zero growth (Dlugokencky et al., 2011; Heimann, 2011; Pison et al., 2013), global methane concentrations started to rise again in 2007 (Rigby et al., 2008; Bousquet et al., 2011; Frankenberg et al., 2011; Sussmann et al., 2012; Nisbet et al., 2014). Since then the methane burden has continuously increased with particularly strong growth in 2014 (Nisbet et al., 2015). The growth rate decline before 2007 has been interpreted as approaching a steady state with essentially constant global emissions since the mid-1980s (Dlugokencky et al., 1998). Causes for the renewed increase in global methane levels since 2007 are still poorly understood, which is reflected in, among other things, a persistent discrepancy between bottom–up and top–down estimates of methane emissions (e.g., Nisbet and Weiss, 2010; Kirschke et al., 2013).

Recent work provides evidence that there are likely two dominant contributors to the recent methane increase (Kirschke et al., 2013; Nisbet et al., 2014), namely increasing emissions from (i) tropical and boreal wetlands driven by precipitation and temperature anomalies

(Dlugokencky et al., 2009; Bousquet et al., 2011) and (ii) growing exploitation of fossil fuels (natural gas, oil, and coal) (e.g., Bergamaschi et al., 2013; see also references in the next paragraph). Even though they introduce interannual variability, biomass burning emissions are found to play only a minor role in explaining the positive long-term methane trend since 2007 (Dlugokencky et al., 2009; Bergamaschi et al., 2013), and global fire emissions slightly decreased between 2000 and 2012 (Giglio et al., 2013). Valuable information for methane source identification is provided by observations of methane isotopes (Dlugokencky et al., 2011; Levin et al., 2012). Since 2007 global methane has become more depleted in ^{13}C, which suggests a dominant role of growing ^{12}C-rich biogenic emissions, especially from wetlands and ruminants (Nisbet et al., 2014). The recent global average methane growth ($\sim 6\,\mathrm{ppb\,yr^{-1}}$) corresponds to an imbalance between emissions and sinks of about $16\,\mathrm{Tg\,yr^{-1}}$, which can be best reconciled with three decades of methane (isotopic) observations if attributed to increasing tropical wetland and fossil-fuel-related emissions (Dlugokencky et al., 2015a). Bergamaschi et al. (2013) attribute the renewed increase mainly to growing anthropogenic emissions (which are, however, significantly lower than estimates in bottom–up inventories) superimposed by interannual variations of wetland and biomass burning emissions. Using a GEOS-Chem model simulation, Bader et al. (2017) suggest that the recent methane increase is dominated by anthropogenic emissions from increased fossil fuel extraction.

Particularly important in this context is the strong increase in US oil and natural gas production starting in the mid-2000s (Moore et al., 2014; Wang et al., 2014), which is expected to continue through 2040 (US Energy Information Administration, 2014). This has been facilitated by the development of new extraction techniques (hydraulic fracturing and horizontal drilling), which involve additional fugitive methane emissions during flowback periods compared to conventional techniques (Field et al., 2014; Howarth, 2014). Several studies report that methane emissions from this industry are likely underestimated (Karion et al., 2013; Miller et al., 2013; Brandt et al., 2014; Kort et al., 2014; Pétron et al., 2014; Schneising et al., 2014; Turner et al., 2015). Furthermore, the rapid growth of coal exploitation since 2000 – especially in China (OECD/IEA, 2015) – potentially contributes to increasing methane emissions (Bergamaschi et al., 2013; Kirschke et al., 2013).

The major loss process for methane is oxidation by hydroxyl radicals (OH). Trends in the global OH concentration can have a large impact on the global methane budget (Rigby et al., 2008), but OH trends are difficult to be quantified due to the extremely short lifetime of OH and its control by many different drivers. IPCC (2013) reports no evidence for an OH trend from 1979 to 2011 based on methyl chloroform measurements. Consistent with this, Kai et al. (2011) infer a stable OH sink from 1998–2005 using CH_4 isotope observations. During 1998–2008, year-to-year changes in OH concentrations are found to be small (Montzka et al., 2011) and have only a minor impact on methane emissions inferred from inverse modeling (Bousquet et al., 2011).

Overall, evidence suggests that the renewed methane increase since 2007 is mainly caused by a combination of increased tropical wetland emissions and increased emissions from fossil fuel exploitation. However, the relative contribution of these two drivers remains highly uncertain (Kirschke et al., 2013). The goal of the research presented in this chapter is to quantify the contribution of increased oil and natural gas production emissions to the renewed methane increase since 2007. The approach applied comprises the combination of long-term FTIR measurements of methane with ethane observations. Ethane is a valuable tracer of thermogenic methane as both emissions are known to be strongly correlated

(Aydin et al., 2011; Simpson et al., 2012). This chapter is structured as follows: Section 3.2 introduces trend analysis methods, a pointing error correction scheme, and a simplified atmospheric model for methane and ethane simulations. Subsequently, results of long-term trend analysis for column-averaged methane and ethane are presented in Section 3.3, which is followed by optimized ethane and methane emission scenarios in Section 3.4. Finally, Section 3.5 summarizes results and gives relevant conclusions.

3.2 Methods

Long-term time series of column-averaged dry-air mole fractions of methane (XCH_4) and ethane (XC_2H_6) are retrieved from high-resolution mid-infrared FTIR spectra obtained at two NDACC sites: a northern midlatitude site (Zugspitze, Germany) and a southern midlatitude site (Lauder, New Zealand). Sampled air masses are representative of undisturbed atmospheric background conditions of northern and southern midlatitudes. At the high-altitude observatory Zugspitze (47.42° N, 10.98° E; 2964 m a.s.l.), a Bruker IFS 125HR spectrometer has been in operation since 1995 (Sussmann and Schäfer, 1997). The FTIR system at Lauder (45.04° S, 169.68° E; 370 m a.s.l.) is based on a Bruker IFS 120HR and was based on a Bruker IFS 120M before 2001 (Rinsland et al., 1998; Zeng et al., 2012). Retrieval strategies for column-averaged methane and ethane are harmonized for both measurement sites in order to obtain consistent results from Zugspitze and Lauder time series. Details on the retrieval strategies are described in Sect. 2.2.2. The vertical information obtained from FTIR measurements is characterized by means of their degrees of freedom for signal. On average, Zugspitze (Lauder) retrievals provide DOFS = 2.1 (DOFS = 1.8) for methane DOFS = 1.6 (DOFS = 1.2) for ethane.

Column-averaged dry-air mole fractions provide valuable information for source–sink inversion studies, as they are independent of variations in surface pressure, solar zenith angle, and humidity. To obtain column-averaged dry-air mole fractions, retrieved total columns of methane and ethane are divided by the corresponding dry pressure column, which is derived from ground pressure measurements and four times daily pressure–temperature–humidity profiles from the National Center for Environmental Prediction (NCEP) interpolated to FTIR measurement time. Long-term trends (see Fig. 3.5) are inferred from the time series of column-averaged dry-air mole fractions following the approach by Gardiner et al. (2008). First, seasonal cycles of XCH_4 and XC_2H_6 are removed by fitting and subtracting an intraannual model (third-order Fourier series). The second step involves a least squares fit of a linear trend to the deseasonalized time series and bootstrap resampling of the residuals to determine the linear trend uncertainty. Furthermore, annual growth rates of methane and ethane (see Fig. 3.6) are calculated as difference of annual mean mole fractions between the considered and the previous year as in Kirschke et al. (2013). Growth rate uncertainty is determined as quadratic sum of the standard errors (SE) of these two annual means. Additionally, annual running mean growth rates for each month are computed analogously to the approach of Rigby et al. (2008).

Remote sensing of column-averaged methane requires highly accurate measurements, as XCH_4 variations are very small compared to relatively high background XCH_4 levels (only $\sim 1\,\%$ seasonal or diurnal variability). Therefore, ground-based solar FTIR spectrometers have to be extremely well aligned to the center of the solar disk. Degradation in solar

tracking accuracy leads to errors in retrieved trace gas columns, relevant especially for gases with low variability such as methane. Within the scope of this thesis, a new pointing error correction scheme was applied to Zugspitze FTIR measurements. It was published in Reichert et al. (2015) and is briefly described in Sect. 3.2.1.

The source attribution of the renewed methane increase is a major goal of this thesis. To accomplish this task, an atmospheric two-box model was designed and published in Hausmann et al. (2016). This model enables the linkage of methane and ethane trend observations with their respective emission histories. Sect. 3.2.2 introduces the basic concept and underlying assumptions of this simplified atmospheric model.

3.2.1 Correction of FTIR Pointing Errors

Since solar absorption spectrometers use the sun as a light source, such instruments contain a device for active tracking of the solar position. In order to meet very high accuracy requirements, the line of sight of the spectrometer has to be exactly aligned to the center of the solar disk. However, this continuous alignment is generally prone to inaccuracies. Tracking errors in the vertical direction cause the air mass observed during the measurement to differ from the air mass assumed in the trace gas retrieval (Hase, 2000). To a good approximation, these air mass errors result in equal relative errors in the retrieved trace gas columns, which might exceed accuracy requirements. In this section, a correction method for pointing errors in solar absorption spectrometry is presented and validated.

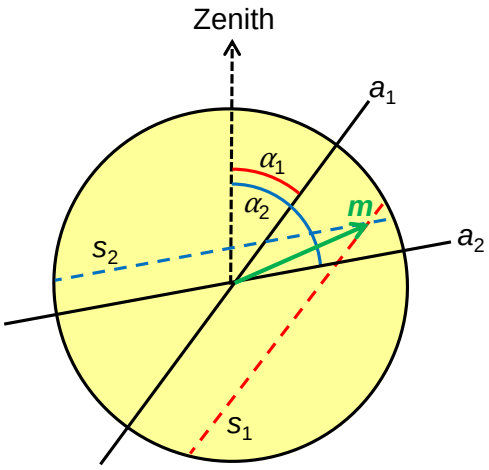

Figure 3.1: Schematic representation of the solar disk and the mispointing determination strategy. Solar line shifts are measured at times with solar axis orientations α_1 and α_2. The mispointing vector $\boldsymbol{m}$ is defined by the intersection of lines s_1 and s_2 parallel to the solar rotation axes a_1 and a_2 (adapted from Reichert et al., 2015).

The basic concept of the mispointing determination is illustrated in Fig. 3.1 and explained in the following. The mispointing vector $\boldsymbol{m}$, i.e., the vector from the solar disk center to the actual pointing coordinates, is fully described by a component parallel and a component perpendicular to the solar rotation axis. The perpendicular component can be determined from FTIR spectra by analyzing the rotational Doppler shift of solar absorption lines (Gisi et al., 2011). The challenge is to calculate the second mispointing vector component.

Therefore, multiple solar line shift measurements are combined, which are obtained at different orientations of the solar rotation axis. Each of these shift measurements constrains the mispointing vector to point to a straight line parallel to the solar rotation axis at a distance proportional to the measured solar line shift. The intersection coordinates of these lines define the full mispointing vector. In order to reduce errors due to uncertainties in solar line shift measurements, it is favorable to use larger sets of measured spectra to compute a mean mispointing vector. In this case, the mean mispointing is defined by the mean intersection coordinates of all pairs of measurements selected from a given set of spectra. Finally, the zenith mispointing component can be derived from the mispointing vector, which allows us to determine the actual zenith angle of the FTIR line of sight and the corresponding observed air mass. The main assumption of this concept is that the mispointing change within the considered time bin is negligible compared to the mispointing magnitude. Details on the pointing error correction can be found in Reichert et al. (2015). Here, main focus is put on its application to Zugspitze measurements.

Basically, there are two approaches to apply the pointing error correction scheme:

(i) A priori correction: the trace gas retrieval is repeated using the mispointing corrected solar zenith angle $\mathrm{sza_{cor}}$, which is determined by subtracting the zenith mispointing component from the apparent solar zenith angle (given by the ray trace calculation).

(ii) A posteriori correction: retrieved trace gas total columns are a posteriori corrected by multiplication with the air mass correction factor $\mathrm{am_{org}}/\mathrm{am_{cor}}$, where $\mathrm{am_{org}}$ is the uncorrected air mass and $\mathrm{am_{cor}} = 1/\cos(\mathrm{sza_{cor}})$ is the mispointing corrected air mass.

Beside the effect on the conversion of slant path to vertical column, the a priori correction method takes into account that the mispointing has slight influence on the ray tracing in the forward spectral calculations of the retrieval. These effects are not considered in the a posteriori method. Furthermore, the a posteriori correction uses an approximative air mass calculation, which could be replaced by more accurate air mass calculation methods especially at high solar zenith angles. However, trace gas columns corrected with the a posteriori approach show good consistency with results from the more sophisticated a priori approach. Therefore, a posteriori correction is a good approximation for total column retrievals, while a priori correction should be performed for profile retrievals.

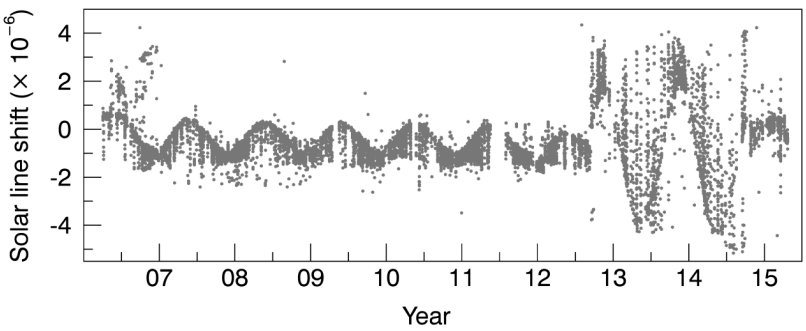

Figure 3.2: Time series of solar line shifts determined from Zugspitze FTIR spectra in the wavenumber region of 2400–3100 $\mathrm{cm^{-1}}$ (adapted from Reichert et al., 2015).

Due to a non-optimum configuration of the Zugspitze solar tracking optics, tracking accuracy was significantly degraded in the period from September 2012 to September 2014. In this

period, Zugspitze FTIR soundings were impacted by mispointing errors and resulting biases in retrieved trace gas columns. In September 2014, this issue could be resolved by replacing the quadrant diode by a Camtracker solar tracking system (Gisi et al., 2011). Solar line shifts derived from the Zugspitze FTIR time series are shown in Fig. 3.2, which clearly illustrates the period of non-optimum optics configuration. Measurements made with the more stable pre-September 2012 and post-September 2014 optics configurations show considerably smaller solar line shifts. Applying the pointing error correction scheme to the Zugspitze FTIR spectra enables to correct for mispointing induced errors. The uncorrected and a posteriori corrected column-averaged methane time series are presented in Fig. 3.3. For the period from September 2012 to September 2014, a mean mispointing in zenith direction of $-0.063°$ is derived, which causes a mean bias of -2.82 ppb in monthly mean XCH_4 data.

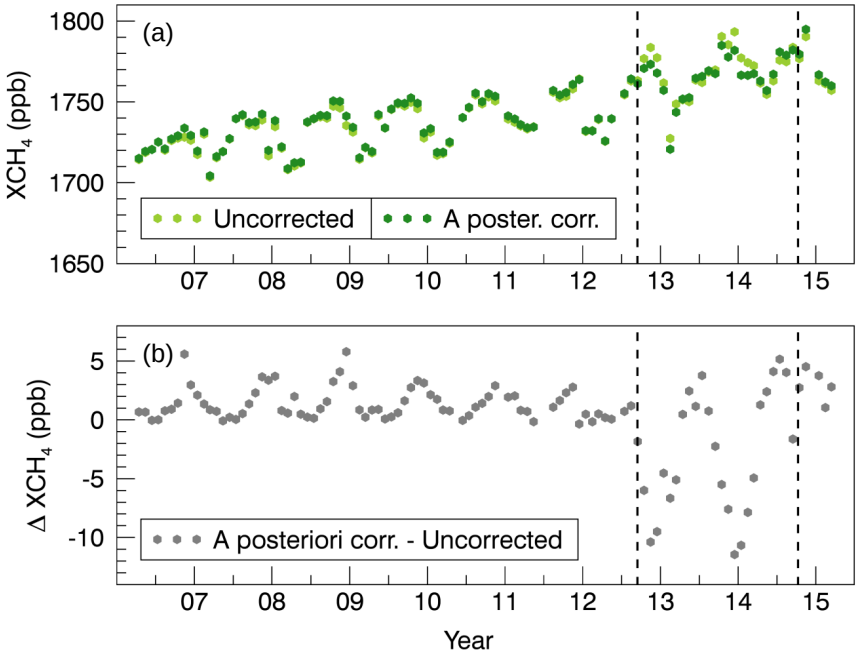

Figure 3.3: Pointing error correction applied to Zugspitze FTIR measurements: (a) Comparison of uncorrected and a posteriori corrected XCH_4 monthly means and (b) their difference. Vertical dashed lines mark changes in the optical configuration: off-axis mirror installation in September 2012 and Camtracker setup in September 2014 (adapted from Reichert et al., 2015).

Table 3.1: Validation of pointing error correction: XCH_4 trend with 95 % confidence intervals derived from the uncorrected, a posteriori, and a priori corrected time series at Zugspitze and Garmisch for the time period April 2006 to March 2015.

XCH_4 trend (ppb yr^{-1})	Uncorrected	A posteriori corr.	A priori corr.
Zugspitze	6.45 [5.84, 7.04]	6.07 [5.55, 6.59]	6.08 [5.56, 6.60]
Garmisch	5.22 [4.77, 5.65]	5.20 [4.74, 5.64]	5.19 [4.74, 5.63]

To validate the pointing error correction method, column-averaged methane trends are compared for uncorrected and corrected time series at Zugspitze (47.42° N, 10.98° E; 2964 m a.s.l.)

and nearby Garmisch site (47.48° N, 11.06° E; 743 m a.s.l.). Trend consistency for both sides was shown for measurements before September 2011 by Sussmann et al. (2012). Table 3.1 compiles trend estimates from April 2006 to March 2015. The Zugspitze XCH_4 trend is reduced from 6.45 [5.84, 7.04] ppb yr^{-1} to 6.07 [5.55, 6.59] ppb yr^{-1} when applying the pointing error correction, while this has only minor impact on the Garmisch trend (i.e., no major solar tracking issues). Performing the pointing error correction successfully restores trend consistency between Garmisch and Zugspitze for the considered period.

In this section, the new pointing error correction method was successfully applied to the Zugspitze methane time series reducing artifacts due to solar tracking inaccuracies. Zugspitze time series presented in the following (see Sect. 3.3) are generated using the a priori correction method. The pointing error correction is applicable to solar absorption measurements in mid-infrared and near-infrared spectral regions. It will be of particular benefit to refine existing records of high-accuracy-and-precision FTIR soundings for the purpose of improved greenhouse gas trend analysis and source–sink inversions.

3.2.2 Atmospheric Two-Box Model

To investigate which kind of emissions drive the renewed methane increase since 2007, long-term observations of methane are combined with observations of ethane, i.e., a tracer of thermogenic methane emissions. In Sect. 3.4.2 an atmospheric two-box model is applied to simulate hemispheric time series of column-averaged methane and ethane and link them to corresponding emission histories. This simplified atmospheric model is described in detail in this section.

Model Setup. The presented two-box model is based on the work of Aydin et al. (2011) and Kai et al. (2011). Two well-mixed hemispheres, each with distinct methane and ethane sources and sinks, are interconnected by interhemispheric exchange with a timescale of about 1 year (Fig. 3.4). Annual growth rates of hemispheric mean column-averaged mole fractions are determined by hemispheric emissions, chemical loss, and interhemispheric exchange, as expressed in the following equations for the Northern and the Southern Hemisphere:

$$\frac{\mathrm{d}X_\mathrm{N}}{\mathrm{d}t} = E_\mathrm{N} - \frac{X_\mathrm{N}}{\lambda^*} - \frac{X_\mathrm{N} - X_\mathrm{S}}{\tau_{ex}} \tag{3.1}$$

$$\frac{\mathrm{d}X_\mathrm{S}}{\mathrm{d}t} = E_\mathrm{S} - \frac{X_\mathrm{S}}{\lambda^*} + \frac{X_\mathrm{N} - X_\mathrm{S}}{\tau_{ex}} \tag{3.2}$$

Here, X_N and X_S are annual mean column-averaged mole fractions in the Northern and Southern Hemisphere, λ^* is the tracer atmospheric lifetime, and τ_{ex} is the interhemispheric exchange time. E_N and E_S are total hemispheric tracer emissions (in units of ppb yr^{-1}). The latter can be determined from global emissions (E_glob in Tg yr^{-1}) according to $E_\mathrm{N} = f_\mathrm{N} \cdot E_\mathrm{glob} \cdot 2/c_\mathrm{em}$ and $E_\mathrm{S} = (1 - f_\mathrm{N}) \cdot E_\mathrm{glob} \cdot 2/c_\mathrm{em}$ (with the fraction f_N of global emissions in the Northern Hemisphere and the emission unit conversion factor c_em in Tg ppb^{-1}). Model parameters applied are summarized in Table 3.2 for methane and in Table 3.3 for ethane. The parameter uncertainty is given as stated in the cited references or, if not included there, as a range of literature values. More details are given in the following paragraphs.

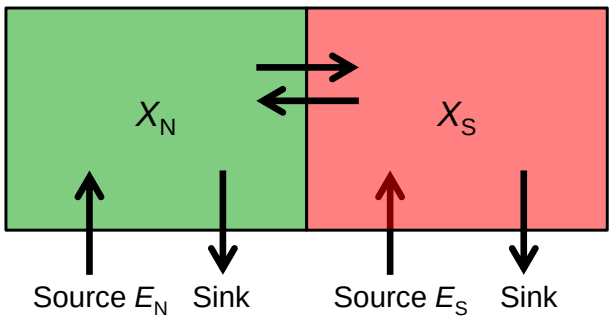

Figure 3.4: Schematic display of the atmospheric two-box model: two well-mixed hemispheres with methane and ethane sources and sinks and interhemispheric exchange.

Atmospheric Lifetime. The atmospheric lifetimes of methane and ethane are determined mainly by the rate of OH oxidation, which is the primary sink of atmospheric methane and ethane. OH concentrations have not shown any large interannual variability since the late 1970s (IPCC, 2013, p. 167). Therefore, a constant atmospheric lifetime of methane (8.9 ± 1.0 years; Turner et al., 2015) and ethane (2.6 ± 0.6 months; Xiao et al., 2008) is applied in the two-box model. Assuming a constant lifetime implies that potential interannual variability of OH is projected to the modeled source term (see Bergamaschi et al., 2013; Dlugokencky et al., 1998). However, Kai et al. (2011) found no significant difference between two-box model simulations with constant and time-dependent methane lifetime including the feedback of methane on OH concentrations.

Initial Emissions. In the case of methane, initial global emissions are taken from top–down emission estimates in the latest IPCC report (IPCC, 2013, p. 507). About 70 % of global methane emissions are located in the Northern Hemisphere (Kai et al., 2011). In the case of ethane, about 80 % of global emissions originate in the Northern Hemisphere (Xiao et al., 2008). Three ethane source categories are distinguished: fossil fuel extraction (oil, gas, and coal), biomass burning, and biofuel use. Each ethane source exhibits a characteristic latitudinal distribution and therefore has a distinct northern hemispheric emission fraction: f_N amounts to 95 %, 90 %, 81 %, and 53 %, respectively, for emissions from oil and natural gas, coal, biofuel use, and biomass burning. Major ethane sources in the Southern Hemisphere are interhemispheric transport and biomass burning (Xiao et al., 2008). Initial global ethane emissions are compiled from the following emission inventories:

(i) Fossil-fuel-related emissions are provided by Schwietzke et al. (2014) including emissions from the extraction of coal (molar ethane-to-methane ratio EMR = 0.5 %), oil (EMR = 21.3 %), and natural gas (mean ethane content of 7.3 % at a global fugitive emission rate of 5 %). This bottom–up inventory supplies annual emissions up to 2011. Estimates for the years 2012–2014 are obtained by extrapolation according to the annual percentage change in the global production of coal (OECD/IEA, 2015) and of oil and natural gas (US Energy Information Administration, 2015).

(ii) Biomass burning emissions are taken from the Global Fire Emission Database GFED4s (van der Werf et al., 2010; Giglio et al., 2013) in combination with emission factors from Akagi et al. (2011).

(iii) Biofuel use emissions are compiled from the linearly extrapolated activity data in Fernandes et al. (2007) together with appropriate emission factors from Andreae and Merlet (2001).

Minor Ethane Emissions. Apart from the major ethane sources described above, minor ethane emissions originate from oceanic and biogenic sources. These are negligibly small (Rudolph, 1995; Xiao et al., 2008) and not considered in this thesis. Furthermore, possible ethane emissions from geologic outgassing are neglected based on the following considerations: Simpson et al. (2012) state that a large geologic ethane source is unlikely, but more investigation would be required for confirmation. Recently, Nicewonger et al. (2016) report preindustrial geologic ethane emissions of 2.2–3.5 $\mathrm{Tg\,yr^{-1}}$, similar to a present-day estimate by Etiope and Ciccioli (2009). However, the temporal variability of geologic emissions is poorly known and assuming constant source strength may be reasonable (Nicewonger et al., 2016). Implementing a two-box model scenario with an additional constant geologic ethane source does not considerably change ($< 0.5\,\%$) the derived optimized increase in oil and natural gas ethane emissions since 2007 (see Sect. 3.4.2). On timescales of glacial–interglacial transitions fluctuations in geologic emissions are possible in response to variable crustal loading or continental shelf exposure (Nicewonger et al., 2016). Such long-term variations can be linearly approximated for the much shorter period considered here (7 years). In a second scenario, hence, geologic emissions are assumed to linearly increase since 2007. If this linear increase is chosen strong enough to fully account for the observed positive ethane trend in 2007–2014, geologic emissions would have to increase by about 190 %. An increase of this strength does not seem to be reasonable and is not evident from review of relevant literature. Consequently, geologic ethane emissions are not considered as done in several previous ethane studies (Pozzer et al., 2010; Aydin et al., 2011; Franco et al., 2015).

High-Latitudinal Response Ratios. With the two-box model presented above, hemispheric averages of methane and ethane can be simulated. To compare model output with Zugspitze and Lauder observations, which are representative of high latitudes (30–90° N or S), modeled hemispheric means have to be translated to high-latitudinal averages. High-latitudinal ethane averages respond with different efficiency to changes in ethane emissions depending on the latitudinal distribution of each ethane source (i.e., fossil fuel and biofuel ethane emissions are concentrated in northern midlatitudes, biomass burning emissions primarily originate in the tropics). Response ratios of high-latitudinal ethane averages to changes in hemispheric means, which were determined by Aydin et al. (2011) for different ethane sources, are applied in this thesis. In contrast to ethane, methane has a much longer atmospheric lifetime and therefore a relatively small interhemispheric gradient of about 4 % (Kai et al., 2011) compared to 70 % for ethane (Simpson et al., 2012). Consequently, the gradient between high latitudes and the tropics is relatively weak for methane. Ratios of high northern latitudinal averages to hemispheric averages amount to 1.02 for methane (derived from Dlugokencky et al., 2015b) and to 1.38 for ethane (derived from Simpson et al., 2012). As first approximation, modeled hemispheric methane averages are assumed to be representative of high-latitudinal averages. This assumption seems to be valid, in particular, as only total methane emissions are considered avoiding issues with distinct latitudinal distributions of different methane sources.

Table 3.2: Uncertainty of methane two-box model parameters and implied trend uncertainty.

Model parameter	Reference	Parameter range	Trend ($\mathrm{ppb\,yr^{-1}}$)
Lifetime (yr)	Turner et al. (2015)	8.9 [7.9, 9.9]	6.21 [5.88, 6.53]
Interh. exchange (yr)	Patra et al. (2009)	0.98 [0.55, 1.41]	6.21 [6.10, 6.32]
Conversion c_{em} ($\mathrm{Tg\,ppb^{-1}}$)	Patra et al. (2011)	2.845 [2.767, 2.870]	6.21 [6.39, 6.16]
NH emission frac. (%)	Kai et al. (2011)	0.70 [0.65, 0.75]	6.21 [6.14, 6.28]
Global emission ($\mathrm{Tg\,yr^{-1}}$):			
1980s	IPCC (2013, p. 507)	541 [500, 592]	6.21 [7.51, 4.60]
1990s	IPCC (2013, p. 507)	554 [529, 596]	6.21 [7.87, 3.42]
2000s	IPCC (2013, p. 507)	553 [526, 569]	6.21 [3.55, 7.79]
1980–2010	IPCC (2013, p. 507)	all min/max	6.21 [6.51, 3.38]

Table 3.3: Uncertainty of ethane two-box model parameters and implied trend uncertainty (given in 10^{-2} $\mathrm{ppb\,yr^{-1}}$).

Model parameter	Reference	Parameter range	Trend
Lifetime (month)	Xiao et al. (2008)	2.6 [2.0, 3.2]	2.27 [1.79, 2.72]
Interh. exchange (yr)	Patra et al. (2009)	0.98 [0.55, 1.41]	2.27 [2.11, 2.35]
Conversion c_{em} ($\mathrm{Tg\,ppb^{-1}}$)	Rudolph (1995)	18 [10, 26]	2.27 [4.08, 1.57]
NH emission fraction (%):			
Biomass burning	van der Werf et al. (2010)	53 [48, 58]	2.27 [2.26, 2.27]
Biofuel use	Xiao et al. (2008)	81 [73, 89]	2.27 [2.26, 2.27]
Coal	Schwietzke et al. (2014)	90 [81, 99]	2.27 [2.26, 2.27]]
Oil and gas	Schwietzke et al. (2014)	95 [86, 100]	2.27 [2.11, 2.35]
Global emission ($\mathrm{Tg\,yr^{-1}}$):			
Biomass burning	van der Werf et al. (2010)	± 65 %	2.27 [2.19, 2.34]
Biofuel use	Fernandes et al. (2007)	± 75 %	2.27 [2.22, 2.31]
Coal	Schwietzke et al. (2014)	± 90 %	2.27 [2.23, 2.30]
Oil	Schwietzke et al. (2014)	± 40 %	2.27 [2.19, 2.35]
Gas	Schwietzke et al. (2014)	± 50 %	2.27 [2.01, 2.53]

3.3 Long-Term Trend Analysis Results

Time series of monthly mean column-averaged dry-air mole fractions of methane and ethane are presented in Fig. 3.5 as derived from Zugspitze and Lauder FTIR measurements. In addition, deseasonalized time series and linear trend estimates are shown. The trend analysis is performed for two distinct time periods (1999–2006 and 2007–2014), which correspond to methane trend turning points published in earlier work (e.g., Rigby et al., 2008; Dlugokencky et al., 2011; Sussmann et al., 2012; IPCC, 2013). Trend analysis results are compiled in Table 3.4 and can be summarized as follows: the stagnation of methane growth from 1999 to 2006 and the renewed methane increase since 2007 are consistently observed at both sites. The positive methane trend since 2007 (6.2 [5.6, 6.9] ppb yr^{-1} at Zugspitze; 6.0 [5.3, 6.7] ppb yr^{-1} at Lauder) persists until the end of 2014 and agrees well with the reported global surface methane trend (e.g., Dlugokencky et al., 2011; Nisbet et al., 2014). In the case of ethane, a weakly negative trend is found for the period 1999–2006 with equal magnitudes at Zugspitze (-0.5 [-1.0, 0.1] $\times 10^{-2}$ ppb yr^{-1}; statistically insignificant) and Lauder (-0.4 [-0.7, -0.2] $\times 10^{-2}$ ppb yr^{-1}; statistically significant). While this negative ethane trend persists at Lauder in the period 2007–2014, a trend reversal is observed at Zugspitze resulting in a statistically significant positive trend of 2.3 [1.8, 2.8] $\times 10^{-2}$ ppb yr^{-1} for 2007–2014. The ethane trend turning point at the beginning of 2007 is chosen in analogy to the applied methane trend periods. This choice is corroborated by the minimum (October 2006) in the two-year running mean time series of monthly XC_2H_6 data.

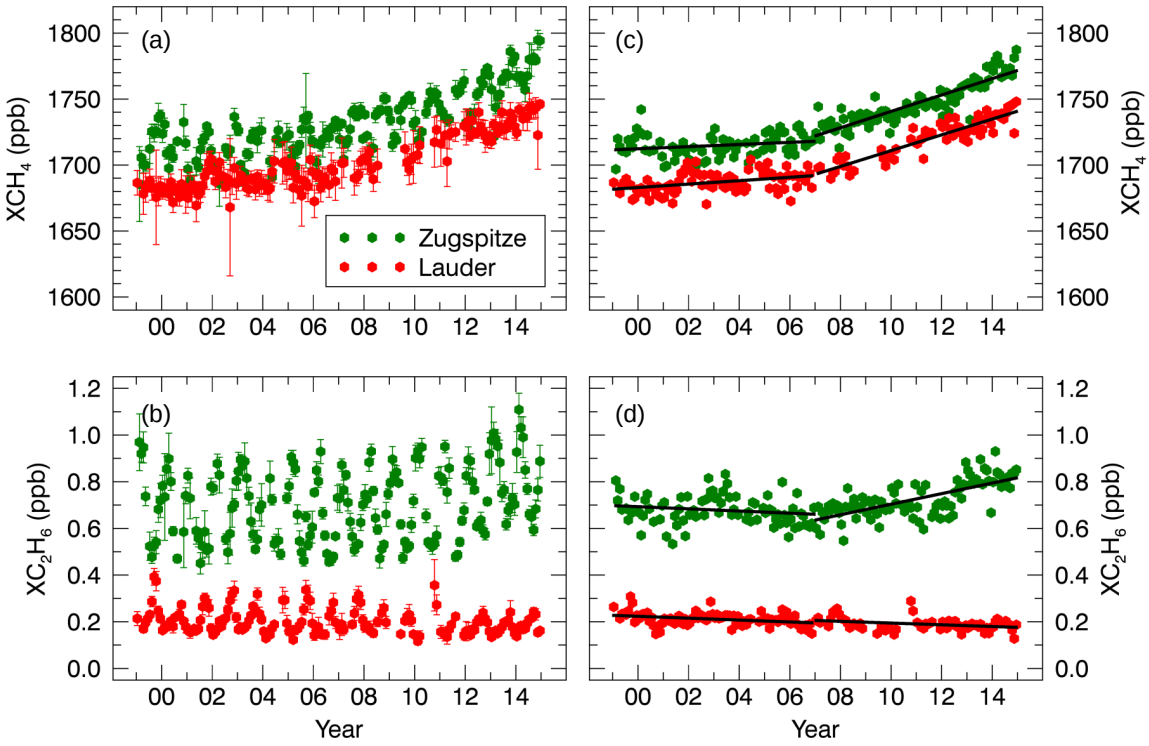

Figure 3.5: Time series of monthly mean column-averaged dry-air mole fractions of (a) methane and (b) ethane measured at Zugspitze and Lauder. Error bars indicate statistical standard errors of monthly means (± 3 SE $= \pm 3$ SD $/ \sqrt{n}$ with sample size n and standard deviation SD). Deseasonalized time series of (c) methane and (d) ethane are displayed along with linear trend estimates (black lines). See Table 3.4 for trend magnitudes (Hausmann et al., 2016).

Table 3.4: Linear trend estimates and 95 % confidence intervals for column-averaged methane and ethane time series as well as for the resulting interhemispheric gradients (IHG-XCH_4 and IHG-XC_2H_6, defined as difference of Zugspitze and Lauder time series).

	Trend 1999–2006 (ppb yr^{-1})		Trend 2007–2014 (ppb yr^{-1})	
	Zugspitze	Lauder	Zugspitze	Lauder
Methane	0.8 [0.0, 1.6]	1.3 [0.6, 1.9]	6.2 [5.6, 6.9]	6.0 [5.3, 6.7]
Ethane ($\times 10^{-2}$)	−0.5 [−1.0, 0.1]	−0.4 [−0.7, −0.2]	2.3 [1.8, 2.8]	−0.4 [−0.6, −0.1]
IHG-XCH_4	−0.6 [−1.9, 0.5]		0.7 [−0.4, 1.8]	
IHG-XC_2H_6 ($\times 10^{-2}$)	0.1 [−0.5, 0.7]		2.7 [2.1, 3.3]	

Annual Growth Rates. Figure 3.6 presents annual growth rates of column-averaged methane and ethane derived from Zugspitze and Lauder time series. Interannual variability of annual growth rates is lower in the 2007–2014 period compared to the 1999–2006 period in all cases with the exception of the Lauder ethane time series (low variability over the full time period). In the 2007–2014 period methane growth rates at Zugspitze and Lauder are generally positive and increasing, while oscillating around zero before. Consistent with the results of Nisbet et al. (2015), an extraordinarily high methane growth rate is observed at Zugspitze in 2014 (13.1 ppb yr^{-1}). In contrast, methane and ethane growth rates at Lauder as well as ethane growth at Zugspitze are not particularly high in 2014.

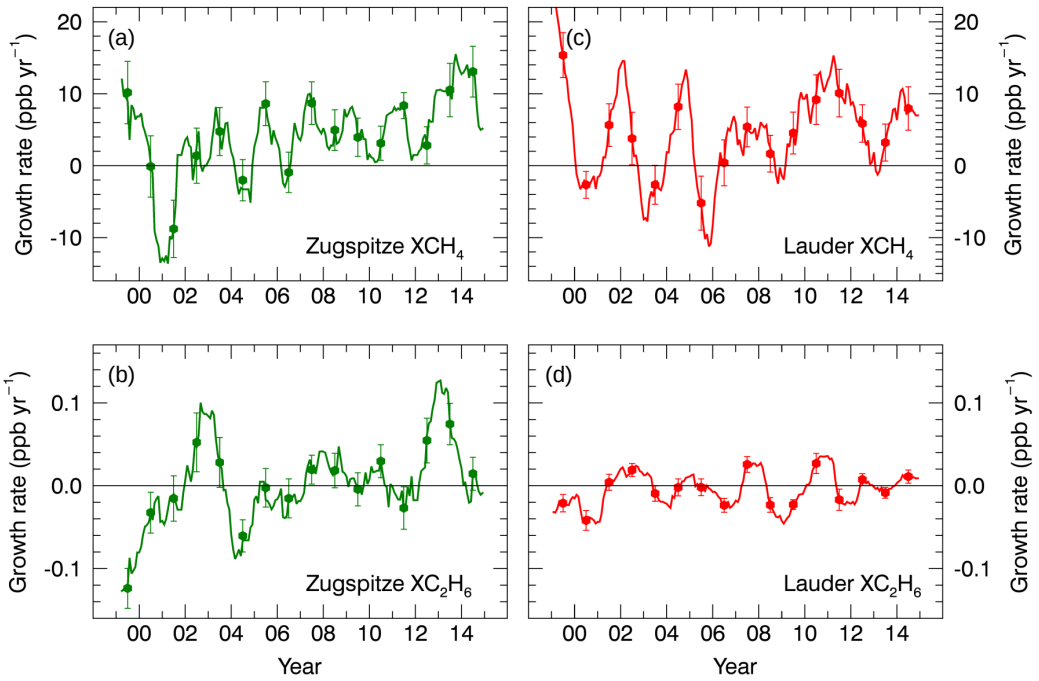

Figure 3.6: Annual growth rates of (a) column-averaged methane and (b) ethane observed at Zugspitze as well as growth rates for (c) methane and (d) ethane observed at Lauder. Annual increases (filled circles) are calculated as the difference between two consecutive annual means. Annual running mean growth rates are depicted as solid lines (Hausmann et al., 2016).

Trends and Biomass Burning Events. Derived methane and ethane trends could be affected by the interannual variability of biomass burning emissions, especially if strong biomass burning events occur at the beginning or end of the considered time period. This influence on Zugspitze and Lauder time series is investigated using the presented annual ethane growth rates (see Fig. 3.6). Ethane growth rates at Zugspitze are mostly positive in the 2007–2014 period and mostly negative in the 1999–2006 period with exception of the years 2002 and 2003. This strong ethane growth could be related to boreal biomass burning events in this time period (Simmonds et al., 2005; Simpson et al., 2006). A similar pattern is observed in 2012 and 2013, which is possibly also caused by a biomass burning emission peak in boreal Asia as reported in the Global Fire Emission Database GFED4s (Giglio et al., 2013). At Lauder, relatively high ethane column-averaged mole fractions and associated higher growth rates are observed in October and November 2010 (see Figs. 3.5 and 3.6). Similar peaks in late 2010 are present in the time series of total columns of biomass burning tracers HCN and CO at Lauder. This suggests that a biomass burning event caused these high ethane observations. Biomass burning emission data from the Global Fire Emission Database reveal no strong fire activity in 2010 within the region of Australia and New Zealand. In contrast, the monthly burned area record is exceptionally large for August and September 2010 in Southern Hemisphere South America, probably connected to a strong La Niña event. Related biomass burning emissions can be convected to the upper troposphere and transported by westerly winds to New Zealand within 1–2 weeks (Rinsland et al., 1998, 2001; Staudt et al., 2002). The dominance of such transport patterns during the respective measurement period in 2010 is confirmed using backward trajectories (Stein et al., 2015; available at http://ready.arl.noaa.gov/HYSPLIT_traj.php). In summary, strong biomass burning events introduce interannual variability in the presented ethane and methane time series but should not have major effects on trend estimates as they primarily occur in the middle of the considered time periods and not at their beginning or end. Furthermore, there are no indications for a strong positive trend in biomass burning emissions over the considered time period (see Sect. 3.4.1).

Interhemispheric Gradients. A sensitive tool to locate changing emissions is the study of trends in spatial gradients of methane and ethane. The interhemispheric gradient (IHG) is defined as the difference between northern and southern high-latitude averages (30–90° N/S) of methane (IHG-XCH_4) and ethane (IHG-XC_2H_6), respectively. Assuming that Zugspitze (Lauder) observations are representative of the northern (southern) high-latitude XCH_4 and XC_2H_6 averages, IHG-XCH_4 and IHG-XC_2H_6 can be calculated as difference in monthly mean time series between Zugspitze and Lauder. This assumption is supported by the following argumentation: ethane is approximately well-mixed in high northern and southern latitudes (Aydin et al., 2011) as its lifetime of 2.6 months (Xiao et al., 2008) exceeds zonal mixing timescales of about 2 weeks (Williams and Koppmann, 2007). Methane has an even longer lifetime of about 9 years (Prather et al., 2012) and is therefore well-mixed north of 30° N and in the Southern Hemisphere (Simpson et al., 2002; Saito et al., 2012). Trend analysis for the interhemispheric gradients reveals no significant trend for IHG-XCH_4 in both time periods considered, while the trend of IHG-XC_2H_6 is statistically insignificant in 1999–2006 and becomes significantly positive in 2007–2014 (see Table 3.4). In relation to methane emissions, findings on the trend behavior of ethane and its interhemispheric gradient can be interpreted as follows. Ethane sources are predominantly located in the Northern Hemisphere (80 % of global emissions). In contrast to methane,

ethane cannot completely mix over both hemispheres, as its lifetime is short compared to the interhemispheric exchange time of approximately 1 year (Tans, 1997; Aydin et al., 2011). Ethane concentrations have continuously declined since the 1980s, which can be explained by reduced fossil-fuel-related emissions (Aydin et al., 2011; Simpson et al., 2012; Helmig et al., 2014). Negative ethane trends for 1996–2006 are also reported by Angelbratt et al. (2011) from FTIR observations at four European NDACC stations. Due to the high altitude of Zugspitze observatory (2964 m a.s.l.), the Zugspitze time series represents the background conditions of free tropospheric ethane influenced by long-range emission transport. The recent ethane trend reversal identified at the Zugspitze observatory is similarly observed at the high-altitude NDACC station of Jungfraujoch, Swiss Alps (Franco et al., 2015). Furthermore, long-term in situ measurements in the US show increasing ethane concentrations over the past years linked with increasing natural gas production (Vinciguerra et al., 2015). Overall, these time series point to a recent ethane increase in the Northern Hemisphere, which was recently confirmed by global surface ethane measurements (Helmig et al., 2016). Consistent with observations in Lauder, a continuing ethane decline is observed at two other NDACC FTIR stations in the Southern Hemisphere: the total-column ethane trend is significantly negative in 1999–2006 and weakly negative but not significant for 2007–2014 in Arrival Heights, Antarctica (Zeng et al., 2012). A similar trend behavior has been observed at Wollongong, Australia (N. Jones, pers. comm., 2015).

Overall, the significant positive trend of IHG-XC_2H_6 for 2007–2014 suggests increasing ethane emissions in the Northern Hemisphere, where most fossil-fuel-related ethane sources are located. Using ethane as a tracer for thermogenic methane emissions, the presented simultaneous increase in methane and ethane in the Northern Hemisphere since 2007 points to a potential contribution of thermogenic methane sources to the methane burden increase since 2007.

3.4 Contribution of Oil and Gas Emissions

3.4.1 Ethane-to-Methane Ratio Analysis

Thermogenic and biogenic methane sources can be separated using their ethane-to-methane emission ratios (Schoell, 1980). While there are no associated ethane emissions during microbial methanogenesis, ethane is emitted together with methane from thermogenic sources, i.e., primarily from fossil fuel extraction. The molar ethane-to-methane ratio (EMR) is larger than 1.0 % for largely thermogenic methane sources (Kang et al., 2014; Yacovitch et al., 2014), whereas biogenic sources are characterized by EMR values below 0.1 % (Taylor et al., 2000; Jackson et al., 2014). For atmospheric measurements in spatial and temporal proximity to an emission source, the molar ethane-to-methane ratio of this source (EMR_{src}) can be determined from the linear regression slope in a scatterplot of ethane against methane mole fractions. This technique has been applied in several studies to compare ethane-to-methane ratios of atmospheric measurements with ratios in nearby natural gas pipelines (e.g., Wennberg et al., 2012).

Scatterplots of deseasonalized monthly mean XCH_4 and XC_2H_6 at Zugspitze and Lauder are shown in Fig. 3.7 for the periods 1999–2006 and 2007–2014. Table 3.5 summarizes results of the linear regression and correlation analysis. A significant ethane–methane correlation with

a coefficient of determination (R^2) of 0.44 is derived for the 2007–2014 period at Zugspitze, while no significant correlation is found for the 1999–2006 period at Zugspitze and for either period at Lauder. The regression slope for the 2007–2014 data at Zugspitze amounts to $0.31 \pm 0.07\,\%$ (uncertainty given as twice the standard deviation SD, i.e., $\pm\, 2 \times \mathrm{SD}$) and is significantly larger than 0.1 %. In contrast, slopes do not significantly differ from zero for 1999–2006 at Zugspitze and for either period at Lauder.

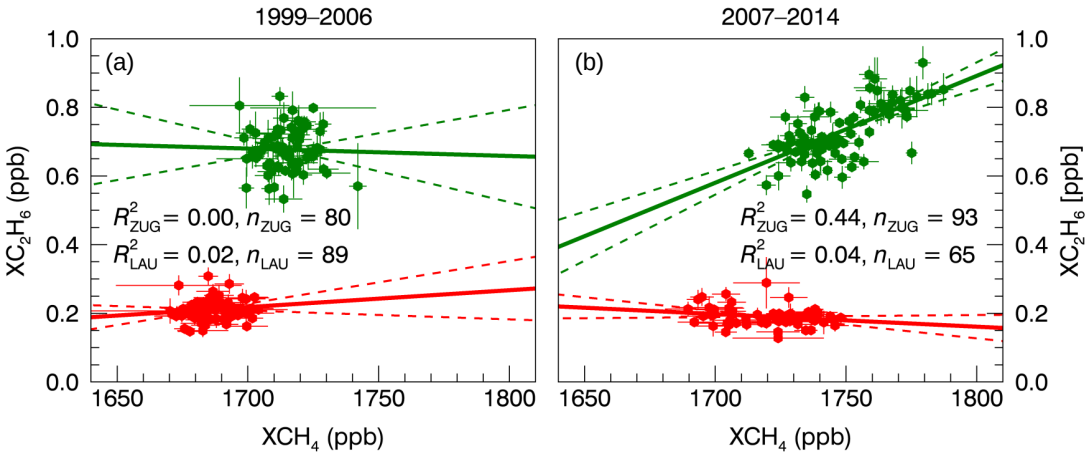

Figure 3.7: Scatterplots of monthly mean column-averaged ethane and methane derived from deseasonalized time series at Zugspitze (green) and Lauder (red) for the time periods of (a) 1999–2006 and (b) 2007–2014. Solid (dashed) lines show linear regression results (uncertainty range of ±2 SD). Statistics are summarized in Table 3.5 (Hausmann et al., 2016).

Table 3.5: Ethane–methane correlation analysis and linear regression results.

	1999–2006		2007–2014	
	Zugspitze	Lauder	Zugspitze	Lauder
Number of monthly means n	80	89	93	65
Pearson's correlation coefficient R	−0.03	0.14	0.66	−0.21
Quality measure $R \cdot \sqrt{(n-2)/(1-R^2)}$	−0.27	1.31	8.45	−1.71
t value for 99 % confidence level	2.64	2.63	2.63	2.66
Sign. correlation (99 % confidence)?	no	no	yes	no
Linear regression slope	−0.02 %	0.05 %	0.31 %	−0.04 %
Uncertainty (± 2 SD)	± 0.16 %	± 0.08 %	± 0.07 %	± 0.04 %

As the measurements analyzed here represent background conditions (i.e., are not observed in close proximity to sources), it is not possible to directly infer the ethane-to-methane ratio of the source from the regression slope. Methane and ethane time series measured at remote sites are subject to long-term trends of emissions, photochemical loss (reaction with OH), and mixing during atmospheric transport. Background ethane-to-methane ratios

($\mathrm{EMR_{bg}}$) can therefore differ significantly from the original source emission ratio (Borbon et al., 2013; Yokelson et al., 2013) and are likely smaller than $\mathrm{EMR_{src}}$ due to the different lifetimes of methane and ethane (Wang and Zeng, 2004; Parrish et al., 2007). Nevertheless, a rough estimate of the source ethane-to-methane ratio can be obtained using a simple heuristic model: in a well-stirred reactor, emission pulses are instantaneously mixed in the troposphere followed by first-order chemical loss in the well-mixed troposphere (Parrish et al., 2007). The source ethane-to-methane ratio can then be inferred from the measured $\mathrm{EMR_{bg}}$ and the rate constants for the reaction with OH ($k_{\mathrm{C_2H_6}} = 1.83 \times 10^{-13}\,\mathrm{cm^3\,molecule^{-1}\,s^{-1}}$ and $k_{\mathrm{CH_4}} = 3.68 \times 10^{-15}\,\mathrm{cm^3\,molecule^{-1}\,s^{-1}}$; Sander et al. (2011)):

$$\mathrm{EMR_{src}} = \mathrm{EMR_{bg}} \cdot k_{\mathrm{C_2H_6}}/k_{\mathrm{CH_4}} \tag{3.3}$$

This simplification is applicable as methane and ethane are long-lived compared to the period of about 30 days required for the complete dispersion of an emission pulse throughout the hemispheric troposphere (Parrish et al., 2007). As a first approximation, such long-lived trace gases can mix within a hemisphere so that details of transport and mixing become unimportant (Stohl et al., 2002), especially if looking at monthly or annual means. Assuming a constant source emission ratio during 2007–2014 and applying the well-stirred reactor model, the $\mathrm{EMR_{bg}}$ determined from the Zugspitze regression slope ($0.31 \pm 0.07\,\%$, $\pm 2 \times \mathrm{SD}$ uncertainty) translates to an $\mathrm{EMR_{src}}$ of 12–19 %. This is within the EMR value range of 1–25 % known to be typical for oil and gas production emissions (Xiao et al., 2008), while coal mining emissions exhibit lower EMR values of below 1 % (Xiao et al., 2008; Schwietzke et al., 2014).

The derived EMR range (12–19 %) would also be in line with a potential contribution from biomass burning emissions (EMR = 4–18 %; Akagi et al., 2011). However, there are no indications for a strong positive trend in biomass burning emissions during 2007–2014 that could have caused the observed ethane increase since 2007: biomass burning emissions from the Global Fire Emission Database GFED4s (van der Werf et al., 2010; Giglio et al., 2013) modestly decrease during 2007–2014 (5-year averages of global $\mathrm{CH_4}$ biomass burning emissions amount to $14.2\,\mathrm{Tg\,yr^{-1}}$ for 2007 and $13.4\,\mathrm{Tg\,yr^{-1}}$ for 2012). Furthermore, columns of the biomass burning tracer CO do not exhibit a significant trend during 2007–2014 (-4.6 [-10.0, 1.0] $\times 10^{15}\,\mathrm{molecules\,cm^{-2}\,yr^{-1}}$; 95 % confidence interval) as determined from the Zugspitze FTIR time series. Consistent results are obtained at the high-altitude NDACC FTIR station of Jungfraujoch (Swiss Alps, 46.5° N), where neither biomass burning tracer CO and HCN present an upturn in this time period (Franco et al., 2015). The 2007–2014 trend of CO and HCN total columns at Jungfraujoch amounts to -5.2 [-10.1, -0.3] $\times 10^{15}\,\mathrm{molecules\,cm^{-2}\,yr^{-1}}$ and 0.003 [-0.029, 0.033] $\times 10^{15}\,\mathrm{molecules\,cm^{-2}\,yr^{-1}}$, respectively. These trend estimates are determined via the bootstrap method from Jungfraujoch data available from the NDACC database (E. Mahieu, pers. comm., 2015; the CO time series is an extension of Dils et al., 2011).

In summary, methane and ethane time series are significantly correlated for the period from 2007 to 2014 at Zugspitze. The regression slope can be used to derive a source ethane-to-methane ratio which corresponds to thermogenic methane emissions from oil and natural gas sources. In contrast, no significant ethane–methane correlation is found for Zugspitze data during 1999–2006 and for Lauder data in both periods. Consequently, it can be concluded that thermogenic methane fugitive emissions from fossil fuel production and distribution have significantly contributed to the renewed methane increase since 2007.

3.4.2 Optimized Emission Scenarios

To quantify the contribution of thermogenic methane emissions from growing oil and natural gas industries to the renewed methane increase since 2007, it is proceeded as follows: First, the ethane emission change that is necessary to explain the positive ethane trend observed at Zugspitze since 2007 is determined using an atmospheric two-box model. These additional ethane emissions not included in the emission inventories are then fully attributed to growing emissions from oil and natural gas exploitation. As a second step, a reasonable ethane-to-methane ratio for oil and natural gas emissions is applied to quantify the associated thermogenic methane emission increase and relate it to the total methane emission increase during 2007–2014.

Two-Box Model Simulation. Hemispheric column-averaged methane and ethane time series are simulated with the help of the atmospheric two-box model described in detail in Sect. 3.2.2. The two-box model enables the linkage of the 2007–2014 trend observations at Zugspitze and Lauder with the respective emission histories of ethane and methane. Our knowledge for developing accurate initial emission inventories is incomplete. Therefore, simulated and observed time series of atmospheric methane and ethane mole fractions are likely to diverge. In order to reconstruct the observed 2007–2014 trend of XCH_4 and XC_2H_6 using the atmospheric two-box model, an optimized emission scenario is developed by minimizing the difference between modeled and observed trends at Zugspitze. The modeled trend is determined from the modeled annual methane or ethane time series by linear regression. Annual global emissions from 2007 to 2014 are optimized by adding a linear emission growth since 2007 to the initial emission history, i.e.,

$$E_{\mathrm{CH_4,\,tot,\,opt}}(t) = E_{\mathrm{CH_4,\,tot,\,ini}}(t) + (t - t_0)\, s_{\mathrm{CH_4}} \tag{3.4}$$

$$E_{\mathrm{C_2H_6,\,oil\,\&\,gas,\,opt}}(t) = E_{\mathrm{C_2H_6,\,oil\,\&\,gas,\,ini}}(t) + (t - t_0)\, s_{\mathrm{C_2H_6}} \tag{3.5}$$

where $E_{\mathrm{CH_4,\,tot,\,opt}}(t)$ and $E_{\mathrm{C_2H_6,\,oil\,\&\,gas,\,opt}}(t)$ are optimized annual global emissions of methane and of ethane from the oil and gas industry in $\mathrm{Tg\,yr^{-1}}$. Initial annual global emissions are denoted as $E_{\mathrm{CH_4,\,tot,\,ini}}(t)$ and $E_{\mathrm{C_2H_6,\,oil\,\&\,gas,\,ini}}(t)$ with year $t \in [2007,\, 2014]$, reference year $t_0 = 2006$, and linear emission growth rates $s_{\mathrm{CH_4}}$ and $s_{\mathrm{C_2H_6}}$.

The choice of a linear emission increase in the model is motivated by the largely linear growth of fossil fuel production, which implies a linear ethane emission increase from this sector. Additionally, the positive ethane trend since 2007 can only be reproduced by a continuous emission increase, as the relatively short atmospheric lifetime of ethane prevents it from accumulating over the years. In contrast, the 2007–2014 methane increase could be modeled using a methane emission step change in 2007. This would result in a linear methane increase in the following years due to its longer lifetime. However, at least the thermogenic part of methane emissions has to exhibit a linear increase as associated to a linear ethane emission increase.

Optimized Emission Increase 2007–2014. The emission optimization procedure described above provides us with the following estimates of the increase in emissions over the 2007–2014 period required to explain observed methane and ethane trends:

(i) The total methane emission increase $\Delta E_{\mathrm{CH_4,\,tot,\,opt}}$ from 2007 to 2014 causing the observed positive methane trend.

(ii) The overall increase in oil and natural gas ethane emissions $\Delta E_{\mathrm{C_2H_6,\,oil\,\&\,gas,\,opt}}$ from 2007 to 2014 necessary to explain the ethane increase observed at Zugspitze.

The latter is associated to a methane emission increase, which can be determined using a reasonable ethane-to-methane ratio of oil and gas emissions. Finally, the contribution C of oil and natural gas emissions to the recent methane increase since 2007 can be inferred as ratio of the increase in oil and gas methane emissions to the total methane emission increase in 2007–2014:

$$C = \frac{\Delta E_{\mathrm{C_2H_6,\,oil\,\&\,gas,\,opt}} \cdot \mathrm{EMR}^{-1}}{\Delta E_{\mathrm{CH_4,\,tot,\,opt}} \cdot M_{\mathrm{C_2H_6}}/M_{\mathrm{CH_4}}} \tag{3.6}$$

Here, EMR is the assumed molar ethane-to-methane ratio for oil and gas emissions and $M_{\mathrm{C_2H_6}}/M_{\mathrm{CH_4}}$ the molar mass ratio of ethane and methane ($30\,\mathrm{g\,mol^{-1}}/16\,\mathrm{g\,mol^{-1}}$).

Oil and Gas Emission Scenarios. Three emission scenarios are considered, each characterized by a distinct ethane-to-methane ratio range of the oil and natural gas emissions:

(i) Scenario 1: attribution to a combination of oil and natural gas emissions with EMR = 7.0–16.2 % (i.e., ranging from the upper bound of natural gas EMR values to the lower bound of oil-related EMR values)

(ii) Scenario 2: complete attribution to oil-related emissions with EMR = 16.2–31.4 %

(iii) Scenario 3: complete attribution to natural gas sources with EMR = 4.4–7.0 %

With the approach presented here, oil and natural gas sources cannot be distinguished. As reliable information on the ratio of oil-related emissions to natural gas emissions is missing, a plausible EMR for combined oil and natural gas emissions has to be assumed. While scenario 1 is considered as most reasonable reference scenario, scenario 2 and 3 represent two extreme limiting cases. EMR ranges are taken from Schwietzke et al. (2014) and are originally given as mass-based methane-to-ethane ratios (MER) in units of $\mathrm{Tg\,CH_4\,(Tg\,C_2H_6)^{-1}}$. For reasons of consistency with Sect. 3.4.1, MER values are converted to molar EMR ranges with $\mathrm{EMR} = \mathrm{MER}^{-1} \times M_{\mathrm{CH_4}}/M_{\mathrm{C_2H_6}} \times 100\,\%$. The corresponding MER ranges of the presented emission scenarios amount to MER = [3.3, 7.6] in scenario 1, MER = [1.7, 3.3] in scenario 2, and MER = [7.6, 12.1] in scenario 3.

Uncertainty Analysis. Uncertainties of the estimated optimized emission changes for 2007–2014 ($\Delta E_{\mathrm{CH_4,\,tot,\,opt}}$ and $\Delta E_{\mathrm{C_2H_6,\,oil\,\&\,gas,\,opt}}$) are determined using a perturbation approach. Respective lower and upper bound estimates are inferred from separate two-box model runs with all model parameters either set to the lower or the upper bound of their uncertainty ranges (see Tables 3.2 and 3.3), in order to maximize or minimize the modeled trend. Consequently, the uncertainty range (2.5^{th}–97.5^{th} percentile) of the oil and natural gas contribution C is derived using a Monte Carlo simulation: 10^6 random samples are drawn from normally distributed EMR values and from lognormal distributions of $\Delta E_{\mathrm{C_2H_6,\,oil\,\&\,gas,\,opt}}$ and $\Delta E_{\mathrm{CH_4,\,tot,\,opt}}$ (parameter ranges are interpreted as $3 \times \mathrm{SD}$ intervals of the distributions).

Emission Optimization Results. Fig. 3.8 illustrates the results obtained by two-box model simulations described in the previous paragraphs. Modeled methane and ethane time series are shown for high northern and southern latitudes (HNL: 30–90° N, HSL: 30–90° S) in Fig. 3.8a and Fig. 3.8b. Prior global methane and ethane emission inventories are depicted in Fig. 3.8c together with the optimized emission scenario for 2007–2014 (including optimized total methane emissions and optimized ethane emissions from oil and natural gas production).

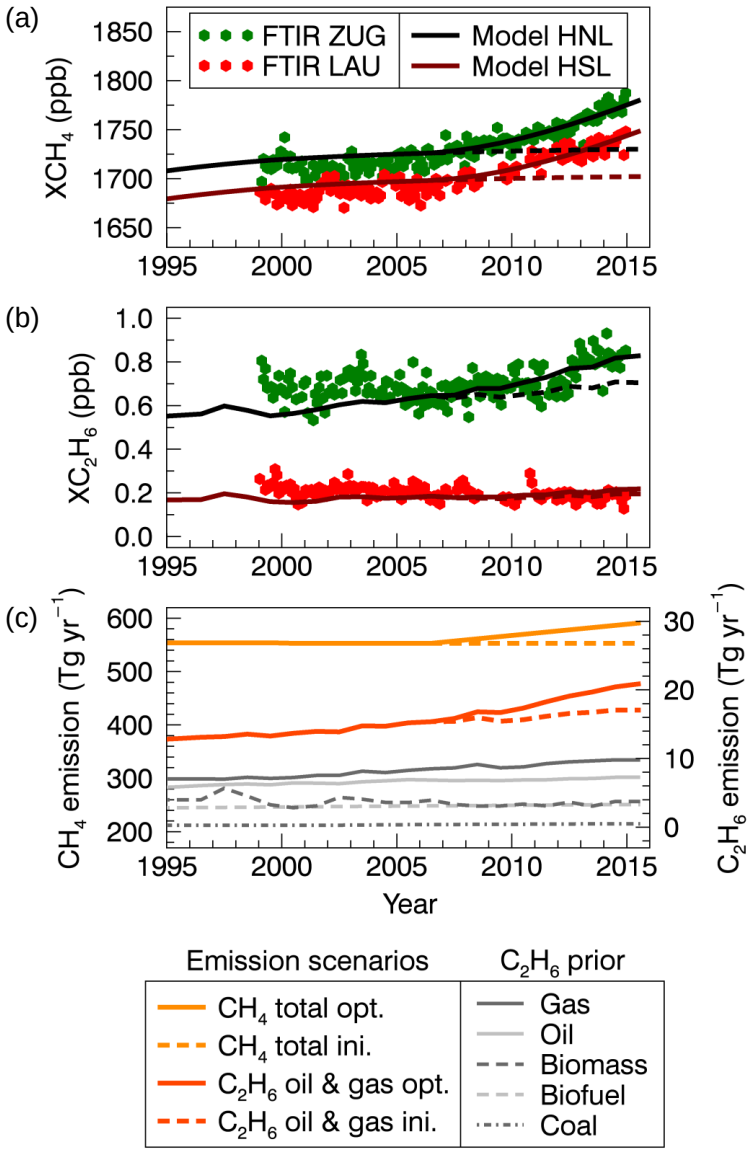

Figure 3.8: Methane and ethane two-box model: monthly mean column-averaged (a) methane and (b) ethane from Zugspitze and Lauder FTIR observations. Modeled annual means of XCH_4 and XC_2H_6 are shown for high northern and southern latitudes (HNL, HSL) after emission optimization (solid lines) and with prior emissions (dashed lines). An overall offset is applied to the modeled time series to fit the observed average for 2007–2014. (c) Emission scenario for 2007–2014: optimized global emissions of methane ("CH_4 total opt.", left y-axis) and ethane from oil and natural gas sources ("C_2H_6 oil & gas opt.", right y-axis). For comparison, the corresponding initial emission histories are displayed along with prior ethane emissions of all considered source categories (Hausmann et al., 2016).

Positive methane and ethane trends observed in the 2007–2014 period correspond to an optimized 2007–2014 increase in global methane emissions of $\Delta E_{\mathrm{CH_4,\,tot,\,opt}} = 24$–$45\,\mathrm{Tg\,yr^{-1}}$ and an optimized increase in ethane oil and gas emissions of $\Delta E_{\mathrm{C_2H_6,\,oil\,\&\,gas,\,opt}} = 1$–$11\,\mathrm{Tg\,yr^{-1}}$. Thermogenic methane emissions from oil and natural gas production significantly contribute to the renewed methane increase since 2007 for all three considered emission scenarios. The 95 % confidence interval of the oil and gas contribution C amounts to:

(i) $C = [39, 160]\,\%$ for scenario 1 (oil and gas emission combination)

(ii) $C = [18, 72]\,\%$ for scenario 2 (only oil-related emissions)

(iii) $C = [73, 280]\,\%$ for scenario 3 (pure natural gas sources)

The most reasonable case is represented by assumptions of reference scenario 1. Scenarios 2 and 3 are only considered as limiting cases and should not be perceived as realistic settings. The lower boundary of these confidence intervals provides an estimate for the minimum contribution of oil and natural gas emission to the renewed methane increase. The upper boundaries exceeding 100 % are physically not meaningful and not taken into further consideration.

Methane Emission Increase (2007–2014). The total methane emission increase over the 2007–2014 period estimated from two-box model simulations ($\Delta E_{\mathrm{CH_4,\,tot,\,opt}} = 24$–$45\,\mathrm{Tg\,yr^{-1}}$) agrees well with estimates of previous studies. Bergamaschi et al. (2013) report a methane emission increase by 16–20 $\mathrm{Tg\,yr^{-1}}$ for 2007–2010 compared to 2003–2005. Kirschke et al. (2013) find a methane emission increase of 17–22 $\mathrm{Tg\,yr^{-1}}$ from 2005 to 2010, which is probably low-biased due to few observations at the end of the 2010 5-year average. A methane emission increase of 22–18 $\mathrm{Tg\,yr^{-1}}$ between 2005 and 2009 (3-year average) is derived from emissions estimated with CarbonTracker-CH_4 (Bruhwiler et al., 2014; available at www.esrl.noaa.gov/gmd/ccgg). All of these literature estimates can be extrapolated to the period 2007–2014 assuming constant emission growth over this period. Estimates of the overall emission increase from 2007 to 2014 amount to 25–31 $\mathrm{Tg\,yr^{-1}}$, 24–31 $\mathrm{Tg\,yr^{-1}}$, and 20–56 $\mathrm{Tg\,yr^{-1}}$ as extrapolated from the estimates in Bergamaschi et al. (2013), Kirschke et al. (2013), and Bruhwiler et al. (2014), respectively. These overall 2007–2014 emission changes are defined as the difference between global methane emissions in 2014 and in 2007 assuming linear emission growth over this period. These estimates are to be distinguished from an instantaneous source–sink imbalance in a certain year derived from the annual methane growth rate in that year using an atmospheric one-box model and a mole-fraction-to-mass conversion factor (Dlugokencky et al., 1998). According to this approach a methane growth rate of about $6\,\mathrm{ppb\,yr^{-1}}$ can be translated to a source–sink imbalance of $16\,\mathrm{Tg\,yr^{-1}}$ (Dlugokencky et al., 2015a). A corresponding emission step change in 2007 implemented in the two-box model could be used to simulate the observed methane increase since 2007 (which is not the case for ethane). After such an emission step change a new steady state is approached on a timescale comparable to the atmospheric lifetime of methane.

Discussion on Oil and Gas Emission Optimization. The emission optimization approach presented in the previous paragraphs considers ethane emissions only from oil and natural gas sources, which implies to attribute additional ethane emissions (compared to

emission inventories) completely to increasing oil and natural gas sources. This approximation can be justified by several arguments compiled in following. The long-term variability of ethane is dominated by changes in its fossil fuel sources (Aydin et al., 2011). Furthermore, there is no evidence pointing to a long-term increase in biomass burning or biofuel use emissions that is sufficiently strong to explain the observed ethane trend (see discussion in Sect. 3.4.1). The biomass burning emission inventory applied in this study (GFED4s) is based on satellite-derived estimates of burned area together with biogeochemical modeling (van der Werf et al., 2010). Such top–down emission inventories can be considered to be more reliable than bottom–up inventories (Nisbet and Weiss, 2010), such as the applied fossil fuel emission inventory (Schwietzke et al., 2014). Furthermore, the inventory of Schwietzke et al. (2014) is available only until 2011 and extrapolated to 2012–2014 using global fossil fuel production data (see Sect. 3.2.2), while GFED4s data are available up to 2014. Coal mining emissions may have significantly contributed to the methane increase since 2007 (Bergamaschi et al., 2013) but play a minor role in the ethane emission increase which cannot be fully explained by coal-related emissions. The approach using ethane as constraint for thermogenic methane emissions is not fully suitable to quantify the methane emission increase from coal mining. This is due to the fact, that coal emissions exhibit very low ethane-to-methane ratios (EMR = 0.01–1.07 %; Xiao et al., 2008; Schwietzke et al., 2014) and a substantial proportion of biogenic methane emissions (EMR < 0.1 %), which have almost no associated ethane emissions. Nevertheless, the global coal production growth of 22 % since 2007 (US Energy Information Administration, 2015) is accounted for in prior ethane emissions applied for coal mining (see Sect. 3.2.2).

In this section, the observed positive ethane trend in the Northern Hemisphere is related to a linear ethane emission increase from oil and natural gas extraction. The associated oil and natural gas methane emission increase for 2007–2014 can be determined using a realistic ethane-to-methane ratio. It is shown that growing thermogenic methane emissions from oil and natural gas sources significantly contribute to the total methane emission increase since 2007. An oil and natural gas emission contribution of at least 39 % (95 % confidence level) is found for the reference emission scenario (combined oil and gas emissions) and a contribution of at least 18 % for the limiting case of pure oil emissions.

3.5 Conclusions

In this chapter, it was demonstrated that long-term observations of column-averaged ethane within the NDACC FTIR framework provide a valuable constraint on the source attribution of methane emission changes. Harmonized time series of column-averaged dry-air mole fractions of methane and ethane were presented for Zugspitze (47° N, 11° E) and Lauder (45° S, 170° E), representative of high northern and southern latitude background conditions. Long-term trend analysis revealed consistent changes of methane concentrations in both hemispheres: the period of stagnating methane growth from 1999 to 2006 is followed by a renewed methane increase since 2007 continuing through 2014. The 2007–2014 period is characterized by a growth in column-averaged methane of 6.2 [5.6, 6.9] ppb yr^{-1} at Zugspitze and 6.0 [5.3, 6.7] ppb yr^{-1} at Lauder (95 % confidence intervals). In the case of ethane, a trend reversal in 2007 followed by a significant positive trend of 2.3 [1.8, 2.8] $\times 10^{-2}$ ppb yr^{-1} since 2007 is observed in northern high latitudes at Zugspitze, in contrast to a continuing decline (-0.4 [-0.6, -0.1] $\times 10^{-2}$ ppb yr^{-1}) in southern high latitudes.

For the time period of renewed methane increase (2007–2014), evidence was derived that the underlying overall source ethane-to-methane ratio corresponds to typical emission ratios of oil and gas production sources (assuming a constant emission ratio for this time period and well-mixed hemispheres). Optimized global methane and ethane emission scenarios for 2007–2014 were derived, which are consistent with trend observations at Zugspitze and Lauder. An ethane emission increase of 1–11 $\mathrm{Tg\,yr^{-1}}$ (total increase between 2007 and 2014) from the oil and natural gas sector is necessary to reconstruct the positive ethane trend at Zugspitze. The methane emission increase associated was determined using three different assumptions of ethane-to-methane ratios: an oil and gas source mixture with EMR = 7.0–16.2 % (scenario 1), pure oil sources with EMR = 16.2–31.4 % (scenario 2), and natural gas sources with EMR = 4.4–7.0 % (scenario 3). The methane emission increase derived for 2007–2014 as constrained by the ethane emission history can then be related to the total methane emission increase of 24–45 $\mathrm{Tg\,yr^{-1}}$, which is necessary to explain the methane trend observed in 2007–2014. This analysis yields a significant contribution of emissions from oil and natural gas production to the renewed methane increase since 2007. At 95 % confidence level, the increase in these thermogenic methane emissions accounts for at least 39 % (scenario 1, assuming a mixture of oil and natural gas sources), at least 18 % (scenario 2, assuming pure oil sources), or at least 73 % (scenario 3, assuming pure gas sources) of the renewed methane increase.

For verification of these results, more sophisticated source–sink inversion are to be conducted using full 3-D chemical transport models to simulate atmospheric methane and ethane trends. Further information on the emissions causing positive methane trends can be gained from methane isotope observations, particularly in combination with ethane measurements. The findings presented indicate the direction for further source attribution studies of the renewed methane increase and provide basic knowledge for developing effective methane emission reduction strategies.

Chapter 4

Water Vapor and its Isotopes as Transport Tracer

4.1 Introduction

Water vapor is of fundamental importance in the climate system of our Earth. As dominant greenhouse gas it accounts for about 60 % of the natural greenhouse effect (Kiehl and Trenberth, 1997; Harries et al., 2008). The Earth's energy budget is closely linked to the global water cycle which effectively redistributes energy by latent heat transport (Stephens et al., 2012; Wild et al., 2013). However, relevant processes determining the interaction between atmospheric humidity, circulation, and climate are still not completely understood (e.g., cloud feedback mechanisms). A major challenge in climate modeling remains to accurately represent the response of the hydrological cycle and general circulation patterns to climate change (Bengtsson et al., 2014; Bony et al., 2015).

Large-scale circulation patterns in the northern midlatitudes are dominated by prevailing westerly winds. Extratropical cyclones and deep convective systems facilitate transport of water vapor from moisture sources to higher altitudes and latitudes. Along these major transport pathways also other trace gas signatures and pollution plumes can travel over long distances from source to receptor regions – possibly even to other continents (e.g., Stohl, 2001; Stohl et al., 2002). Transported species of predominantly natural origin include, among others, volcanic ash (e.g., Trickl et al., 2013), biomass burning aerosols (e.g., Forster et al., 2001; Wotawa et al., 2001; Damoah et al., 2004; Fromm et al., 2010; Trickl et al., 2015), pollen (e.g., Jochner et al., 2015), mineral dust (e.g., Husar, 2004; Papayannis et al., 2008; Trickl et al., 2011; Israelevich et al., 2012), and stratospheric ozone (e.g., Beekmann et al., 1997; Škerlak et al., 2014). Relevant anthropogenic tracers are, e.g., aerosols, carbon monoxide, ozone, and its precursors. Such transport events impact climate, air quality, and human health in the receptor regions and are highly relevant for agreements on emission regularizations (Holloway et al., 2003; TF-HTAP, 2010).

Research on long-range transport to Central Europe has a long history at high-altitude observatories, such as Zugspitze or Jungfraujoch, which offer a unique opportunity to monitor free tropospheric conditions. Transport studies using lidar (light detection and ranging) and in situ measurements combined with transport modeling identified three main

long-range transport patterns to Central Europe. First, intercontinental transport from North America effectively carries anthropogenic emissions within 3–10 days to the European middle troposphere after lifting by warm conveyor belts (Stohl and Trickl, 1999; Trickl et al., 2003). Second, intercontinental transport from Northern Africa imports Saharan mineral dust into Europe in 5–15 events per year (Papayannis et al., 2008; Flentje et al., 2015). Third, stratosphere–troposphere transport facilitates intrusions of dry, ozone-rich air into the Central European troposphere after typically descending 3–15 days from the lowermost stratosphere (Stohl et al., 2003; Trickl et al., 2010, 2014, 2015, 2016).

Valuable information on tropospheric moisture pathways (and associated transport of other tracers) is provided by measurements of water vapor and its isotopes (Strong et al., 2007; González et al., 2016; Schneider et al., 2016). The isotopic composition of atmospheric water vapor is modified during phase transitions (evaporation, condensation, and sublimation) due to fractionation processes caused by isotopic mass differences (Dansgaard, 1964). The main source of water vapor in the atmosphere is evaporation from the ocean surface. Subsequently, air masses are transported to regions of lower temperatures, where condensation or sublimation occurs together with associated rainout. These processes cause the air mass to become increasingly dehydrated and depleted in the heavier isotope HDO. Resulting large-scale isotope effects (e.g., Worden et al., 2007; Christner, 2015) include increasing HDO depletion with higher latitudes (latitude effect), with higher altitudes (altitude effect), and with increasing distance from oceans (continental effect). The relative HDO content of water vapor is typically expressed in terms of δD which is defined as relative deviation of the HDO-H_2O ratio from a standard reference, i.e.,

$$\delta\mathrm{D} = \left(\frac{\mathrm{VMR_{HDO}}/\mathrm{VMR_{H_2O}}}{\mathrm{R_{SMOW}}} - 1\right) \times 1000\,‰ \tag{4.1}$$

where $\mathrm{VMR_{HDO}}$ and $\mathrm{VMR_{H_2O}}$ are volume mixing ratios of HDO and H_2O and $\mathrm{R_{SMOW}} = 3.1152 \times 10^{-4}$ is the HDO-H_2O ratio of Standard Mean Ocean Water (Craig, 1961). In the following, also columnar water vapor and δD values are applied: integrated water vapor (IWV) is the H_2O total column multiplied by $3.345 \times 10^{-21}\,\mathrm{mm\,(molecules\,cm^{-2})^{-1}}$ and column-based δD ($\delta\mathrm{D_{col}}$) is calculated using the ratio of total columns in Eq. (4.1).

So far, research on long-range transport to Central Europe has mainly been based on investigations or field campaigns of special transport events combining observations of conventional tracers (such as ozone, aerosols, and humidity) at few sites. This classical approach is not sufficient to fully capture complex transport mechanisms within the global hydrological cycle. With the advance of water vapor isotope remote sensing, a new promising transport tracer has become available (i.e., consistent H_2O-δD data). Only recently, tropospheric water vapor isotope data sets were derived from satellite remote sensing measurements (Worden et al., 2006; Schneider and Hase, 2011; Lacour et al., 2012; Boesch et al., 2013; Frankenberg et al., 2013; Sutanto et al., 2015). Additionally, within the project MUSICA, retrieval methods were developed to infer tropospheric H_2O-δD profiles from ground-based mid-infrared FTIR measurements (Barthlott et al., 2017; Schneider et al., 2016) operated within NDACC. Retrieving H_2O-δD time series from globally distributed operational NDACC sites will provide us with a vast transport tracer data set that has to be exploited to gain a more comprehensive picture of atmospheric moisture transport. As these transport processes can be associated with the dispersion of natural or anthropogenic emissions, this is of particular interest for emission regularization policies and human health issues (e.g., air pollution, pollen distribution). Additionally, analysis of H_2O-δD data will

yield further insight into the coupling of the hydrological cycle with general circulation patterns, urgently needed to improve our understanding of climate change.

The goal of the investigations presented in this chapter is to evaluate new possibilities in transport research, which are provided by long-term consistent H_2O-δD observations. The results were published in Hausmann et al. (2017). The latest H_2O-δD retrieval version (see Sect. 2.2.2) is applied to an exemplary midlatitude NDACC FTIR site (i.e., Mt. Zugspitze). The resulting update of the Zugspitze water vapor time series (Sussmann et al., 2009) including isotopic information is presented in Section 4.2. Based on this data set, moisture pathways to the Central European free troposphere are identified using backward trajectories and δD outlier analysis (Sect. 4.3.1). The main task is to identify distinct H_2O-δD signatures for long-range transport patterns (Sect. 4.3.2) and combine the results with conventional transport tracers from lidar and in situ measurements (Sect. 4.3.3). Finally, a summary is given in Section 4.4 along with the conclusions drawn.

4.2 Long-Term H_2O-δD Time Series at Zugspitze

A decadal time series of water vapor and its isotopes (2005–2015) is derived from ground-based solar absorption FTIR measurements obtained at Mt. Zugspitze (47.42° N, 10.98° E; 2964 m a.s.l.). This high-altitude observatory is mostly located above the moist boundary layer or just below its upper edge (Carnuth et al., 2002). Consequently, sampled air masses are representative of free tropospheric background conditions over Central Europe. Details on the Zugspitze FTIR instrument are given in Section 2.2.1. Observed high-resolution mid-infrared FTIR spectra provide information on a large number of trace gases, including water vapor and its isotopes (Sussmann et al., 2009; Schneider et al., 2013). However, the retrieval of water vapor isotopes from such spectra is very demanding due to the high variability of atmospheric water vapor compared with relatively small variations in δD, which result from strong correlations between HDO and H_2O abundances. Schneider et al. (2015) developed a retrieval strategy for consistent H_2O-δD pairs (see details in Sect. 2.2.2), which is applied to Zugspitze FTIR observations in this section.

To characterize the resulting Zugspitze H_2O-δD data set, typical averaging kernels are depicted in Fig. 4.1 for the humidity-proxy state, i.e., $1/3 \times (\ln[H_2O] + \ln[HDO] + \ln[H_2{}^{18}O])$. An exemplary measurement on 29 October 2009 is chosen, which represents the mean state of the Zugspitze time series (type 2 data: IWV = 3.8 mm, DOFS = 1.6). Furthermore, the vertical sensitivity is analyzed, which is defined as sum over the row elements of the averaging kernel matrix (see Eq. (2.22)). Retrieved profiles are perceived to be sensitive in an altitude region with vertical sensitivity values larger than 0.75. For Zugspitze observations, the type 1 retrieval product provides optimally estimated H_2O profiles with an average DOFS of 2.8 (standard deviation SD = 0.2) and vertical sensitivity up to 12 km as shown in Fig. 4.1a. In the following, only the type 2 product is used, which provides consistent H_2O-δD profiles with an average DOFS of 1.6 (SD = 0.2) for Zugspitze (Fig. 4.1b). In this case, vertical sensitivity reaches up to 9 km (SD = 1 km) altitude and peaks around 5 km (SD = 0.5 km) altitude. The vertical resolution amounts to 2–3 km in the lower troposphere and 4–5 km in the middle-upper troposphere, as derived from the full width at half-maximum of averaging kernels. Error estimation for type 2 data yields a precision below 2 % for IWV and below 30 ‰ for column-based δD (Schneider et al., 2012).

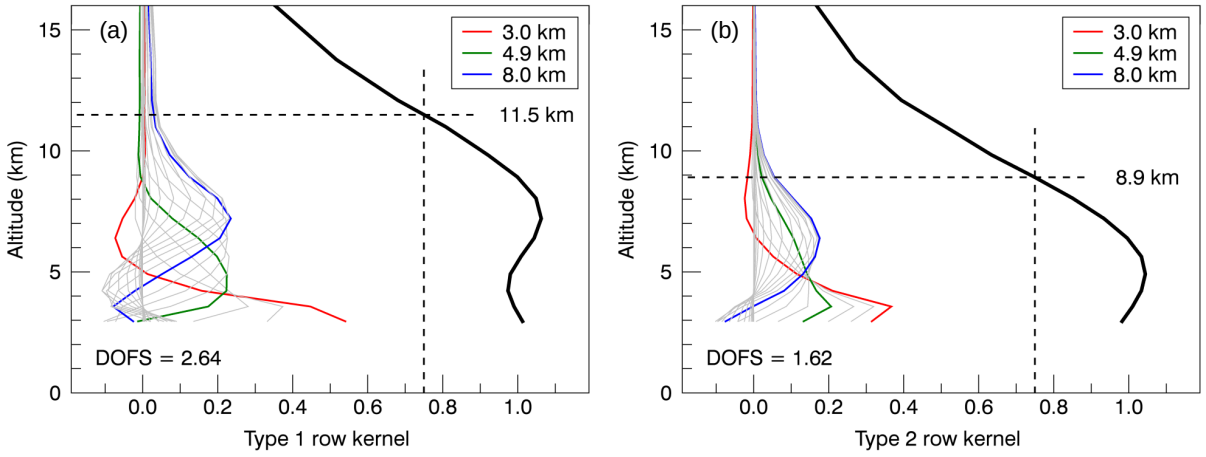

Figure 4.1: Averaging kernel rows of an exemplary H_2O measurement at Mt. Zugspitze (29 October 2009, 13:21 UTC) for two retrieval products: (a) optimally estimated humidity state (type 1) and (b) consistent H_2O-δD state (type 2). Thick black lines depict vertical column sensitivities (Hausmann et al., 2017).

Retrieval quality selection is implemented by means of a threshold in the root-mean-square residuals of the spectral fit (RMS), which is chosen to eliminate 5 % of all spectra with the highest RMS (see Sussmann et al., 2009). The full Zugspitze time series yields a mean normalized RMS of 0.26 %. Additionally, the sum of DOFS for all retrieved isotopes (H_2O, HDO, and $H_2{}^{18}O$) is required to exceed a value of 4.0. To compute daily means, only days with more than one measurement are considered. Seasonal cycles are determined by fitting an intraannual model (third-order Fourier series) to the time series, which is subtracted from the original data set for the purpose of deseasonalization. Linear trend estimates are derived as in Sect. 3.2, i.e., by fitting a linear trend model to the deseasonalized time series and determining uncertainties (95 % confidence intervals) with bootstrap resampling of the residuals (Gardiner et al., 2008).

Time series of daily mean integrated water vapor and column-based δD above Mt. Zugspitze are presented in Fig. 4.2 for the period 2005–2015. This long-term data set comprises 1154 daily means derived from 10184 quality selected FTIR spectra with, on average, nine spectra per measurement day and 105 measurement days per year. The multiannual mean of the deseasonalized IWV time series amounts to 4.4 ± 0.1 mm (mean $\pm$ 2 SE), which reflects very dry conditions at the high-altitude Zugspitze site. The multiannual mean of deseasonalized column-based δD amounts to -311.3 ± 3.8 ‰. This relatively low value corresponds to strong HDO depletion at high altitudes according to the altitude effect. The multiannual mean δD_{col} value at Zugspitze is slightly less depleted than observations at nearby, but even higher Jungfraujoch station (46.5° N, 8.0° E; 3580 m a.s.l.), which exhibits a multiannual mean δD_{col} of -330 ‰ (Schneider et al., 2012).

The presented daily mean IWV and δD_{col} time series provide the basis to derive long-term trends for the period 2005–2015, which are briefly discussed in this paragraph. For column-based δD, a statistically insignificant trend of 0.8 [−3.1, 4.7] % per decade is inferred (relative to the overall δD_{col} mean). The IWV time series yields a weakly positive but also insignificant trend of 2.4 [−5.8, 10.6] % per decade (relative to the overall IWV mean). Over the same time period (2005–2015), temperature increases significantly (1.3 [0.5, 2.1] K per decade) at Mt. Zugspitze. This positive temperature trend is derived from daily mean

temperature data based on hourly in situ measurements, which are coincident with FTIR data (coincidence interval of ± 30 min). Assuming constant relative humidity (RH) and following the Clausius-Clapeyron equation (Schneider et al., 2010), the observed temperature increase translates to a positive IWV trend of 9.2 [3.7, 14.7] % per decade. This calculated IWV trend agrees with the observed IWV trend if considering uncertainties. The assumption of constant RH is valid on large spatial scales, while over specific land regions RH might have slightly decreased (Hartmann et al., 2013), which would explain the relatively large calculated IWV trend compared to observations.

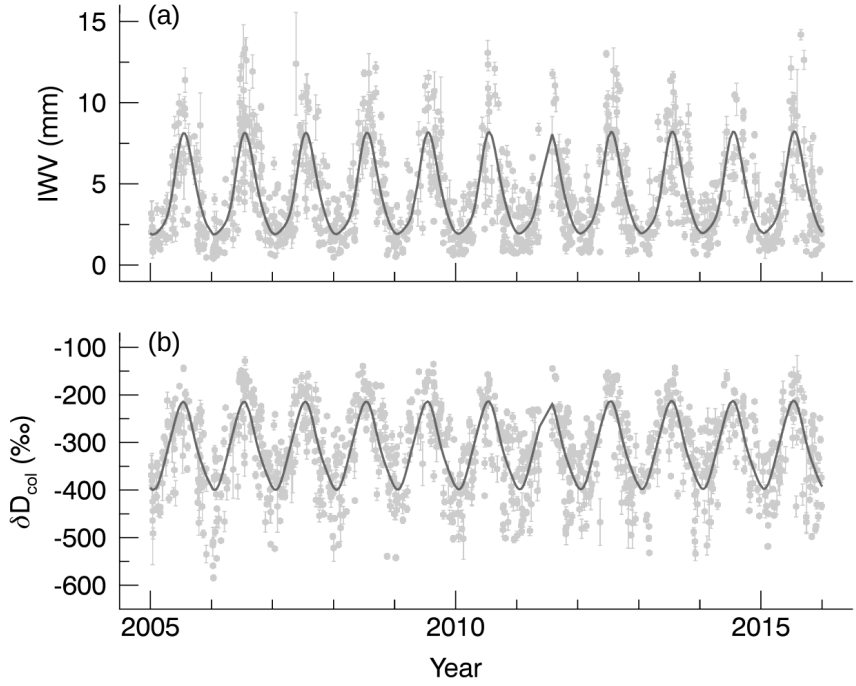

Figure 4.2: Daily mean time series of (a) integrated water vapor and (b) column-based δD retrieved from Zugspitze FTIR measurements. Error bars indicate uncertainties of daily means (± 2 SE) and grey lines show corresponding seasonal cycles determined by fitting a third-order Fourier series (Hausmann et al., 2017).

Strong seasonal cycles of free tropospheric water vapor and δD are observed above Zugspitze. Fig. 4.3 shows multiannual monthly means for an altitude of 5 km a.s.l., where the vertical sensitivity of the H_2O-δD product exhibits its maximum (see Fig. 4.1b). These data are representative for an altitude region of 3–7 km (full width at half-maximum of the averaging kernel). The seasonal cycle exhibits an amplitude of 140 % for H_2O and 50 % for δD, which is determined as difference between maximum and minimum monthly means relative to the overall mean. Both seasonal cycles exhibit a maximum in summer (July) and a minimum in winter (January). The δD maximum results from ascending motions being more frequent in summer, which are associated with transport of less HDO depleted air masses from lower altitudes and latitudes (Risi et al., 2012). Stronger HDO depletion in winter (δD minimum) is caused by a stronger continental temperature gradient in winter and associated stronger dehydration during air mass transport from the Atlantic Ocean. Additionally, transport from Eastern Europe occurs more frequently during anticyclonic conditions in winter importing strongly depleted continental air masses (Christner, 2015). Monthly frequency distributions of single H_2O measurements are generally right-skewed

and variability is larger in summer (June–August) than in winter. This might be explained by extreme moistening events due to more frequent convection and mixing with boundary layer air in summer. Monthly frequency distributions of free tropospheric δD measurements are moderately left-skewed, which points to episodic influence by strongly HDO depleted air masses (e.g., originating in the upper troposphere or lower stratosphere).

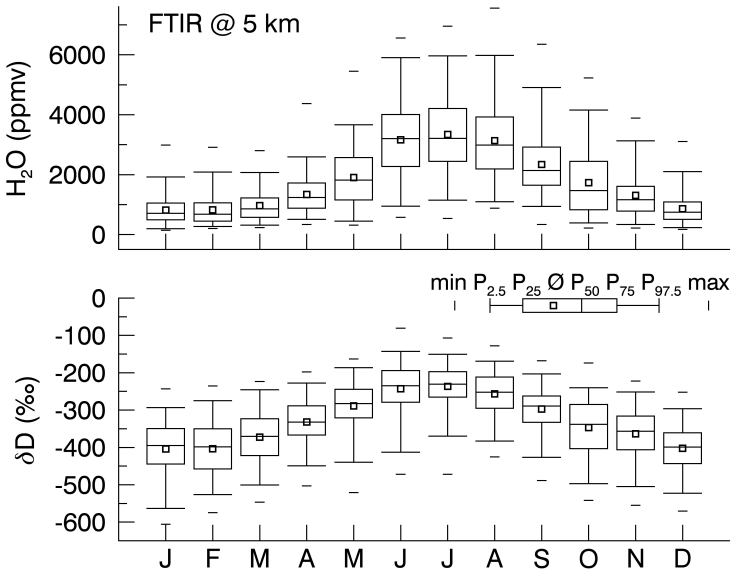

Figure 4.3: Seasonal cycles of free tropospheric water vapor and δD above Mt. Zugspitze (5 km a.s.l.): multiannual monthly means derived from 2005–2015 FTIR data and monthly frequency distributions with percentiles P as specified in the legend (Hausmann et al., 2017).

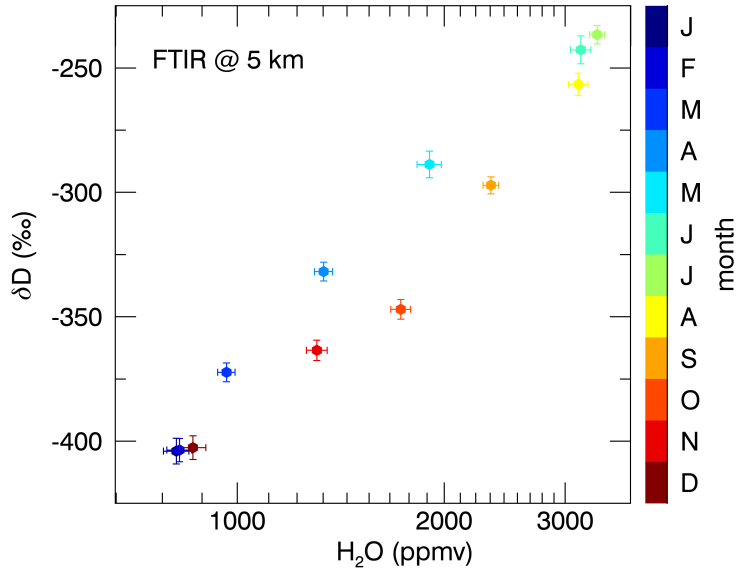

Figure 4.4: H_2O-δD distribution plot of multiannual monthly means ($\pm$ 2 SE) as presented in Fig. 4.3 for the free troposphere (5 km a.s.l.) above Mt. Zugspitze (Hausmann et al., 2017).

Visualizing these multiannual monthly means as H_2O-δD distribution plot (Fig. 4.4) reveals significant changes in the isotopic composition of atmospheric water vapor over the course of a year. Atmospheric water vapor is clearly less HDO depleted in spring than in autumn.

This is mainly caused by seasonal variations in sea surface temperature of the Atlantic Ocean (i.e., the major moisture source) as derived from Rayleigh model simulations (see Fig. 4.6). An additional contribution is possibly due to increased mixing in spring compared to autumn. These seasonal variations in the water vapor isotopic composition above Zugspitze imply that δD observations provide information complementary to the H_2O data (e.g., Risi et al., 2012; Schneider et al., 2012).

In this section, a decadal time series of consistent water vapor and δD observations was derived from FTIR measurements at Mt. Zugspitze, which is representative of Central European background conditions. These observations are used as a tracer of atmospheric transport processes to study its behavior in relation to different transport pathways to the Central Europe free troposphere.

4.3 Transport Patterns to Central Europe

4.3.1 Moisture Pathways Related to δD Outliers

To explore the potential of water vapor isotopes as a proxy for transport processes, moisture transport pathways are identified for cases of extreme water vapor isotopic composition. The Zugspitze H_2O-δD data product contains predominantly information on free tropospheric moisture pathways reaching Central Europe in the altitude region around 5 km a.s.l. (see Fig. 1b). With the help of backward trajectory analysis, these transport pathways are determined for outliers in column-based δD derived from the frequency distribution of the deseasonalized daily mean time series at Mt. Zugspitze (2005–2015). High outliers are defined as daily mean values larger than the 95$^{\text{th}}$ percentile of the frequency distribution ($\delta D_{col} > -219\,‰$) and low outliers are days with δD_{col} below the 5$^{\text{th}}$ percentile ($\delta D_{col} < -430\,‰$). This definition yields 56 (57) days of high (low) δD_{col} outliers from a total of 1154 measurement days.

For all Zugspitze FTIR measurement times in 2005–2015, the Air Resources Laboratory's HYbrid Single-Particle Lagrangian Integrated Trajectory model (HYSPLIT; available at http://ready.arl.noaa.gov; Stein et al., 2015) is applied to calculate 120-hour backward trajectories arriving in 5 km altitude at Mt. Zugspitze. Meteorological data are taken from the NCEP reanalysis (global 2.5° grid) and model vertical velocity is applied. Resulting backward trajectories are shown in Fig. 4.5. Stohl (1998) estimated trajectory uncertainty to 10–20 % of the travel distance. This estimate is fulfilled in the free troposphere according to our experience. As initial point of the trajectories the point of last condensation (LC) is chosen, which is defined as region along the trajectory where the relative humidity exceeds 80 % for a period of at least three hours (see González et al., 2016). As water vapor mixing ratios and isotopic composition are conserved in absence of sources and sinks (Galewsky et al., 2005; Noone, 2012), conditions at the LC point determine H_2O-δD observations along the trajectory if mixing during transport is negligible. If no LC point is found (i.e., no condensation occurred), full 120-hour trajectories are depicted in Fig. 4.5.

According to the location of Mt. Zugspitze in the zone of prevailing westerlies and in agreement with results from long-term ozone lidar measurements at nearby Garmisch site (see Sect. 4.3.3), the majority of trajectories point to moisture sources over the Atlantic

Ocean spreading across a wide latitude range (from subtropics to polar regions). Several trajectories originate over the North American continent or even the Pacific region. Fewer trajectories arrive from Eastern Europe or Northern Africa.

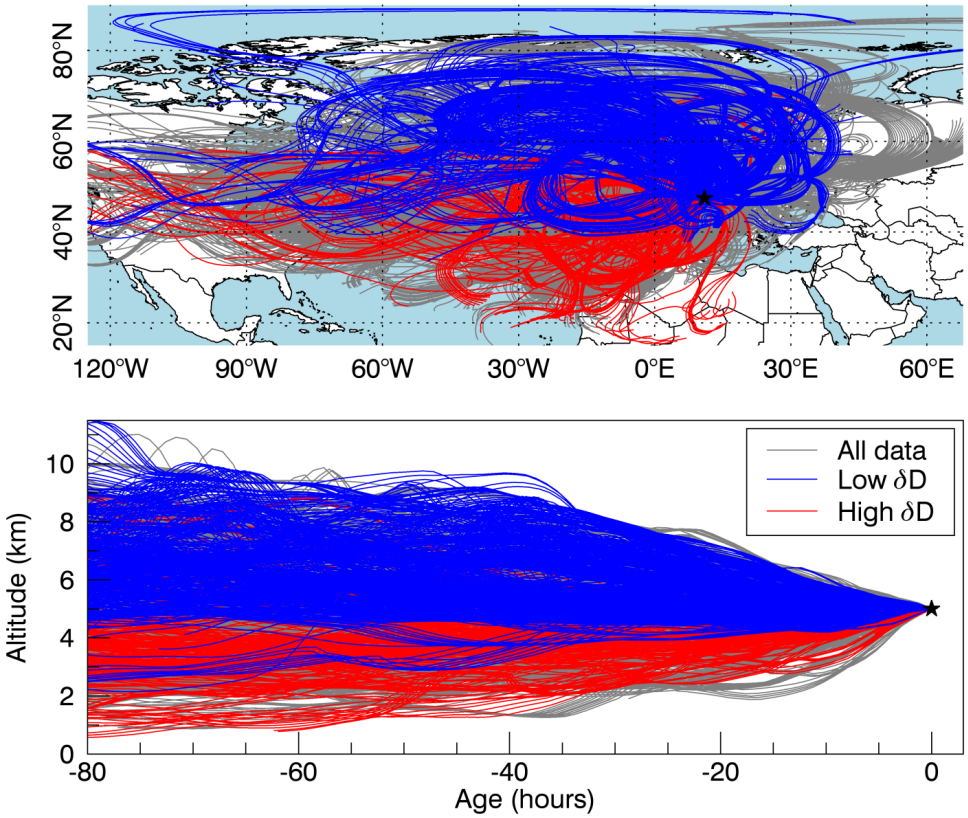

Figure 4.5: Backward trajectories of air masses arriving at Mt. Zugspitze (marked as black star) in 5 km a.s.l. altitude: map projection (upper panel) and vertical cross section (lower panel) of trajectories for all FTIR measurement times in 2005–2015 (grey lines) and for days identified as δD_{col} outliers (blue and red lines) (Hausmann et al., 2017).

Table 4.1: Air mass origin and conditions at last condensation point for trajectories on δD outlier days (only if LC is found) given as mean values with uncertainties of two standard errors (SE) and corresponding minimum and maximum value ranges (Min, Max).

	High δD_{col} ($> 95^{th}$ perc.)		Low δD_{col} ($< 5^{th}$ perc.)	
	Mean ($\pm$ 2 SE)	Min, Max	Mean ($\pm$ 2 SE)	Min, Max
Latitude (°N)	46 [45, 47]	30, 55	62 [61, 63]	34, 75
Altitude (km a.s.l.)	4.6 [4.4, 4.9]	0.4, 8.1	6.5 [6.4, 6.6]	3.3, 8.7
Pressure (hPa)	579 [560, 599]	333, 963	438 [432, 445]	317, 678
Temperature (K)	260 [259, 262]	226, 289	242 [241, 243]	224, 274
VMR_{H_2O} (10^3 ppmv)	4.1 [3.7, 4.5]	0.3, 15.6	1.2 [1.1, 1.3]	0.2, 8.5

Figure 4.5 reveals clearly different transport patterns for outliers in column-based δD observed at Zugspitze: For extraordinarily low δD_{col}, air masses mostly descend from high latitudes and altitudes, which is often related to cold advection at the rear side of an upper level trough. In contrast, on days with very high δD_{col}, air masses predominately arrive from lower latitudes ascending from lower altitudes, often in connection with warm advection at the front side of an upper level trough. Table 4.1 gives an overview of conditions at the last condensation points for trajectories related to high and low δD_{col} outliers (only if an LC point is found along the trajectory). This analysis shows that air masses originate from significantly higher latitudes (about 60° N) and altitudes (about 6.5 km) on low δD outlier days than on high δD days. Last condensation occurred at significantly lower temperatures and under dryer conditions for low δD days compared to high δD days. Consequently, mostly dry air masses are transported to Zugspitze in connection with low δD.

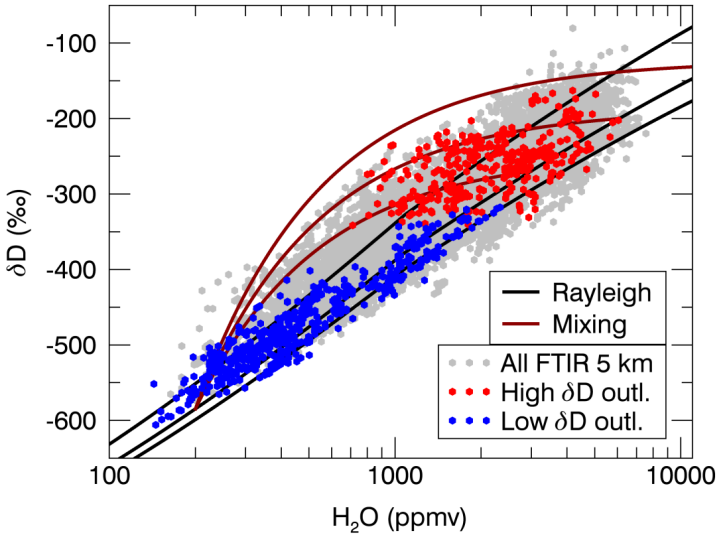

Figure 4.6: H_2O-δD distribution of free tropospheric measurements above Zugspitze (5 km a.s.l.) for all 2005–2015 data and for high and low δD outliers as determined from the deseasonalized column-based δD time series. Simulated Rayleigh and mixing processes are shown for comparison (Hausmann et al., 2017).

A first order interpretation of the H_2O-δD data pairs can be obtained by their comparison to theoretical Rayleigh and mixing lines (Wiegele et al., 2014; Schneider et al., 2015; González et al., 2016). Such a comparison is illustrated in Fig. 4.6, which shows Zugspitze H_2O-δD data at 5 km altitude along with simulated Rayleigh and mixing processes. An idealized Rayleigh process simulates the gradual dehydration of an air parcel during adiabatic cooling with immediate removal of the condensate. During this process, the remaining water vapor becomes more and more depleted in HDO. Rayleigh dehydration processes (black lines in Fig. 4.6) are simulated using a mean midlatitude profile of pressure and temperature (Christner, 2015, Table 13) and initial evaporation conditions which are characteristic for midlatitude oceanic or continental moisture sources (T = 15 ° C, RH = 80 %, and δD values of −60 ‰, −130 ‰, and −160 ‰). Furthermore, mixing processes are simulated (dark red lines in Fig. 4.6) for moist lower-middle tropospheric air masses with dry, HDO depleted upper tropospheric air (VMR_{H_2O} = 200 ppmv, δD = −585 ‰). The δD value of the mixture is mainly determined by the δD value of the mixing partner with higher water vapor content (Noone et al., 2011). Three moist mixing partners are considered here: (i) boundary layer air

with $VMR_{H_2O} = 13500\,\text{ppmv}$ and $\delta D = -130\,‰$, (ii) moderately dehydrated and depleted air with $VMR_{H_2O} = 6100\,\text{ppmv}$ and $\delta D = -200\,‰$, and (iii) even more dehydrated air with $VMR_{H_2O} = 3000\,\text{ppmv}$ and $\delta D = -270\,‰$. Comparing the simulations described above with H_2O-δD pairs observed at Zugspitze (see Fig. 4.6) reveals underlying transport regimes for designated δD_{col} outlier days: measurements on low δD days group along Rayleigh curves, while data on high δD days preferentially group along the simulated mixing lines. It is tentatively concluded that the first group (low δD_{col}) experienced slow ascent from mostly midlatitude moisture sources with associated gradual dehydration by condensation and rainout, followed by subsidence to the middle troposphere above Zugspitze with only minor mixing with moist, less depleted air masses. In contrast, the second group (high δD_{col}) reveals ascending air masses from lower latitudes and altitudes influenced by mixing with drier middle-upper tropospheric air masses.

The presented analysis of δD outliers and backward trajectories demonstrates the valuable potential of water vapor isotope observations for investigating moisture transport pathways. As along these pathways also many other atmospheric species can be transported, H_2O-δD data might also serve as useful tracer in long-range transport research.

4.3.2 H_2O-δD Signatures of Long-Range Transport Events

In the previous section, moisture transport pathways to the Central European free troposphere were identified for days with extraordinarily high or low δD observations at Mt. Zugspitze. Going a step further, it is examined to what extent H_2O-δD observations provide information also on long-range transport events of various other atmospheric tracers. In the following, H_2O-δD signatures are analyzed for three FTIR measurement categories, each of which is influenced by a distinct long-range transport pattern to the Central European free troposphere: (i) intercontinental transport from North America (TUS), (ii) intercontinental transport from Northern Africa (TNA), and (iii) stratospheric air intrusions (STI). Zugspitze FTIR measurements are assigned to these long-range transport categories by classification of respective backward trajectories (see Sect. 4.3.1) using the criteria summarized in Table 4.2 and described in more detail in the following paragraphs.

Intercontinental Transport from North America (TUS). The first transport pattern considered is intercontinental transport from North America, which may effectively carry anthropogenic pollution plumes (e.g., ozone or aerosols) to Central Europe within typically 3–10 days (Stohl and Trickl, 1999; Trickl et al., 2003; Huntrieser et al., 2005). Consequently, North American emissions strongly contribute to the European total column tracer mass (i.e., 43 % for a tracer with 10 days lifetime; Stohl et al., 2002). The typical pathway of polluted boundary layer air from North America is uplift in a warm conveyor belt (WCB, i.e., an ascending air stream ahead of a surface cold front in an extratropical cyclone) and subsequent transport by strong westerly flows in the middle-upper troposphere. The North American tracer enters Europe typically in altitudes of 5–8 km and at high latitudes ($> 60°$ N). Here, the circulation frequently turns anticyclonic and tracers eventually reach Northern Alps (Huntrieser and Schlager, 2004). WCB climatologies reveal a major inflow region at the southeastern coast of North America (Stohl, 2001; Eckhardt et al., 2004; Madonna et al., 2014). In the following, Zugspitze backward trajectories passing this source region (25–45° N, 70–110° W, 0–2 km altitude) are assigned to the TUS category.

Intercontinental Transport from Northern Africa (TNA). The second transport category is intercontinental transport from Northern Africa to the European free troposphere. Associated transport of Saharan mineral dust influences air quality, soil fertility, radiative budget, and atmospheric oxidation capacity in the receptor region (Ravishankara, 1997). Saharan mineral dust import to Central Europe occurs 5–15 times per year and each event lasts 1–3 days (Papayannis et al., 2008; Flentje et al., 2015). In the following, Zugspitze backward trajectories passing the Saharan boundary layer region (15–30° N, 15° W–35° E, 0–2 km altitude; Engelstaedter et al., 2006) are assigned to the TNA category.

Extratropical Stratospheric Intrusions (STI). The third transport class accounts for extratropical stratospheric intrusions, which occur mainly in synoptic-scale processes such as tropopause folds and cutoff lows near the polar or subtropical jet stream (Stohl et al., 2003). Filaments of ozone-rich stratospheric air descend from the lowermost stratosphere and proceed to the Central European free troposphere via several pathways (Trickl et al., 2010; Škerlak et al., 2014). Mixing with tropospheric air might exhibit relatively long time scales and little modification is reported even after several days of transport (Trickl et al., 2014). In the following, Zugspitze backward trajectories originating above the zonal mean tropopause (TP) taken from ECMWF data (Eckhardt et al., 2004) at latitudes above 20° N are assigned to the STI category (required minimum residence time of five hours above TP, which is penetrated at least once by more than 1 km). This TP definition is chosen, as potential vorticity for a dynamical TP definition is not provided within HYSPLIT.

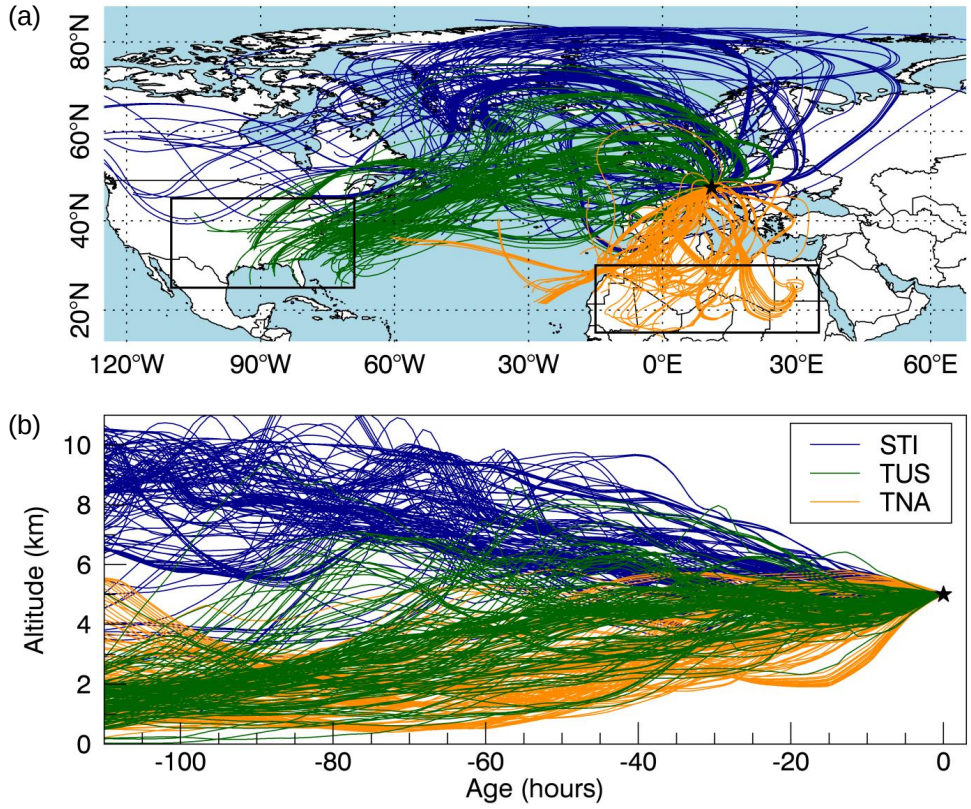

Figure 4.7: Categorization of backward trajectories for long-range transport events: (a) map projection and (b) vertical cross section for stratospheric intrusions (STI), transport from North America (TUS), and from Northern Africa (TNA). Black boxes indicate source regions used to classify TUS and TNA (see Table 4.2), black star marks Mt. Zugspitze (Hausmann et al., 2017).

H_2O-δD Signatures of Transport Events. These long-range transport categories (TUS, TNA, STI) are expected to have characteristic imprints on H_2O-δD pairs observed at Mt. Zugspitze. Stratospheric intrusions originate in the lowest few kilometers of the stratosphere (Trickl et al., 2014, 2016), where moisture content is extremely low and the mean δD profile exhibits a minimum before increasing above due to growing influence of isotopically heavier water vapor from methane oxidation (Zahn et al., 2006; Steinwagner et al., 2010). Consequently, STI events potentially import relatively dry and HDO depleted air masses to the Central European troposphere. In contrast, TUS and TNA air masses originate in the moist boundary layer and may transport relatively moist and less depleted air masses to Central Europe. However, strong WCB updraft during TUS events may cause air mass dehydration and HDO depletion through rainout (Rayleigh process). Criteria for long-range transport events described above are applied to categorize Zugspitze backward trajectories as shown in Fig. 4.7. Distributions of deseasonalized VMR_{H_2O} and δD for the corresponding classes of free tropospheric Zugspitze FTIR data (5 km a.s.l.) are depicted in Fig. 4.8. Considering uncertainty of two standard errors (± 2 SE), mean VMR_{H_2O} and δD values are significantly different for all three transport classes (see Table 4.2).

Table 4.2: Backward trajectory classification for long-range transport patterns of stratospheric intrusions (STI), transport from North America (TUS), and from Northern Africa (TNA) along with the resulting distribution of deseasonalized VMR_{H_2O} and δD.

	STI	TUS	TNA
Trajectory source region:			
Latitude	> 20° N	25–45° N	15–30° N
Longitude	–	70–110° W	15° W–35° E
Altitude	> zonal mean TP	0–2 km	0–2 km
H_2O-δD signature (mean ± 2 SE):			
VMR_{H_2O} (10^3 ppmv)	1.21 [1.07, 1.34]	2.42 [2.25, 2.59]	2.78 [2.63, 2.93]
δD (‰)	−384 [−397, −372]	−315 [−326, −303]	−251 [−257, −246]

As expected, STI is associated with the driest and most HDO depleted air masses. TNA is connected to moister and less depleted air, while TUS exhibits intermediate VMR_{H_2O} and δD values. The standard deviation of VMR_{H_2O} distributions is similar for all transport classes (SD ≈ 1000 ppmv). In the case of δD distributions, TNA shows less scatter (SD = 34 ‰) compared to TUS (SD = 65 ‰) and STI (SD = 73 ‰). This indicates a quite homogeneous source region and transport regime for TNA. Larger scatter for TUS might result from variable strengths of WCB uplift causing various levels of dehydration and HDO depletion. Relatively large scatter in the δD distribution for STI events implies that also weakly depleted air masses are observed during STI events. This could have several reasons: First, stratospheric intrusions with depths ranging from few hundreds to several thousands of meters are not necessarily resolved by the relatively coarse vertical resolution of the FTIR δD product. Second, as a climatological tropopause altitude is applied to identify STI events, local and seasonal TP variations are not accounted for, i.e., also (upper) tropospheric

trajectories might be included in the STI class. Third, mixing with tropospheric air might occur during transport from the stratosphere, which however was found to be very slow in the free troposphere (Trickl et al., 2014). Fourth, δD values in the lower stratosphere might be less depleted than predicted from Rayleigh processes, which is probably caused by extratropical troposphere–stratosphere transport, e.g., by convectively lofted ice (Hanisco et al., 2007; Steinwagner et al., 2010; Randel et al., 2012). All these mechanisms would yield higher δD observations at Zugspitze than expected for STI events from the δD minimum in the lower stratosphere.

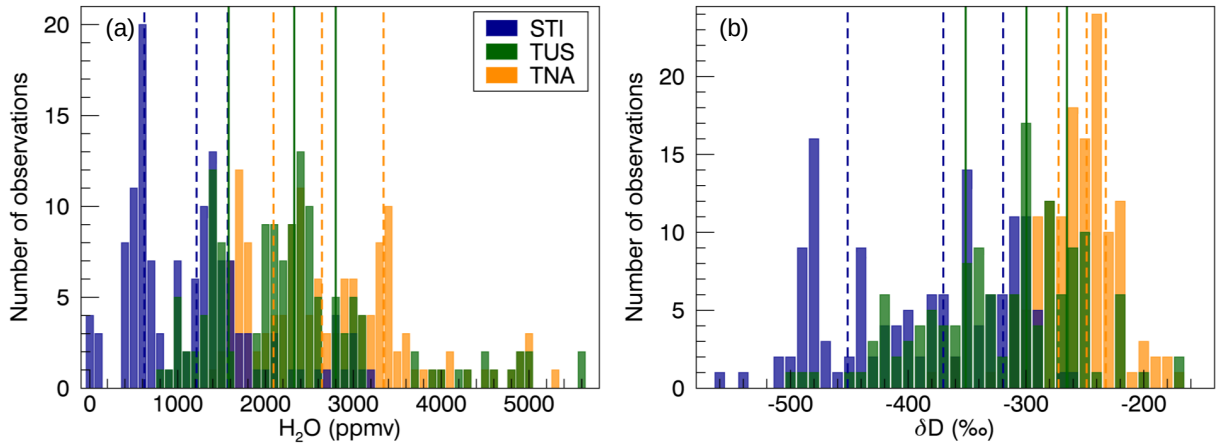

Figure 4.8: H_2O-δD signatures of long-range transport events: distribution of deseasonalized (a) VMR_{H_2O} and (b) δD in the free troposphere above Zugspitze (5 km a.s.l.) for trajectory classes shown in Fig. 4.7. Vertical lines mark corresponding 25th, 50th, and 75th percentiles of the distributions while mean and standard errors are given in Table 4.2 (Hausmann et al., 2017).

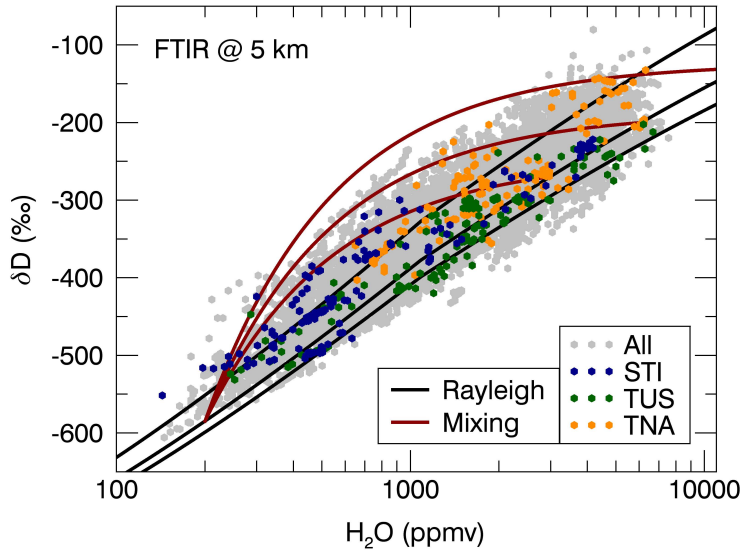

Figure 4.9: H_2O-δD distribution of free tropospheric measurements above Zugspitze (5 km a.s.l.) for all 2005–2015 data and for long-range transport categories shown in Fig. 4.7. Simulated Rayleigh and mixing processes are shown for comparison as in Fig. 4.6 (Hausmann et al., 2017).

In analogy to Fig. 4.6, H_2O-δD data pairs for these long-range transport patterns are interpreted by comparison to theoretical Rayleigh and mixing lines as depicted in Fig. 4.9.

For TNA events, it can be derived from this analysis that moist boundary layer air is imported to the free troposphere by means of dry convection without significant condensation and cloud formation (González et al., 2016; Schneider et al., 2016). Therefore, TNA air masses are less depleted in HDO (higher δD values). In case of TUS events, either dry or moist air masses can be imported to Central Europe. TUS transport is generally in line with simulated Rayleigh processes and suggests that moist TUS air masses originate over warmer surfaces while drier TUS air masses have their origin over colder regions. The STI transport category also largely agrees with Rayleigh models. In case of dry STI events, air masses seem to be partially influenced by mixing processes of dry upper tropospheric or lower stratospheric air with free tropospheric air masses.

To summarize, distinct H_2O-δD fingerprints were found in Zugspitze FTIR data for three categories of long-range transport patterns (TUS, TNA, and STI). Consequently, consistent H_2O-δD observations can serve as a valuable new transport tracer to study atmospheric transport to the Central European free troposphere, especially if combined with measurements of conventional transport tracers.

4.3.3 Lidar and In Situ Measurements of Transport Tracers

Transport categories analyzed in the previous section identify backward trajectories and FTIR measurements which are potentially influenced by long-range transport of relevant atmospheric tracers to Central Europe. However, this analysis cannot determine whether tracers other than H_2O-δD were actually transported to a significant extent along the trajectory to the receptor region. Actual tracer transport would require substantial emissions in the respective source region during air mass overpass and depends on tracer reactivity as well as on meteorological conditions during transport to Central Europe. In the following, lidar and in situ observations of conventional transport tracers (i.e., ozone, aerosols, beryllium-7, and humidity) are used to identify long-range transport events associated with tracer transport reaching the Northern Alps and to analyze the respective H_2O-δD signatures in Zugspitze FTIR measurements.

Identification of STI and TNA Events from Lidar Profiles. Ozone and aerosol lidar measurements obtained at Garmisch (47.48° N, 11.06° E, 743 m a.s.l.) close to Mt. Zugspitze offer the possibility to detect long-range tracer transport events reaching the Northern Alps. Garmisch lidar observations in the period 2013–2015 are analyzed to identify intrusions of stratospheric air (ozone-rich, dry) and mineral dust import from Northern Africa (high aerosol content). Stratospheric intrusions (STI) become apparent in lidar profiles as layers with a vertical extent of 200 meters up to several kilometers, which exhibit ozone enhancements of the order of 10 ppb or more relative to ozone concentrations observed in layers above and below. Corresponding layers of low relative humidity (RH $< 10\,\%$) are found in radiosonde profiles recorded in Munich (48.25° N, 11.55° E, 492 m a.s.l.) or in water vapor profiles from differential absorption lidar measurements at Mt. Zugspitze (Vogelmann et al., 2015). These dry, ozone-rich layers are assigned to being of stratospheric origin either by stratospheric intrusion forecasts or by HYSPLIT backward trajectories (Trickl et al., 2010). Mineral dust transport from Northern Africa (TNA) becomes apparent in lidar profiles as elevated aerosol layers which are attributed to Northern African origin by HYSPLIT trajectory analysis.

Garmisch lidar observations in the years 2013–2015 reveal 237 days influenced by STI events and 41 days of TNA events. Coincident FTIR measurements at Mt. Zugspitze are available on 136 (26) days of these STI (TNA) days, which corresponds to 47 % (9 %) of all FTIR measurement days in the 2013–2015 period. Figure 4.10 and Table 4.3 present distributions of deseasonalized daily mean IWV and δD_{col} for this compilation of FTIR measurements. TNA days with mineral dust transport exhibit significantly higher mean IWV and less HDO depletion (IWV = 5.47 [4.90, 6.05] mm, $\delta D_{col} = -266\,[-284, -247]$ ‰) compared to all FTIR data in 2013–2015 excluding TNA events (significance on 2-σ level). This result can be related to transport of less depleted air masses from lower altitudes and latitudes during TNA events. Additionally, mineral dust transport requires that no condensation (i.e., dehydration and depletion) occurred along the pathway to avoid wet deposition of aerosols. In contrast, STI events show a tendency to lower IWV and stronger HDO depletion (IWV = 4.18 [4.01, 4.34] mm, $\delta D_{col} = -322\,[-327, -316]$ ‰) compared to all FTIR data excluding STI events (significant difference on 1-σ level, see Table 4.3). The broad δD distribution for STI days is similar to results found in the previous section and can probably be explained by similar arguments as given in Sect. 4.3.2.

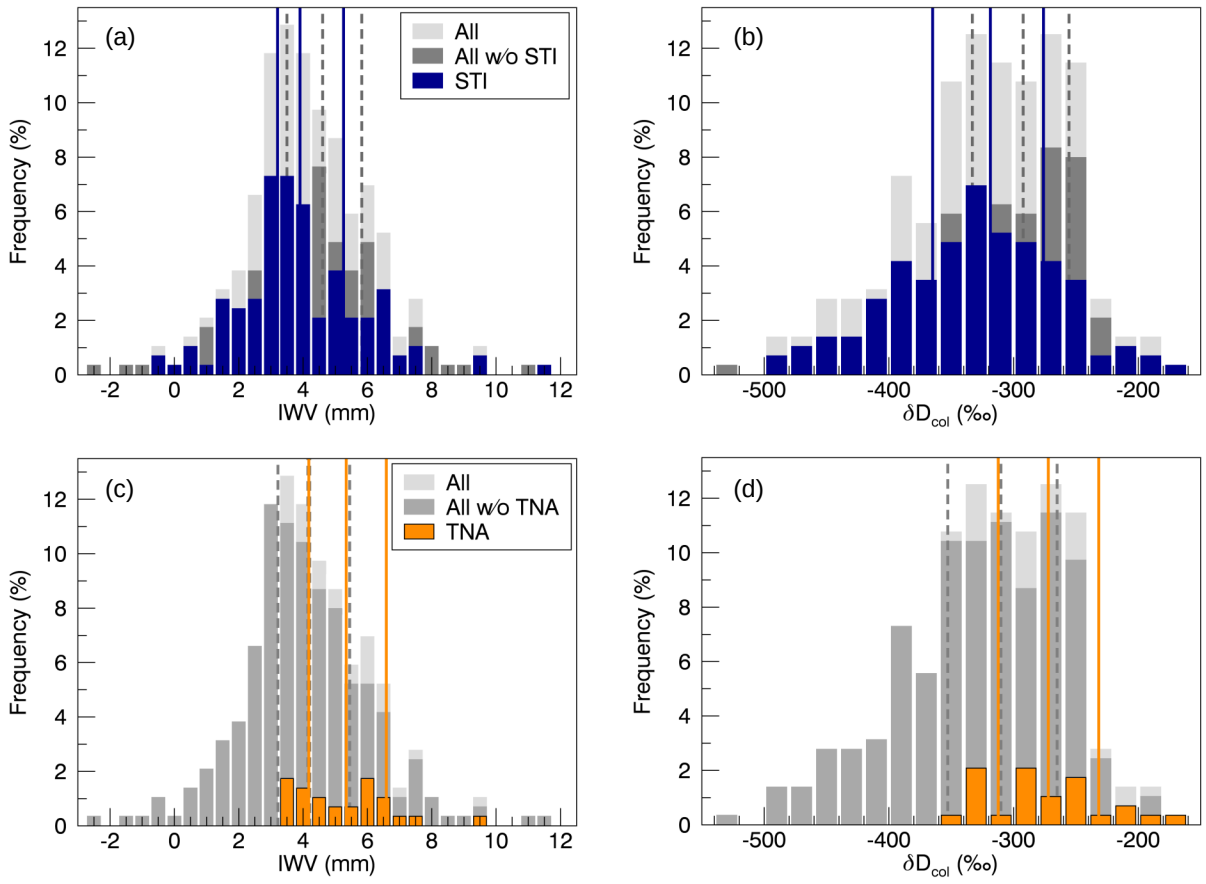

Figure 4.10: Distributions of deseasonalized daily mean IWV and column-based δD for days identified as (a, b) stratospheric intrusion events (STI) and as (c, d) dust transport events from Northern Africa (TNA). For comparison distributions for all FTIR measurements in 2013–2015 are shown as well as distributions excluding the respective transport events. Vertical lines indicate 25th, 50th, and 75th percentiles of the distributions (Hausmann et al., 2017).

Table 4.3: Mean values (± 2 SE) of deseasonalized daily mean IWV and δD_{col} at Zugspitze for STI and TNA events in 2013–2015 identified from lidar profiles and for FTIR time series excluding these events (in case of STI also mean values ± 1 SE are compiled).

	Mean (± 2 SE)		Mean (± 1 SE)	
	IWV (mm)	δD_{col} (‰)	IWV (mm)	δD_{col} (‰)
STI	4.18 [3.85, 4.51]	−322 [−333, −310]	4.18 [4.01, 4.34]	−322 [−327, −316]
All w/o STI	4.61 [4.29, 4.94]	−302 [−312, −292]	4.61 [4.45, 4.77]	−302 [−307, −297]
All	4.41 [4.18, 4.64]	−311 [−319, −304]	4.41 [4.29, 4.52]	−311 [−315, −307]
All w/o TNA	4.30 [4.05, 4.54]	−316 [−324, −308]		
TNA	5.47 [4.90, 6.05]	−266 [−284, −247]		

In Situ Observations of Deep Stratospheric Intrusions. Frequently, stratospheric intrusions penetrate deep into the troposphere, eventually reaching mountain summit observatories or even surface stations (e.g., Eisele et al., 1999; Schuepbach et al., 1999; Stohl et al., 2000; Lefohn et al., 2012; Lin et al., 2012; Itoh and Narazaki, 2016; Ott et al., 2016). In the following, deep stratospheric intrusions (DSTI) are defined as STI events reaching the summit of Mt. Zugspitze. DSTI events can be detected by in situ measurements of stratospheric tracers, such as low relative humidity and high beryllium-7 (Trickl et al., 2010). The cosmogenic radionuclide beryllium-7 (Be-7) is a good, but not unambiguous, indicator for stratospheric air, as it is produced mainly (i.e., to 67 %; Lal and Peters, 1967) in the stratosphere. Following previous studies (e.g., Trickl et al., 2010), deep stratospheric intrusions can be identified by combined tracer thresholds: flag 1 is defined as RH < 60 % and Be-7 > 85th percentile of the annual Be-7 distribution, while flag 2 is defined as RH < 60 % combined with RH < 30 % for at least one data point within six hours before and after the respective measurement. For the period 2005–2015, in situ measurements at Mt. Zugspitze provide 12-hour averages of Be-7 and hourly RH data (T. Steinkopff, pers. comm., 2016), displayed in Fig. 4.11. Deep stratospheric intrusion periods are marked as identified by flag 1. In addition, Fig. 4.11 shows coincident FTIR observations of lower tropospheric δD (deseasonalized hourly means, partial column from 3–5 km a.s.l.). From a total of 6560 hourly mean δD data in 2005–2015, 24 % are identified as DSTI events using in situ flag 1 and 38 % if using flag 2. The tendency of flag 2 to cover more intrusion cases is expected from results in Trickl et al. (2010). The distribution of lower tropospheric δD for deep stratospheric intrusion events is depicted in Fig. 4.12. The mean value of lower tropospheric δD is significantly lower for DSTI events than for the full time series without these events. It amounts to −334 [−337, −330] ‰ (mean ± 2 SE) for DSTI flag 1 and, for flag 2, it amounts to −331 [−334, −328] ‰. A mean value of −284 [−286, −282] ‰ (−274 [−276, −273] ‰) is obtained for the full time series excluding DSTI events identified with flag 1 (flag 2). For the full time series, it amounts to −296 [−298, −294] ‰. Scatter of lower tropospheric δD distributions is about 70 ‰ for both DSTI flags. Overall, both flags for the identification of deep stratospheric intrusions from in situ observations provide consistent results with respect to the distribution of lower tropospheric δD derived from coincident FTIR measurements.

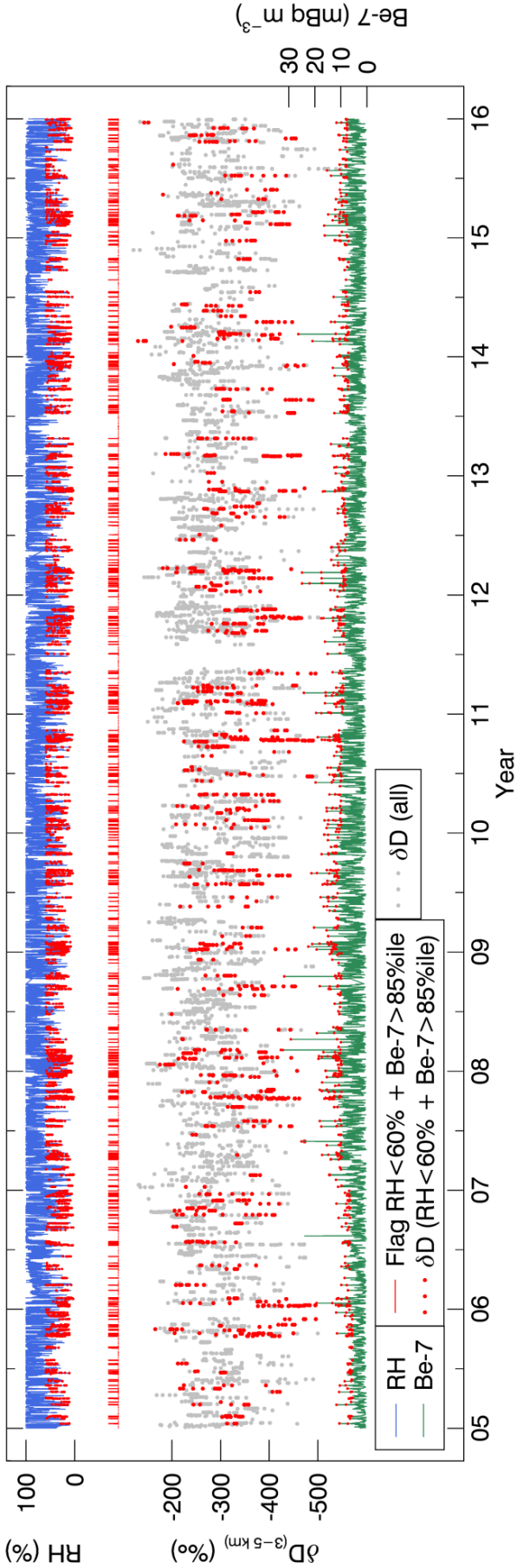

Figure 4.11: Deep stratospheric intrusions at Mt. Zugspitze in 2005–2015 derived from in situ observations of stratospheric tracers (relative humidity and Be-7) using DSTI-flag 1 and coincident FTIR data of lower tropospheric δD, i.e., deseasonalized hourly means of 3–5 km partial columns (Hausmann et al., 2017).

The significant shift of the lower tropospheric δD distribution to more HDO depleted δD values for DSTI events at Mt. Zugspitze agrees with the conception of intrusions originating in the strongly HDO depleted lower stratosphere region. However, the δD distribution for DSTI events exhibits a relatively large scatter, which implies that also weakly depleted air masses are found for DSTI events. This result is in line with relatively broad δD distributions found for the STI transport category in Sect. 4.3.2 and for STI events identified from lidar measurements (see Fig. 4.10). Correlation analysis for all coincident measurements of lower tropospheric δD (FTIR) and Be-7 (in situ) yields a significant negative correlation (99 % confidence) with a correlation coefficient of $R = -0.295$. This negative correlation is in line with expectations, as Be-7 concentrations increase with altitude towards the lower stratosphere, whereas δD values decrease with altitude.

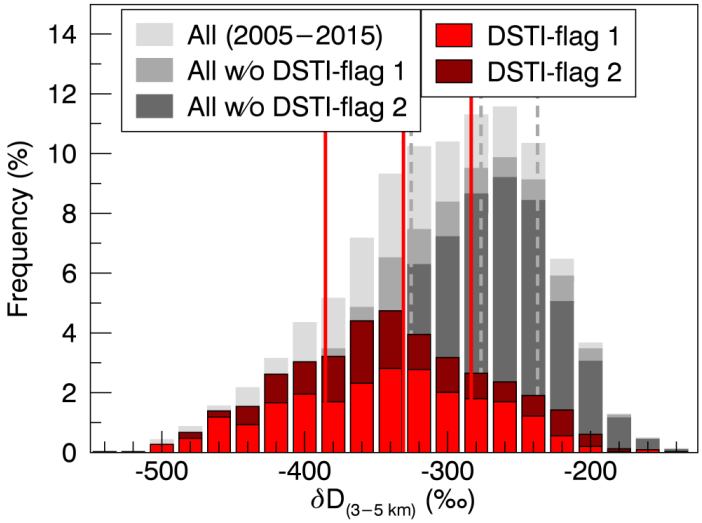

Figure 4.12: Distribution of lower tropospheric δD (deseasonalized hourly means of 3–5 km partial columns) for deep stratospheric intrusion events identified from Zugspitze in situ observations using two different flags (DSTI-flag 1: RH $< 60\,\%$ and Be-7 $> 85^{\text{th}}$ percentile; DSTI-flag 2: RH $< 60\,\%$ and $1 \times$ RH $< 30\,\%$ within $\pm$ 6 hours). For comparison, the distribution is shown for all FTIR measurements coincident with in situ data in 2005–2015 as well as all data excluding DSTI events. Vertical lines indicate median and 25^{th}–75^{th} percentile range of the distribution for DSTI-flag 1 and all data without DSTI-flag 1 (Hausmann et al., 2017).

4.4 Conclusions

In this chapter, vertical soundings of tropospheric water vapor and δD (2005–2015) were derived from mid-infrared FTIR measurements at Mt. Zugspitze (47° N, 11° E; 2964 m a.s.l.). These high-altitude observations performed within the NDACC framework provide a unique possibility to monitor Central European background conditions, as the site is mostly located above the moist boundary layer. Beside water vapor profiles with optimized vertical resolution (DOFS = 2.8), the retrieval provides H_2O-δD pairs with consistent vertical resolution (DOFS = 1.6 for H_2O and δD) and maximum vertical sensitivity in the free troposphere (around 5 km a.s.l.), which were applied in this chapter. Trend analysis for the Zugspitze time series of integrated water vapor and column-based δD reveals no significant trends for 2005–2015. Nevertheless, the IWV trend of 2.4 [−5.8, 10.6] % decade^{-1}

(statistically insignificant, 95 % confidence interval) can be reconciled with the temperature increase at Mt. Zugspitze over this time period (1.3 [0.5, 2.1] K decade^{-1}) assuming constant relative humidity. Seasonal variations in free tropospheric H_2O and δD exhibit amplitudes of 140 % and 50 % of the respective overall means. The minima (maxima) in January (July) are in agreement with changing sea surface temperature of the Atlantic Ocean.

Consistent H_2O-δD observations are a valuable proxy for atmospheric transport pathways. The potential of this new transport tracer was demonstrated by analyzing a vast compilation of backward trajectories to the free troposphere above Mt. Zugspitze (5 km a.s.l.). Distinct moisture pathways to the Central European free troposphere were identified depending on observed δD levels. While days with low column-based δD observations ($\delta D_{col} < 5^{th}$ percentile) are predominantly associated with dry air masses originating in higher latitudes (62° N) and altitudes (6.5 km), high δD days ($\delta D_{col} > 95^{th}$ percentile) are mostly related to moist air masses arriving from lower latitudes (46° N) and altitudes (4.6 km). Backward trajectory classification indicates that H_2O-δD observations are influenced by three main long-range transport patterns towards Mt. Zugspitze assessed in previous studies: (i) intercontinental transport from North America (TUS), (ii) intercontinental transport from Northern Africa (TNA), and (iii) stratospheric air intrusions (STI). The FTIR data exhibit significantly differing signatures in free-tropospheric H_2O-δD pairs for TUS (mean ± 2 SE: $VMR_{H_2O} = 2.4\,[2.3, 2.6] \times 10^3$ ppmv, $\delta D = -315\,[-326, -303]$ ‰), TNA ($VMR_{H_2O} = 2.8\,[2.6, 2.9] \times 10^3$ ppmv, $\delta D = -251\,[-257, -246]$ ‰), and STI ($VMR_{H_2O} = 1.2\,[1.1, 1.3] \times 10^3$ ppmv, $\delta D = -384\,[-397, -372]$ ‰). For TUS events, air masses have their origin in the moist boundary layer and H_2O-δD observations depend on the surface temperature of their oceanic or continental source region and the degree of dehydration and HDO depletion having occurred during updrafts in warm conveyor belts. TNA events are associated with dry convection of moist boundary layer air and therefore with import of relatively moist and weakly HDO depleted air masses to Central Europe. In contrast, during STI events predominantly dry and HDO depleted air masses are imported, which originate in the extremely dry and HDO depleted lowermost stratosphere.

These long-range transport patterns potentially involve the import of various trace constituents to the Central European free troposphere, i.e., import of pollution from North America (e.g., aerosol, ozone, carbon monoxide), Saharan mineral dust, stratospheric ozone and other airborne species such as pollen. The results presented above provide evidence that H_2O-δD observations are a valuable proxy for the potential transport of such tracers. To validate this finding, a data base of transport events (TNA and STI) covering 2013–2015 is consulted, which is deduced by data filtering from in situ measurements at Mt. Zugspitze and lidar profiles at near-by Garmisch. Indeed, the FTIR data related to these verified TNA events (27 days) exhibit characteristic fingerprints in IWV (5.5 [4.9, 6.1] mm) and δD_{col} (−266 [−284, −247] ‰), which are significantly distinguishable from the rest of the time series (IWV = 4.3 [4.1, 4.5] mm, $\delta D_{col} = -316\,[-324, -308]$ ‰). This holds true on 1-σ level for 136 STI days (mean ± 1 SE: IWV = 4.2 [4.0, 4.3] mm, $\delta D_{col} = -322\,[-327, -316]$ ‰) with respect to the remainder (IWV = 4.6 [4.5, 4.8] mm, $\delta D_{col} = -302\,[-307, -297]$ ‰). Furthermore, deep stratospheric intrusions to the Zugspitze summit (derived by in situ humidity and beryllium-7 data filtering) show a significantly lower mean value (−334 [−337, −330] ‰) of lower-tropospheric δD (3–5 km a.s.l.) on 2-σ level than the rest of the 2005–2015 time series (−284 [−286, −282] ‰). Our results show that consistent H_2O-δD observations at Mt. Zugspitze can serve as an operational indicator for long-range transport events to Central Europe.

In future work, backward trajectory classification to identify STI events could be improved, e.g., by application of a dynamical tropopause definition. H_2O-δD observations could also be combined with FTIR data of other relevant trace species, such as ozone or carbon monoxide, for more reliable detection of transport events. Furthermore, H_2O-δD profile information provided by FTIR measurements (approximately two tropospheric partial columns) could be combined with lidar or radiosonde humidity profiles with high vertical resolution, especially for studying thin filaments of stratospheric air intrusions. Regarding long-term trends, water vapor trends could be estimated for different transport categories to investigate to what extent changing transport patterns contribute to observed water vapor trends. Of particular importance would be research on the connection between lower stratospheric humidity trends, trends in the frequency of stratosphere–troposphere transport events, and tropospheric water vapor trends.

Finally, combining H_2O-δD measurements from all globally distributed NDACC sites with observations from in situ and lidar networks and operational transport modeling could provide a unique new database to study the impact of atmospheric transport with respect to climate, air quality, and human health. H_2O-δD data could serve as an indicator for the presence of pronounced transport events at Mt. Zugspitze to initiate case studies using observations of the respectively relevant tracers (e.g., humidity, aerosols, ozone, pollen). On demand, further FTIR sites could be included, which are located along simulated transport trajectories. Particular focus has to be laid on deepening our knowledge on the coupling of changing transport patterns in the global circulation, changes in the intensity of the hydrological cycle, and climate change.

Chapter 5

Summary and Outlook

Water vapor and methane play a key role in the Earth's energy budget. As predominant greenhouse gas, atmospheric water vapor accounts for about 60 % of the natural greenhouse effect. Moreover, anthropogenic climate forcing is substantially amplified by the water vapor feedback mechanism. In turn, methane is the second most important anthropogenic greenhouse gas after carbon dioxide and responsible for about 20 % of global warming since preindustrial times. Overall, water vapor and methane are among the most dominant greenhouse gases in the climate system. Therefore, long-term monitoring of these atmospheric trace gases is an important task to improve our understanding of climate change and to develop effective mitigation strategies.

In the present dissertation, long-term time series of water vapor and methane were derived from mid-infrared solar absorption measurements at Mt. Zugspitze (47.42° N, 10.98° E; 2964 m a.s.l.). This high-altitude observatory has been operated within the NDACC framework since 1995 to monitor a large number of atmospheric trace constituents under free tropospheric background conditions. Remote sensing of water vapor and methane represents a major challenge with respect to measurement accuracy and precision as these trace gases exhibit very different degrees of variability. While integrated water vapor varies over three orders of magnitude during the course of a year, the variability of column-averaged methane is typically smaller than 1 % of its background level.

Based on analyzing these long-term observations at Mt. Zugspitze, this thesis focused on two so far unresolved issues in current climate research, regarding the source attribution of methane trends and the large-scale transport of water vapor and other relevant trace species in the atmosphere. In this context, two essential research questions were examined:

- How is it possible to quantify the contribution of methane emissions from the oil and natural gas industry to the renewed methane increase since 2007 and how large is this contribution?
- Are long-term observations of water vapor and its isotopes able to yield new insights in long-range transport pathways of atmospheric air masses to Central Europe?

Methods developed within the scope of this dissertation in order to answer these research questions as well as results achieved are summarized in the next two sections, which are followed by an outlook to future research projects.

Oil and Gas Contribution to Renewed Methane Increase

After a period of stagnation in the growth rate of atmospheric methane (1999–2006), increase resumed in 2007 and has persisted through 2014. Several recent studies suggest that this renewed methane increase has likely been driven by a rise in emissions from natural wetlands as well as from the production of fossil fuels. However, the relative contribution of these two drivers remains highly uncertain. A remarkable factor in this context is the simultaneous massive growth in the US oil and natural gas production, facilitated by new drilling technologies (i.e., hydraulic fracturing).

In the present thesis, an innovative approach was employed to quantify to what extent methane emissions from the oil and natural gas industry have contributed to the renewed methane increase since 2007. This estimate was achieved by combining trend observations of methane with measurements of ethane, which is a tracer for thermogenic methane emissions. Due to the low variability of column-averaged methane, trend analysis demands highly precise measurements. To meet these requirements, a novel correction method was applied to successfully eliminate pointing errors which affected a minor part of the Zugspitze data set. Harmonized time series of column-averaged methane and ethane were presented for two NDACC sites, representing midlatitude background conditions of the Northern and Southern Hemisphere (i.e., Zugspitze at 47° N and Lauder at 45° S). The renewed methane increase of about $6\,\mathrm{ppb\,yr^{-1}}$ has consistently occurred in both hemispheres since 2007. After a global ethane decrease since the 1980s, a trend reversal was identified in 2007 only in the Northern Hemisphere, while ethane has continued to decrease in the Southern Hemisphere. The significant correlation of methane and ethane time series at Zugspitze in the 2007–2014 period and the corresponding regression slope point to a thermogenic source with an ethane-to-methane ratio compatible with oil and natural gas emissions.

Methane and ethane observations at Zugspitze and Lauder were simulated by means of an atmospheric two-box model which allows attributing observed trends to optimized emission scenarios. Based on this top-down approach, the northern hemispheric ethane increase since 2007 was assigned to a linear increase in fugitive ethane emissions from the oil and natural gas industry, primarily located in the Northern Hemisphere. The associated increase in methane emissions was determined using observation-based ethane-to-methane ratios of fossil-fuel related emissions. The most plausible emission scenario revealed an oil and natural gas emission contribution of at least 39 % to the renewed methane increase since 2007. In addition, two limiting cases were considered which result in a minimum contribution of at least 18 % from pure oil emissions and 73 % from pure gas emissions, respectively. These results suggest that thermogenic methane emissions from the oil and natural gas industry have significantly contributed to the renewed methane increase since 2007. Consequently, detection and elimination of methane leakage from these infrastructures is essential to diminish emissions of this very effective greenhouse gas.

Water Vapor Isotopes as Atmospheric Transport Tracers

In this part of the present dissertation, vertical soundings of tropospheric water vapor and its D/H isotope ratio (δD) at Mt. Zugspitze were presented for the time period 2005–2015. Long-term trends over this period were found to be statistically insignificant for integrated water vapor as well as for column-based δD (95 % confidence interval). Nevertheless, the

weakly positive (insignificant) IWV trend could be reconciled with the moisture increase expected from rising temperatures at Mt. Zugspitze, assuming constant relative humidity. Multiannual data of free tropospheric water vapor and δD exhibit a strong seasonal cycle with summer maxima (July) and winter minima (January). Less HDO depletion occurs in spring compared with autumn, which is in agreement with varying sea surface temperatures of the Atlantic Ocean, i.e., the major moisture source for Central Europe.

Fractionation processes during phase transitions (evaporation, condensation, and sublimation) modify the isotopic composition of atmospheric water vapor which consequently contains valuable information on tropospheric moisture pathways. The aim of this dissertation is to examine the potential of H_2O-δD observations at Mt. Zugspitze for investigation of transport processes to Central Europe. Based on extensive backward trajectory simulations, distinct moisture transport pathways to the Central European free troposphere were identified depending on the observed level of column-based δD. According to large-scale isotope effects, low δD outliers were found to be predominantly associated with descending dry air masses from higher latitudes while high δD outliers are mostly connected with ascending moist air masses from lower latitudes. Backward trajectory classification indicates that H_2O-δD observations are influenced by three long-range transport patterns towards Mt. Zugspitze assessed in previous studies: intercontinental transport from North America (TUS), intercontinental transport from Northern Africa (TNA), and stratospheric intrusions (STI). These large-scale transport categories reveal significantly different signatures in H_2O-δD distributions at Mt. Zugspitze. For TUS events, H_2O-δD observations depend on surface temperature in the source region and the degree of dehydration having occurred during updraft in warm conveyor belts. During TNA events (dry convection of boundary layer air) relatively moist and weakly HDO depleted air masses are imported. In contrast, STI events are associated with import of predominantly dry and HDO depleted air masses.

These long-range transport patterns potentially involve the import of various trace constituents to the Central European free troposphere: import of pollution from North America (e.g., aerosol, ozone, and carbon monoxide), Saharan mineral dust, stratospheric ozone and other airborne species such as pollen. The above results provide evidence that H_2O-δD observations are a valuable proxy for the potential transport of such tracers. This finding was successfully validated by consulting a 3-year data base of transport events (TNA and STI) deduced by data filtering from lidar measurements at near-by Garmisch site. During these verified transport events, FTIR data exhibit characteristic fingerprints in IWV and column-based δD, which are clearly distinguishable from the rest of the time series (significant on 2-σ level for TNA, on 1-σ level for STI events). Furthermore, deep stratospheric intrusions to the Zugspitze summit, which were identified by data filtering of in situ measurements, are associated with significantly stronger HDO depletion in the lower-tropospheric δD partial column (3–5 km a.s.l.) than the rest of the 2005–2015 time series. These results demonstrated that consistent H_2O-δD observations at Mt. Zugspitze can serve as an operational indicator for long-range transport events, potentially impacting regional climate, air quality, as well as human health in Central Europe.

Outlook

Based on the joint evaluation of methane and ethane time series, it was possible to attribute a significant share of the renewed methane increase (2007–2014) to thermogenic methane emissions in the Northern Hemisphere. The trend reversal in northern hemispheric ethane concentrations, presented in that context, was confirmed by several recent studies (Franco et al., 2016; Hakola and Hellén, 2016; Helmig et al., 2016; Kort et al., 2016). With the help of two-box model simulations, ethane and methane observations were successfully linked with hemispheric emission scenarios. However, this highly simplified atmospheric model did not allow the localization of emissions on a continental or regional scale. Using global surface observations, Helmig et al. (2016) recently succeeded to attribute the positive ethane trend primarily to oil and natural gas emissions in North America. In addition, Turner et al. (2016) stated that US methane emissions increased by more than 30 % within 2002–2014, probably accounting for 30–60 % of the global methane increase in this period. In combination, these results suggest a connection between the renewed methane increase and the North American oil and natural gas boom in recent years.

Besides the ethane-based approach applied in this thesis, methane source types can be identified by assessing their distinct signatures in the composition of methane isotopes. Using this isotope-based approach, Schaefer et al. (2016) inferred that biogenic methane emissions have predominantly caused the renewed methane rise. This result is consistent with the ethane-based estimate presented here (i.e., a thermogenic contribution of at least 39 %). In fact, another isotope-based study proposed a combined increase in biogenic and thermogenic emissions as main driver of the renewed methane increase (Rice et al., 2016). Consequently, reconciling ethane-based and isotope-based approaches in a more sophisticated source–sink inversion study is an essential task to improve our ability of quantifying changes in the methane budget. Moreover, such efforts should account for methane sink variability (i.e., OH concentrations), potentially affecting methane trends.

Furthermore, global methane emissions have to be estimated at higher spatiotemporal resolution, than achieved so far, to allow for a detailed quantification of regional methane budgets. Valuable new atmospheric data sets are expected to be obtained from future satellite missions (Jacob et al., 2016). For example, TROPOMI (Sentinel-5 precursor mission, to be launched in 2017) is going to provide methane observations with daily global coverage and unprecedented spatial resolution. Specifically designed for methane observations, the first space-based lidar instrument MERLIN (planned launch in 2021) will collect data with high horizontal resolution, even under cloudy conditions. For the validation of these new satellite data products, it will still be necessary to expand efforts within ground-based networks such as NDACC and TCCON regarding the generation of long-term high-precision-and-accuracy data sets. Overall, the aim will be to reduce considerable inconsistencies which persist between methane emission estimates from bottom-up inventories and from top-down inversion studies. By filling gaps in our current knowledge of the global methane budget, we will be able to develop effective emission regulation strategies, urgently needed to implement the Paris Agreement on climate change mitigation.

For sustained progress in climate change mitigation, also atmospheric circulation patterns and transport processes have to be taken into account, which underlines the need for further investigations in this context. This thesis demonstrated that water vapor isotope measurements can yield further insight into transport processes to Central Europe. Results

presented were mainly based on the analysis of free-tropospheric as well as column-based H_2O-δD data. In future work, also more detailed profile information of H_2O and δD has to be exploited, which is provided by ground-based FTIR to a limited extend only. Higher vertical resolution can be achieved by lidar measurements, satellite data, and in situ observations. Such profile information is necessary to resolve, for example, thin stratospheric intrusion filaments. Therefore, profile information provides the basis for recording the entire range of transport events to Central Europe, which is required to comprehensively quantify the impact of long-range transport on regional climate and air quality.

It is of particular importance to determine water vapor trends in distinct altitude regions. Especially, water vapor trends in the upper troposphere and lower stratosphere need to be accurately monitored as they are highly relevant for surface climate change (Solomon et al., 2010). However, water vapor measurements in this extremely dry altitude region are sparse and subject to a high degree of uncertainty (Müller et al., 2016). Stratospheric water vapor concentrations are mainly driven by tropical tropopause temperatures and oxidation of methane, but these drivers cannot fully explain the trends observed. Recently, (Hegglin et al., 2014) presented a merged satellite data set which provides vertically resolved water vapor trends in the stratosphere covering a twenty-year period. This study suggested that long-term changes of circulation patterns need to be considered in order to fully explain stratospheric water vapor trends. In this context, Remsberg (2015) highlighted the potential of methane satellite data as diagnostic tracer for the detection of changes in the Brewer–Dobson circulation. Furthermore, the role of extratropical moisture pathways along warm conveyor belts or deep convection has to be further investigated regarding the inflow of tropospheric moisture into the lower stratosphere region (Zahn et al., 2014). Moreover, it has to be considered that these transport processes will likely be modified with changing general circulation patterns under changing climate conditions.

In addition to lower stratospheric water vapor trends, climate feedback mechanisms represent another essential contribution to climate change and may amplify or diminish anthropogenic climate forcing. Currently, the strongest response to global warming is the positive water vapor feedback which is relatively well understood. However, sign and strength of other climate feedback processes related to the global water cycle are still largely unknown, for example, cloud feedback mechanisms (Bony et al., 2015). Consequently, it remains a major challenge to accurately represent such feedback processes in climate models (Kamae et al., 2016), adversely affecting our ability to predict climate change. Therefore, it is an essential goal of ongoing climate research (Simmons et al., 2016) to improve our understanding of the interactions between global water cycle, atmospheric circulation, and climate change.

Bibliography

Akagi, S. K., Yokelson, R. J., Wiedinmyer, C., Alvarado, M. J., Reid, J. S., Karl, T., Crounse, J. D., and Wennberg, P. O.: Emission factors for open and domestic biomass burning for use in atmospheric models, Atmos. Chem. Phys., 11, 4039–4072, doi:10.5194/acp-11-4039-2011, 2011.

Andreae, M. O. and Merlet, P.: Emission of trace gases and aerosols from biomass burning, Glob. Biogeochem. Cycles, 15, 955–966, doi:10.1029/2000GB001382, 2001.

Angelbratt, J., Mellqvist, J., Simpson, D., Jonson, J. E., Blumenstock, T., Borsdorff, T., Duchatelet, P., Forster, F., Hase, F., Mahieu, E., De Mazière, M., Notholt, J., Petersen, A. K., Raffalski, U., Servais, C., Sussmann, R., Warneke, T., and Vigouroux, C.: Carbon monoxide (CO) and ethane (C_2H_6) trends from ground-based solar FTIR measurements at six European stations, comparison and sensitivity analysis with the EMEP model, Atmos. Chem. Phys., 11, 9253–9269, doi:10.5194/acp-11-9253-2011, 2011.

Aydin, M., Verhulst, K. R., Saltzman, E. S., Battle, M. O., Montzka, S. A., Blake, D. R., Tang, Q., and Prather, M. J.: Recent decreases in fossil-fuel emissions of ethane and methane derived from firn air, Nature, 476, 198–201, doi:10.1038/nature10352, 2011.

Bader, W., Bovy, B., Conway, S., Strong, K., Smale, D., Turner, A. J., Blumenstock, T., Boone, C., Collaud Coen, M., Coulon, A., Garcia, O., Griffith, D. W. T., Hase, F., Hausmann, P., Jones, N., Krummel, P., Murata, I., Morino, I., Nakajima, H., O'Doherty, S., Paton-Walsh, C., Robinson, J., Sandrin, R., Schneider, M., Servais, C., Sussmann, R., and Mahieu, E.: The recent increase of atmospheric methane from 10 years of groundbased NDACC FTIR observations since 2005, Atmos. Chem. Phys., 17, 2255–2277, doi:10.5194/acp-17-2255-2017, 2017.

Barthlott, S., Schneider, M., Hase, F., Blumenstock, T., Kiel, M., Dubravica, D., García, O. E., Sepúlveda, E., Mengistu Tsidu, G., Takele Kenea, S., Grutter, M., Plaza, E. F., Stremme, W., Strong, K., Weaver, D., Palm, M., Warneke, T., Notholt, J., Mahieu, E., Servais, C., Jones, N., Griffith, D. W. T., Smale, D., , and Robinson, J.: Tropospheric water vapour isotopologue data ($H_2^{16}O$, $H_2^{18}O$, and $HD^{16}O$) as obtained from NDACC/FTIR solar absorption spectra, Earth Syst. Sci. Data, 9, 15–29, doi:10.5194/essd-9-15-2017, 2017.

Beekmann, M., Ancellet, G., Blonsky, S., De Muer, D., Ebel, A., Elbern, H., Hendricks, J., Kowol, J., Mancier, C., Sladkovic, R., and Smit, H. G. J.: Regional and global tropopause fold occurrence and related ozone flux across the tropopause, J. Atmos. Chem., 28, 29–44, doi:10.1023/A:1005897314623, 1997.

Bengtsson, L., Bonnet, R. M., Calisto, M., Destouni, G., Gurney, R., Johannessen, J.,

Kerr, Y., Lahoz, W. A., and Rast, M., eds.: The Earth's Hydrological Cycle, vol. 46 of *Space Science Series of ISSI*, Springer, Dordrecht, The Netherlands, doi:10.1007/978-94-017-8789-5, 2014.

Bergamaschi, P., Houweling, S., Segers, A., Krol, M., Frankenberg, C., Scheepmaker, R. A., Dlugokencky, E., Wofsy, S. C., Kort, E. A., Sweeney, C., Schuck, T., Brenninkmeijer, C., Chen, H., Beck, V., and Gerbig, C.: Atmospheric CH_4 in the first decade of the 21st century: Inverse modeling analysis using SCIAMACHY satellite retrievals and NOAA surface measurements, J. Geophys. Res., 118, 7350–7369, doi:10.1002/jgrd.50480, 2013.

Boesch, H., Deutscher, N. M., Warneke, T., Byckling, K., Cogan, A. J., Griffith, D. W. T., Notholt, J., Parker, R. J., and Wang, Z.: HDO/H2O ratio retrievals from GOSAT, Atmos. Meas. Tech., 6, 599–612, doi:10.5194/amt-6-599-2013, 2013.

Bony, S., Stevens, B., Frierson, D. M. W., Jakob, C., Kageyama, M., Pincus, R., Shepherd, T. G., Sherwood, S. C., Siebesma, A. P., Sobel, A. H., Watanabe, M., and Webb, M. J.: Clouds, circulation and climate sensitivity, Nat. Geosci., 8, 261–268, doi:10.1038/ngeo2398, 2015.

Borbon, A., Gilman, J., Kuster, W., Grand, N., Chevaillier, S., Colomb, A., Dolgorouky, C., Gros, V., Lopez, M., Sarda-Esteve, R., Holloway, J., Stutz, J., Petetin, H., McKeen, S., Beekmann, M., Warneke, C., Parrish, D. D., and de Gouw, J. A.: Emission ratios of anthropogenic volatile organic compounds in northern mid-latitude megacities: Observations versus emission inventories in Los Angeles and Paris, J. Geophys. Res., 118, 2041–2057, doi:10.1002/jgrd.50059, 2013.

Bousquet, P., Ringeval, B., Pison, I., Dlugokencky, E. J., Brunke, E.-G., Carouge, C., Chevallier, F., Fortems-Cheiney, A., Frankenberg, C., Hauglustaine, D. A., Krummel, P. B., Langenfelds, R. L., Ramonet, M., Schmidt, M., Steele, L. P., Szopa, S., Yver, C., Viovy, N., and Ciais, P.: Source attribution of the changes in atmospheric methane for 2006–2008, Atmos. Chem. Phys., 11, 3689–3700, doi:10.5194/acp-11-3689-2011, 2011.

Brandt, A. R., Heath, G. A., Kort, E. A., O'Sullivan, F., Pétron, G., Jordaan, S., Tans, P., Wilcox, J., Gopstein, A. M., Arent, D., Wofsy, S., Brown, N. J., Bradley, R., Stucky, G. D., Eardley, D., and Harriss, R.: Methane leaks from North American natural gas systems, Science, 343, 733–735, doi:10.1126/science.1247045, 2014.

Brasseur, G. P. and Solomon, S.: Aeronomy of the Middle Atmosphere: Chemistry and Physics of the Stratosphere an Mesosphere, vol. 32 of *Atmospheric and Oceanographic Sciences Library*, Springer, Dordrecht, The Netherlands, 3rd edn., 2005.

Bruhwiler, L., Dlugokencky, E., Masarie, K., Ishizawa, M., Andrews, A., Miller, J., Sweeney, C., Tans, P., and Worthy, D.: CarbonTracker-CH_4: an assimilation system for estimating emissions of atmospheric methane, Atmos. Chem. Phys., 14, 8269–8293, doi:10.5194/acp-14-8269-2014, 2014.

Carnuth, W., Kempfer, U., and Trickl, T.: Highlights of the tropospheric lidar studies at IFU within the TOR project, Tellus B, 54, 163–185, doi:10.1034/j.1600-0889.2002.00245.x, 2002.

Christner, E.: Messungen von Wasserisotopologen von der planetaren Grenzschicht bis zur oberen Troposphäre zur Untersuchung des hydrologischen Kreislaufs, Ph.D. thesis, Karl-

sruhe Institute of Technology, Germany, available at: https://publikationen.bibliothek.kit.edu/1000046021 (last access: 3 October 2016), 2015.

Conley, S., Franco, G., Faloona, I., Blake, D. R., Peischl, J., and Ryerson, T. B.: Methane emissions from the 2015 Aliso Canyon blowout in Los Angeles, CA, Science, 351, 1317–1320, doi:10.1126/science.aaf2348, 2016.

Craig, H.: Standard for reporting concentrations of deuterium and oxygen-18 in natural waters, Science, 133, 1833–1834, doi:10.1126/science.133.3467.1833, 1961.

Damoah, R., Spichtinger, N., Forster, C., James, P., Mattis, I., Wandinger, U., Beirle, S., Wagner, T., and Stohl, A.: Around the world in 17 days – hemispheric-scale transport of forest fire smoke from Russia in May 2003, Atmos. Chem. Phys., 4, 1311–1321, doi:10.5194/acp-4-1311-2004, 2004.

Dansgaard, W.: Stable isotopes in precipitation, Tellus, 16, 436–468, doi:10.1111/j.2153-3490.1964.tb00181.x, 1964.

Davis, S. P., Abrams, M. C., and Brault, J. W.: Fourier Transform Spectrometry, Academic Press, San Diego, USA, 2001.

Dils, B., Cui, J., Henne, S., Mahieu, E., Steinbacher, M., and De Mazière, M.: 1997–2007 CO trend at the high Alpine site Jungfraujoch: a comparison between NDIR surface in situ and FTIR remote sensing observations, Atmos. Chem. Phys., 11, 6735–6748, doi:10.5194/acp-11-6735-2011, 2011.

Dlugokencky, E., Masarie, K., Lang, P., and Tans, P.: Continuing decline in the growth rate of the atmospheric methane burden, Nature, 393, 447–450, doi:10.1038/30934, 1998.

Dlugokencky, E. J., Bruhwiler, L., White, J. W. C., Emmons, L. K., Novelli, P. C., Montzka, S. A., Masarie, K. A., Lang, P. M., Crotwell, A. M., Miller, J. B., and Gatti, L. V.: Observational constraints on recent increases in the atmospheric CH_4 burden, Geophys. Res. Lett., 36, L18 803, doi:10.1029/2009GL039780, 2009.

Dlugokencky, E. J., Nisbet, E. G., Fisher, R., and Lowry, D.: Global atmospheric methane: budget, changes and dangers, Philos. T. Roy. Soc. A, 369, 2058–2072, doi:10.1098/rsta.2010.0341, 2011.

Dlugokencky, E. J., Crotwell, A. M., Crotwell, M., Lang, P. M., Masarie, K. A., Michel, S., and Bruhwiler, L.: What have we learned from three decades of atmospheric CH_4 measurements?, International Conference on non-CO_2 Greenhouse Gases, InGOS, Utrecht, The Netherlands, 21–24 September, 2015a.

Dlugokencky, E. J., Lang, P. M., Crotwell, A. M., Masarie, K. A., and Crotwell, M. J.: Atmospheric Methane Dry Air Mole Fractions from the NOAA ESRL Carbon Cycle Cooperative Global Air Sampling Network, available at: ftp://aftp.cmdl.noaa.gov/data/trace_gases/ch4/flask/surface (last access: 16 February 2016), 2015b.

Eckhardt, S., Stohl, A., Wernli, H., James, P., Forster, C., and Spichtinger, N.: A 15-year climatology of warm conveyor belts, J. Clim., 17, 218–237, doi:10.1175/1520-0442(2004)017⟨0218:AYCOWC⟩2.0.CO;2, 2004.

Eisele, H., Scheel, H. E., Sladkovic, R., and Trickl, T.: High-Resolution Lidar Mea-

surements of Stratosphere–Troposphere Exchange, J. Atmos. Sci., 56, 319–330, doi:10.1175/1520-0469(1999)056⟨0319:hrlmos⟩2.0.co;2, 1999.

Engelstaedter, S., Tegen, I., and Washington, R.: North African dust emissions and transport, Earth-Sci. Rev., 79, 73–100, doi:10.1016/j.earscirev.2006.06.004, 2006.

Etiope, G. and Ciccioli, P.: Earth's Degassing: A Missing Ethane and Propane Source, Science, 323, 478–478, doi:10.1126/science.1165904, 2009.

Fernandes, S. D., Trautmann, N. M., Streets, D. G., Roden, C. A., and Bond, T. C.: Global biofuel use, 1850–2000, Glob. Biogeochem. Cycles, 21, GB2019, doi:10.1029/2006gb002836, 2007.

Field, R., Soltis, J., and Murphy, S.: Air quality concerns of unconventional oil and natural gas production, Env. Sci. Process. Impact., 16, 954–969, doi:10.1039/C4EM00081A, 2014.

Flentje, H., Briel, B., Beck, C., Collaud Coen, M., Fricke, M., Cyrys, J., Gu, J., Pitz, M., and Thomas, W.: Identification and monitoring of Saharan dust: An inventory representative for south Germany since 1997, Atmos. Environ., 109, 87–96, doi:10.1016/j.atmosenv.2015.02.023, 2015.

Forster, C., Wandinger, U., Wotawa, G., James, P., Mattis, I., Althausen, D., Simmonds, P., O'Doherty, S., Jennings, S. G., Kleefeld, C., Schneider, J., Trickl, T., Kreipl, S., Jäger, H., and Stohl, A.: Transport of boreal forest fire emissions from Canada to Europe, J. Geophys. Res., 106, 22 887–22 906, doi:10.1029/2001JD900115, 2001.

Franco, B., Bader, W., Toon, G., Bray, C., Perrin, A., Fischer, E., Sudo, K., Boone, C., Bovy, B., Lejeune, B., Servais, C., and Mahieu, E.: Retrieval of ethane from ground-based FTIR solar spectra using improved spectroscopy: Recent burden increase above Jungfraujoch, J. Quant. Spectrosc. Ra., 160, 36–49, doi:10.1016/j.jqsrt.2015.03.017, 2015.

Franco, B., Mahieu, E., Emmons, L. K., Tzompa-Sosa, Z. A., Fischer, E. V., Sudo, K., Bovy, B., Conway, S., Griffin, D., Hannigan, J. W., Strong, K., and Walker, K. A.: Evaluating ethane and methane emissions associated with the development of oil and natural gas extraction in North America, Environ. Res. Lett., 11, 044 010, doi:10.1088/1748-9326/11/4/044010, 2016.

Frankenberg, C., Aben, I., Bergamaschi, P., Dlugokencky, E. J., van Hees, R., Houweling, S., van der Meer, P., Snel, R., and Tol, P.: Global column-averaged methane mixing ratios from 2003 to 2009 as derived from SCIAMACHY: Trends and variability, J. Geophys. Res., 116, D04 302, doi:10.1029/2010JD014849, 2011.

Frankenberg, C., Wunch, D., Toon, G., Risi, C., Scheepmaker, R., Lee, J.-E., Wennberg, P., and Worden, J.: Water vapor isotopologue retrievals from high-resolution GOSAT shortwave infrared spectra, Atmos. Meas. Tech., 6, 263–274, doi:10.5194/amt-6-263-2013, 2013.

Fromm, M., Lindsey, D. T., Servranckx, R., Yue, G., Trickl, T., Sica, R., Doucet, P., and Godin-Beekmann, S.: The Untold Story of Pyrocumulonimbus, B. Am. Meteorol. Soc., 91, 1193–1209, doi:10.1175/2010bams3004.1, 2010.

Galewsky, J., Sobel, A., and Held, I.: Diagnosis of subtropical humidity dynamics using tracers of last saturation, J. Atmos. Sci., 62, 3353–3367, doi:10.1175/JAS3533.1, 2005.

García, R., Marsh, D., Kinnison, D., Boville, B., and Sassi, F.: Simulation of secular trends in the middle atmosphere, 1950–2003, J. Geophys. Res., 112, 2156–2202, doi: 10.1029/2006JD007485, 2007.

Gardiner, T., Forbes, A., de Mazière, M., Vigouroux, C., Mahieu, E., Demoulin, P., Velazco, V., Notholt, J., Blumenstock, T., Hase, F., Kramer, I., Sussmann, R., Stremme, W., Mellqvist, J., Strandberg, A., Ellingsen, K., and Gauss, M.: Trend analysis of greenhouse gases over Europe measured by a network of ground-based remote FTIR instruments, Atmos. Chem. Phys., 8, 6719–6727, doi:10.5194/acp-8-6719-2008, 2008.

Giglio, L., Randerson, J. T., and van der Werf, G. R.: Analysis of daily, monthly, and annual burned area using the fourth-generation global fire emissions database (GFED4), J. Geophys. Res. Biogeo., 118, 317–328, doi:10.1002/jgrg.20042, 2013.

Gisi, M., Hase, F., Dohe, S., and Blumenstock, T.: Camtracker: a new camera controlled high precision solar tracker system for FTIR-spectrometers, Atmos. Meas. Tech., 4, 47–54, doi:10.5194/amt-4-47-2011, 2011.

González, Y., Schneider, M., Dyroff, C., Rodríguez, S., Christner, E., García, O. E., Cuevas, E., Bustos, J. J., Ramos, R., Guirado-Fuentes, C., Barthlott, S., Wiegele, A., and Sepúlveda, E.: Detecting moisture transport pathways to the subtropical North Atlantic free troposphere using paired H2O-δD in situ measurements, Atmos. Chem. Phys., 16, 4251–4269, doi:10.5194/acp-16-4251-2016, 2016.

Hakola, H. and Hellén, H.: Atmospheric chemistry: The return of ethane, Nat. Geosci., 9, 475–476, doi:10.1038/ngeo2736, 2016.

Hanisco, T. F., Moyer, E. J., Weinstock, E. M., St. Clair, J. M., Sayres, D. S., Smith, J. B., Lockwood, R., Anderson, J. G., Dessler, A. E., Keutsch, F. N., Spackman, J. R., Read, W. G., and Bui, T. P.: Observations of deep convective influence on stratospheric water vapor and its isotopic composition, Geophys. Res. Lett., 34, L04 814, doi:10.1029/2006gl027899, 2007.

Harries, J., Carli, B., Rizzi, R., Serio, C., Mlynczak, M., Palchetti, L., Maestri, T., Brindley, H., and Masiello, G.: The Far-infrared Earth, Rev. Geophys., 46, RG4004, doi:10.1029/2007rg000233, 2008.

Hartmann, D. L., Klein Tank, A. M. G., Rusticucci, M., Alexander, L. V., Bronnimann, S., Charabi, Y., Dentener, F. J., Dlugokencky, E. J., Easterling, D. R., Kaplan, A., Soden, B. J., Thorne, P. W., Wild, M., and Zhai, P.: Observations: Atmosphere and Surface, in: Climate Change 2013: The Physical Science Basis. Contribution of Working Group I to the Fifth Assessment Report of the Intergovernmental Panel on Climate Change, edited by Stocker, T. F., Qin, D., Plattner, G.-K., Tignor, M., Allen, S. K., Boschung, J., Nauels, A., Xia, Y., Bex, V., and Midgley, P. M., Cambridge University Press, Cambridge, United Kingdom and New York, USA, 2013.

Hase, F.: Inversion von Spurengasprofilen aus hochaufgelösten bodengebundenen FTIR-Messungen in Absorption, Ph.D. thesis, Karlsruhe Institute of Technology, Germany, available at: http://www.imk-asf.kit.edu/downloads/bod/disshase.pdf (last access: 22 August 2016), 2000.

Hase, F., Hannigan, J., Coffey, M., Goldman, A., Höpfner, M., Jones, N., Rinsland, C., and Wood, S.: Intercomparison of retrieval codes used for the analysis of high-

resolution, ground-based FTIR measurements, J. Quant. Spectrosc. Ra., 87, 25–52, doi:10.1016/j.jqsrt.2003.12.008, 2004.

Hausmann, P., Sussmann, R., and Smale, D.: Contribution of oil and natural gas production to renewed increase in atmospheric methane (2007–2014): top–down estimate from ethane and methane column observations, Atmos. Chem. Phys., 16, 3227–3244, doi: 10.5194/acp-16-3227-2016, 2016.

Hausmann, P., Sussmann, R., Trickl, T., and Schneider, M.: A decadal time series of water vapor and D/H isotope ratios above Zugspitze: transport patterns to central Europe, Atmos. Chem. Phys., 17, 7635–7651, doi:10.5194/acp-17-7635-2017, 2017.

Hegglin, M. I., Plummer, D. A., Shepherd, T. G., Scinocca, J. F., Anderson, J., Froidevaux, L., Funke, B., Hurst, D., Rozanov, A., Urban, J., von Clarmann, T., Walker, K. A., Wang, H. J., Tegtmeier, S., and Weigel, K.: Vertical structure of stratospheric water vapour trends derived from merged satellite data, Nat. Geosci., 7, 768–776, doi:10.1038/ngeo2236, 2014.

Heimann, M.: Atmospheric science: Enigma of the recent methane budget, Nature, 476, 157–158, doi:10.1038/476157a, 2011.

Held, I. M. and Soden, B. J.: Water Vapor Feedback and Global Warming, Annu. Rev. Energ. Environ., 25, 441–475, doi:10.1146/annurev.energy.25.1.441, 2000.

Helmig, D., Petrenko, V., Martinerie, P., Witrant, E., Röckmann, T., Zuiderweg, A., Holzinger, R., Hueber, J., Thompson, C., White, J. W. C., Sturges, W., Baker, A., Blunier, T., Etheridge, D., Rubino, M., and Tans, P.: Reconstruction of Northern Hemisphere 1950–2010 atmospheric non-methane hydrocarbons, Atmos. Chem. Phys., 14, 1463–1483, doi:10.5194/acp-14-1463-2014, 2014.

Helmig, D., Rossabi, S., Hueber, J., Tans, P., Montzka, S. A., Masarie, K., Thoning, K., Plass-Duelmer, C., Claude, A., Carpenter, L. J., Lewis, A. C., Punjabi, S., Reimann, S., Vollmer, M. K., Steinbrecher, R., Hannigan, J. W., Emmons, L. K., Mahieu, E., Franco, B., Smale, D., and Pozzer, A.: Reversal of global atmospheric ethane and propane trends largely due to US oil and natural gas production, Nat. Geosci., 9, 490–495, doi:10.1038/ngeo2721, 2016.

Holloway, T., Fiore, A., and Hastings, M. G.: Intercontinental transport of air pollution: will emerging science lead to a new hemispheric treaty?, Environ. Sci. Technol., 37, 4535–4542, doi:10.1021/es034031g, 2003.

Howarth, R. W.: A bridge to nowhere: methane emissions and the greenhouse gas footprint of natural gas, Energy Sci. Eng., 2, 47–60, doi:10.1002/ese3.35, 2014.

Huntrieser, H. and Schlager, H.: Air pollution export from and import to Europe: Experimental evidence, in: Intercontinental Transport of Air Pollution, edited by Stohl, A., pp. 69–98, Springer, Berlin, Germany, doi:10.1007/b10681, 2004.

Huntrieser, H., Heland, J., Schlager, H., Forster, C., Stohl, A., Aufmhoff, H., Arnold, F., Scheel, H. E., Campana, M., Gilge, S., Eixmann, R., and Cooper, O.: Intercontinental air pollution transport from North America to Europe: Experimental evidence from airborne measurements and surface observations, J. Geophys. Res., 110, D01 305, doi: 10.1029/2004jd005045, 2005.

Husar, R. B.: Intercontinental Transport of Dust: Historical and Recent Observational Evidence, in: Intercontinental Transport of Air Pollution, edited by Stohl, A., pp. 277–294, Springer, Berlin, Germany, doi:10.1007/b10681, 2004.

IPCC: Climate Change 2013: The Physical Science Basis. Contribution of Working Group I to the Fifth Assessment Report of the Intergovernmental Panel on Climate Change, edited by Stocker, T. F., Qin, D., Plattner, G.-K., Tignor, M., Allen, S. K., Boschung, J., Nauels, A., Xia, Y., Bex, V., and Midgley, P. M., Cambridge University Press, Cambridge, United Kingdom and New York, NY, USA, 2013.

IRWG: Uniform Retrieval Parameter Summary, available at: http://www.acom.ucar.edu/irwg/IRWG_Uniform_RP_Summary-3.pdf (last access: 6 September 2016), 2014.

Israelevich, P., Ganor, E., Alpert, P., Kishcha, P., and Stupp, A.: Predominant transport paths of Saharan dust over the Mediterranean Sea to Europe, J. Geophys. Res., 117, D02 205, doi:10.1029/2011jd016482, 2012.

Itoh, H. and Narazaki, Y.: Fast descent routes from within or near the stratosphere to the surface at Fukuoka, Japan, studied using ^{7}Be measurements and trajectory calculations, Atmos. Chem. Phys., 16, 6241–6261, doi:10.5194/acp-16-6241-2016, 2016.

Jackson, R. B., Down, A., Phillips, N. G., Ackley, R. C., Cook, C. W., Plata, D. L., and Zhao, K.: Natural gas pipeline leaks across Washington, DC, Environ. Sci. Technol., 48, 2051–2058, doi:10.1021/es404474x, 2014.

Jacob, D. J., Turner, A. J., Maasakkers, J. D., Sheng, J., Sun, K., Liu, X., Chance, K., Aben, I., McKeever, J., and Frankenberg, C.: Satellite observations of atmospheric methane and their value for quantifying methane emissions, Atmos. Chem. Phys., 16, 14 371–14 396, doi:10.5194/acp-16-14371-2016, 2016.

Jochner, S., Lüpke, M., Laube, J., Weichenmeier, I., Pusch, G., Traidl-Hoffmann, C., Schmidt-Weber, C., Buters, J. T., and Menzel, A.: Seasonal variation of birch and grass pollen loads and allergen release at two sites in the German Alps, Atmos. Environ., 122, 83–93, doi:10.1016/j.atmosenv.2015.08.031, 2015.

Kai, F. M., Tyler, S. C., Randerson, J. T., and Blake, D. R.: Reduced methane growth rate explained by decreased Northern Hemisphere microbial sources, Nature, 476, 194–197, doi:10.1038/nature10259, 2011.

Kamae, Y., Ogura, T., Shiogama, H., and Watanabe, M.: Recent progress toward reducing the uncertainty in tropical low cloud feedback and climate sensitivity: a review, Geosci. Lett., 3, 1–10, doi:10.1186/s40562-016-0053-4, 2016.

Kang, M., Kanno, C. M., Reid, M. C., Zhang, X., Mauzerall, D. L., Celia, M. A., Chen, Y., and Onstott, T. C.: Direct measurements of methane emissions from abandoned oil and gas wells in Pennsylvania, P. Natl. A. Sci. USA, 111, 18 173–18 177, doi:10.1073/pnas.1408315111, 2014.

Karion, A., Sweeney, C., Pétron, G., Frost, G., Michael Hardesty, R., Kofler, J., Miller, B. R., Newberger, T., Wolter, S., Banta, R., Brewer, A., Dlugokencky, E., Lang, P., Montzka, S. A., Schnell, R., Tans, P., Trainer, M., Zamora, R., and Conley, S.: Methane emissions estimate from airborne measurements over a western United States natural gas field, Geophys. Res. Lett., 40, 4393–4397, doi:10.1002/grl.50811, 2013.

Kiehl, J. T. and Trenberth, K. E.: Earth's annual global mean energy budget, Bull. Am. Meteorol. Soc., 78, 197–208, doi:10.1175/1520-0477(1997)078⟨0197:EAGMEB⟩2.0.CO;2, 1997.

Kirschke, S., Bousquet, P., Ciais, P., Saunois, M., Canadell, J. G., Dlugokencky, E. J., Bergamaschi, P., Bergmann, D., Blake, D. R., Bruhwiler, L., Cameron-Smith, P., Castaldi, S., Chevallier, F., Feng, L., Fraser, A., Heimann, M., Hodson, E. L., Houweling, S., Josse, B., Fraser, P. J., Krummel, P. B., Lamarque, J.-F., Langenfelds, R. L., Le Quéré, C., Naik, V., O'Doherty, S., Palmer, P. I., Pison, I., Plummer, D., Poulter, B., Prinn, R. G., Rigby, M., Ringeval, B., Santini, M., Schmidt, M., Shindell, D. T., Simpson, I. J., Spahni, R., Steele, L. P., Strode, S. A., Sudo, K., Szopa, S., van der Werf, G. R., Voulgarakis, A., van Weele, M., Weiss, R. F., Williams, J. E., and Zeng, G.: Three decades of global methane sources and sinks, Nat. Geosci., 6, 813–823, doi:10.1038/ngeo1955, 2013.

Kort, E. A., Frankenberg, C., Costigan, K. R., Lindenmaier, R., Dubey, M. K., and Wunch, D.: Four corners: The largest US methane anomaly viewed from space, Geophys. Res. Lett., 41, 6898–6903, doi:10.1002/2014gl061503, 2014.

Kort, E. A., Smith, M. L., Murray, L. T., Gvakharia, A., Brandt, A. R., Peischl, J., Ryerson, T. B., Sweeney, C., and Travis, K.: Fugitive emissions from the Bakken shale illustrate role of shale production in global ethane shift, Geophys. Res. Lett., 43, 4617–4623, doi:10.1002/2016gl068703, 2016.

Lacour, J.-L., Risi, C., Clarisse, L., Bony, S., Hurtmans, D., Clerbaux, C., and Coheur, P.-F.: Mid-tropospheric δD observations from IASI/MetOp at high spatial and temporal resolution, Atmos. Chem. Phys., 12, 10 817–10 832, doi:10.5194/acp-12-10817-2012, 2012.

Lal, D. and Peters, B.: Cosmic Ray Produced Radioactivity on the Earth, Handbuch der Physik / Encyclopedia of Physics, pp. 551–612, doi:10.1007/978-3-642-46079-1_7, 1967.

Lefohn, A. S., Wernli, H., Shadwick, D., Oltmans, S. J., and Shapiro, M.: Quantifying the importance of stratospheric-tropospheric transport on surface ozone concentrations at high- and low-elevation monitoring sites in the United States, Atmos. Environ., 62, 646–656, doi:10.1016/j.atmosenv.2012.09.004, 2012.

Levin, I., Veidt, C., Vaughn, B. H., Brailsford, G., Bromley, T., Heinz, R., Lowe, D., Miller, J. B., Poß, C., and White, J. W. C.: No inter-hemispheric $\delta^{13}CH_4$ trend observed, Nature, 486, E3–E4, doi:10.1038/nature11175, 2012.

Lin, M., Fiore, A. M., Cooper, O. R., Horowitz, L. W., Langford, A. O., Levy, H., Johnson, B. J., Naik, V., Oltmans, S. J., and Senff, C. J.: Springtime high surface ozone events over the western United States: Quantifying the role of stratospheric intrusions, J. Geophys. Res., 117, D00V22, doi:10.1029/2012jd018151, 2012.

Liou, K. N.: An Introduction to Atmospheric Radiation, vol. 84 of *International Geophysics Series*, Elsevier Science, San Diego, USA, 2nd edn., 2002.

Madonna, E., Wernli, H., Joos, H., and Martius, O.: Warm Conveyor Belts in the ERA-Interim Dataset (1979–2010). Part I: Climatology and Potential Vorticity Evolution, J. Clim., 27, 3–26, doi:10.1175/jcli-d-12-00720.1, 2014.

Miller, S. M., Wofsy, S. C., Michalak, A. M., Kort, E. A., Andrews, A. E., Biraud, S. C., Dlugokencky, E. J., Eluszkiewicz, J., Fischer, M. L., Janssens-Maenhout, G., Miller,

B. R., Miller, J. B., Montzka, S. A., Nehrkorn, T., and Sweeney, C.: Anthropogenic emissions of methane in the United States, P. Natl. A. Sci. USA, 110, 20 018–20 022, doi:10.1073/pnas.1314392110, 2013.

Montzka, S. A., Krol, M., Dlugokencky, E., Hall, B., Jöckel, P., and Lelieveld, J.: Small interannual variability of global atmospheric hydroxyl, Science, 331, 67–69, doi:10.1126/science.1197640, 2011.

Moore, C. W., Zielinska, B., Pétron, G., and Jackson, R. B.: Air Impacts of Increased Natural Gas Acquisition, Processing, and Use: A Critical Review, Environ. Sci. Technol., 48, 8349–8359, doi:10.1021/es4053472, 2014.

Müller, R., Kunz, A., Hurst, D. F., Rolf, C., Krämer, M., and Riese, M.: The need for accurate long-term measurements of water vapor in the upper troposphere and lower stratosphere with global coverage, Earth's Future, 4, 25–32, doi:10.1002/2015ef000321, 2016.

Nicewonger, M. R., Verhulst, K. R., Aydin, M., and Saltzman, E. S.: Preindustrial atmospheric ethane levels inferred from polar ice cores: A constraint on the geologic sources of atmospheric ethane and methane, Geophys. Res. Lett., 43, 214–221, doi:10.1002/2015gl066854, 2016.

Nisbet, E. and Weiss, R.: Top-Down Versus Bottom-Up, Science, 328, 1241–1243, doi:10.1126/science.1189936, 2010.

Nisbet, E. G., Dlugokencky, E. J., and Bousquet, P.: Methane on the Rise—Again, Science, 343, 493–495, doi:10.1126/science.1247828, 2014.

Nisbet, E. G., Lowry, D., Zazzeri, G., Fisher, R., France, J., Brownlow, R., and Lanoisellét, M.: The use of C-isotopes in understanding the growth in atmospheric methane 2007-14, International Conference on non-CO_2 Greenhouse Gases, InGOS, Utrecht, The Netherlands, 21–24 September, 2015.

Noone, D.: Pairing Measurements of the Water Vapor Isotope Ratio with Humidity to Deduce Atmospheric Moistening and Dehydration in the Tropical Midtroposphere, J. Clim., 25, 4476–4494, doi:10.1175/jcli-d-11-00582.1, 2012.

Noone, D., Galewsky, J., Sharp, Z. D., Worden, J., Barnes, J., Baer, D., Bailey, A., Brown, D. P., Christensen, L., Crosson, E., Dong, F., Hurley, J. V., Johnson, L. R., Strong, M., Toohey, D., Van Pelt, A., and Wright, J. S.: Properties of air mass mixing and humidity in the subtropics from measurements of the D/H isotope ratio of water vapor at the Mauna Loa Observatory, J. Geophys. Res., 116, D22 113, doi:10.1029/2011jd015773, 2011.

O'Connor, F. M., Boucher, O., Gedney, N., Jones, C. D., Folberth, G. A., Coppell, R., Friedlingstein, P., Collins, W. J., Chappellaz, J., Ridley, J., and Johnson, C. E.: Possible role of wetlands, permafrost, and methane hydrates in the methane cycle under future climate change: A review, Rev. Geophys., 48, RG4005, doi:10.1029/2010rg000326, 2010.

OECD/IEA: Excerpt from Coal Information (2015 edition), IEA Publishing, available at: http://www.iea.org/statistics/topics/coal (last access: 18 December 2015), 2015.

Ostler, A., Sussmann, R., Rettinger, M., Deutscher, N. M., Dohe, S., Hase, F., Jones, N., Palm, M., and Sinnhuber, B.-M.: Multistation intercomparison of column-averaged

methane from NDACC and TCCON: impact of dynamical variability, Atmos. Meas. Tech., 7, 4081–4101, doi:10.5194/amt-7-4081-2014, 2014.

Ott, L. E., Duncan, B. N., Thompson, A. M., Diskin, G., Fasnacht, Z., Langford, A. O., Lin, M., Molod, A. M., Nielsen, J. E., Pusede, S. E., and et al.: Frequency and impact of summertime stratospheric intrusions over Maryland during DISCOVER-AQ (2011): New evidence from NASA's GEOS-5 simulations, J. Geophys. Res., 121, 3687–3706, doi:10.1002/2015jd024052, 2016.

Papayannis, A., Amiridis, V., Mona, L., Tsaknakis, G., Balis, D., Bösenberg, J., Chaikovski, A., De Tomasi, F., Grigorov, I., Mattis, I., Mitev, V., Müller, D., Nickovic, S., Pérez, C., Pietruczuk, A., Pisani, G., Ravetta, F., Rizi, V., Sicard, M., Trickl, T., Wiegner, M., Gerding, M., Mamouri, R. E., D'Amico, G., and Pappalardo, G.: Systematic lidar observations of Saharan dust over Europe in the frame of EARLINET (2000–2002), J. Geophys. Res., 113, D10 204, doi:10.1029/2007jd009028, 2008.

Parrish, D., Stohl, A., Forster, C., Atlas, E., Blake, D., Goldan, P., Kuster, W., and De Gouw, J.: Effects of mixing on evolution of hydrocarbon ratios in the troposphere, J. Geophys. Res., 112, D10S34, doi:10.1029/2006JD007583, 2007.

Patra, P., Takigawa, M., Dutton, G., Uhse, K., Ishijima, K., Lintner, B., Miyazaki, K., and Elkins, J.: Transport mechanisms for synoptic, seasonal and interannual SF_6 variations and "age" of air in troposphere, Atmos. Chem. Phys., 9, 1209–1225, doi:10.5194/acp-9-1209-2009, 2009.

Patra, P. K., Houweling, S., Krol, M., Bousquet, P., Belikov, D., Bergmann, D., Bian, H., Cameron-Smith, P., Chipperfield, M. P., Corbin, K., Fortems-Cheiney, A., Fraser, A., Gloor, E., Hess, P., Ito, A., Kawa, S. R., Law, R. M., Loh, Z., Maksyutov, S., Meng, L., Palmer, P. I., Prinn, R. G., Rigby, M., Saito, R., and Wilson, C.: TransCom model simulations of CH_4 and related species: linking transport, surface flux and chemical loss with CH_4 variability in the troposphere and lower stratosphere, Atmos. Chem. Phys., 11, 12 813–12 837, doi:10.5194/acp-11-12813-2011, 2011.

Pison, I., Ringeval, B., Bousquet, P., Prigent, C., and Papa, F.: Stable atmospheric methane in the 2000s: key-role of emissions from natural wetlands, Atmos. Chem. Phys., 13, 11 609–11 623, doi:10.5194/acp-13-11609-2013, 2013.

Pozzer, A., Pollmann, J., Taraborrelli, D., Jöckel, P., Helmig, D., Tans, P., Hueber, J., and Lelieveld, J.: Observed and simulated global distribution and budget of atmospheric C_2-C_5 alkanes, Atmos. Chem. Phys., 10, 4403–4422, doi:10.5194/acp-10-4403-2010, 2010.

Prather, M. J., Holmes, C. D., and Hsu, J.: Reactive greenhouse gas scenarios: Systematic exploration of uncertainties and the role of atmospheric chemistry, Geophys. Res. Lett., 39, L09 803, doi:10.1029/2012GL051440, 2012.

Pétron, G., Karion, A., Sweeney, C., Miller, B. R., Montzka, S. A., Frost, G. J., Trainer, M., Tans, P., Andrews, A., Kofler, J., Helmig, D., Guenther, D., Dlugokencky, E., Lang, P., Newberger, T., Wolter, S., Hall, B., Novelli, P., Brewer, A., Conley, S., Hardesty, M., Banta, R., White, A., Noone, D., Wolfe, D., and Schnell, R.: A new look at methane and nonmethane hydrocarbon emissions from oil and natural gas operations in the Colorado Denver-Julesburg Basin, J. Geophys. Res., 119, 6836–6852, doi:10.1002/2013jd021272, 2014.

Randel, W. J., Moyer, E., Park, M., Jensen, E., Bernath, P., Walker, K., and Boone, C.: Global variations of HDO and HDO/H_2O ratios in the upper troposphere and lower stratosphere derived from ACE-FTS satellite measurements, J. Geophys. Res., 117, D06 303, doi:10.1029/2011jd016632, 2012.

Ravishankara, A. R.: Heterogeneous and multiphase chemistry in the troposphere, Science, 276, 1058–1065, doi:10.1126/science.276.5315.1058, 1997.

Reichert, A., Hausmann, P., and Sussmann, R.: Pointing errors in solar absorption spectrometry – correction scheme and its validation, Atmos. Meas. Tech., 8, 3715–3728, doi:10.5194/amt-8-3715-2015, 2015.

Remsberg, E. E.: Methane as a diagnostic tracer of changes in the Brewer–Dobson circulation of the stratosphere, Atmos. Chem. Phys., 15, 3739–3754, doi:10.5194/acp-15-3739-2015, 2015.

Rice, A. L., Butenhoff, C. L., Teama, D. G., Röger, F. H., Khalil, M. A. K., and Rasmussen, R. A.: Atmospheric methane isotopic record favors fossil sources flat in 1980s and 1990s with recent increase, P. Natl. A. Sci. USA, 113, 10 791–10 796, doi:10.1073/pnas.1522923113, 2016.

Rigby, M., Prinn, R. G., Fraser, P. J., Simmonds, P. G., Langenfelds, R. L., Huang, J., Cunnold, D. M., Steele, L. P., Krummel, P. B., Weiss, R. F., O'Doherty, S., Salameh, P. K., Wang, H. J., Harth, C. M., Mühle, J., and Porter, L. W.: Renewed growth of atmospheric methane, Geophys. Res. Lett., 35, L22 805, doi:10.1029/2008GL036037, 2008.

Rinsland, C. P., Jones, N. B., Connor, B. J., Logan, J. A., Pougatchev, N. S., Goldman, A., Murcray, F. J., Stephen, T. M., Pine, A. S., Zander, R., Mahieu, E., and Demoulin, P.: Northern and Southern hemisphere ground-based infrared spectroscopic measurements of tropospheric carbon monoxide and ethane, J. Geophys. Res., 103, 28 197–28 217, doi:10.1029/98JD02515, 1998.

Rinsland, C. P., Meier, A., Griffith, D. W., and Chiou, L. S.: Ground-based measurements of tropospheric CO, C_2H_6, and HCN from Australia at 34° S latitude during 1997–1998, J. Geophys. Res., 106, 20 913–20 924, doi:10.1029/2000JD000318, 2001.

Risi, C., Noone, D., Worden, J., Frankenberg, C., Stiller, G., Kiefer, M., Funke, B., Walker, K., Bernath, P., Schneider, M., Wunch, D., Sherlock, V., Deutscher, N., Griffith, D., Wennberg, P. O., Strong, K., Smale, D., Mahieu, E., Barthlott, S., Hase, F., García, O., Notholt, J., Warneke, T., Toon, G., Sayres, D., Bony, S., Lee, J., Brown, D., Uemura, R., and Sturm, C.: Process-evaluation of tropospheric humidity simulated by general circulation models using water vapor isotopologues: 1. Comparison between models and observations, J. Geophys. Res., 117, D05 303, doi:10.1029/2011jd016621, 2012.

Rodgers, C. D.: Retrieval of atmospheric temperature and composition from remote measurements of thermal radiation, Rev. Geophys., 14, 609–624, doi:10.1029/rg014i004p00609, 1976.

Rodgers, C. D.: Characterization and error analysis of profiles retrieved from remote sounding measurements, J. Geophys. Res., 95, 5587–5595, doi:10.1029/JD095iD05p05587, 1990.

Rodgers, C. D.: Characterization and Error Analysis of Profiles Retrieved From Remote

Sounding Measurements, vol. 2 of *Series on Atmospheric, Oceanic and Planetary Physics*, World Scientific Publishing, London, UK, 2000.

Rothman, L., Barbe, A., Chris Benner, D., Brown, L., Camy-Peyret, C., Carleer, M., Chance, K., Clerbaux, C., Dana, V., Devi, V., Fayt, A., Flaud, J.-M., Gamache, R. R., Goldman, A., Jacquemart, D., Jucks, K. W., Lafferty, W. J., Mandin, J.-Y., Massie, S. T., Nemtchinov, V., Newnham, D. A., Perrin, A., Rinsland, C. P., Schroeder, J., Smith, K. M., Smith, M. A. H., Tang, K., Toth, R. A., Vander Auwera, J., Varanasi, P., and Yoshino, K.: The HITRAN molecular spectroscopic database: edition of 2000 including updates through 2001, J. Quant. Spectrosc. Ra., 82, 5–44, doi:10.1016/s0022-4073(03)00146-8, 2003.

Rothman, L., Gordon, I., Babikov, Y., Barbe, A., Chris Benner, D., Bernath, P., Birk, M., Bizzocchi, L., Boudon, V., Brown, L. R., Campargue, A., Chance, K., Cohen, E., Coudert, L., Devi, V., Drouin, B., Fayt, A., Flaud, J.-M., Gamache, R., Harrison, J., Hartmann, J.-M., Hill, C., Hodges, J., Jacquemart, D., Jolly, A., Lamouroux, J., Roy, R. L., Li, G., Long, D., Lyulin, O., Mackie, C., Massie, S., Mikhailenko, S., Müller, H., Naumenko, O., Nikitin, A., Orphal, J., Perevalov, V., Perrin, A., Polovtseva, E., Richard, C., Smith, M., Starikova, E., Sung, K., Tashkun, S., Tennyson, J., Toon, G., Tyuterev, V., and Wagner, G.: The HITRAN2012 molecular spectroscopic database, J. Quant. Spectrosc. Ra., 130, 4–50, doi:10.1016/j.jqsrt.2013.07.002, 2013.

Rudolph, J.: The tropospheric distribution and budget of ethane, J. Geophys. Res., 100, 11 369–11 381, doi:10.1029/95JD00693, 1995.

Saito, R., Patra, P. K., Deutscher, N., Wunch, D., Ishijima, K., Sherlock, V., Blumenstock, T., Dohe, S., Griffith, D., Hase, F., Heikkinen, P., Kyrö, E., Macatangay, R., Mendonca, J., Messerschmidt, J., Morino, I., Notholt, J., Rettinger, M., Strong, K., Sussmann, R., and Warneke, T.: Technical Note: Latitude-time variations of atmospheric column-average dry air mole fractions of CO_2, CH_4 and N_2O, Atmos. Chem. Phys., 12, 7767–7777, doi:10.5194/acp-12-7767-2012, 2012.

Sander, S. P., Abbatt, J., Barker, J. R., Burkholder, J. B., Friedl, R. R., Golden, D. M., Huie, R. E., Kolb, C. E., Kurylo, M. J., Moortgat, G. K., Orkin, V. L., and Wine, P. H.: Chemical Kinetics and Photochemical Data for Use in Atmospheric Studies, Evaluation No. 17, JPL Publication 10-6, Jet Propulsion Laboratory, Pasadena, USA, available at: http://jpldataeval.jpl.nasa.gov (last access: 18 December 2015), 2011.

Schaefer, H., Fletcher, S. E. M., Veidt, C., Lassey, K. R., Brailsford, G. W., Bromley, T. M., Dlugokencky, E. J., Michel, S. E., Miller, J. B., Levin, I., Lowe, D. C., Martin, R. J., Vaughn, B. H., and White, J. W. C.: A 21st-century shift from fossil-fuel to biogenic methane emissions indicated by $^{13}CH_4$, Science, 352, 80–84, doi:10.1126/science.aad2705, 2016.

Scheepmaker, R. A., Frankenberg, C., Deutscher, N. M., Schneider, M., Barthlott, S., Blumenstock, T., Garcia, O. E., Hase, F., Jones, N., Mahieu, E., Notholt, J., Velazco, V., Landgraf, J., and Aben, I.: Validation of SCIAMACHY HDO/H_2O measurements using the TCCON and NDACC-MUSICA networks, Atmos. Meas. Tech., 8, 1799–1818, doi:10.5194/amt-8-1799-2015, 2015.

Schneider, M. and Hase, F.: Optimal estimation of tropospheric H_2O and δD with

IASI/METOP, Atmos. Chem. Phys., 11, 11 207–11 220, doi:10.5194/acp-11-11207-2011, 2011.

Schneider, M., Barthlott, S., Hase, F., González, Y., Yoshimura, K., García, O. E., Sepúlveda, E., Gomez-Pelaez, A., Gisi, M., Kohlhepp, R., Dohe, S., Blumenstock, T., Wiegele, A., Christner, E., Strong, K., Weaver, D., Palm, M., Deutscher, N. M., Warneke, T., Notholt, J., Lejeune, B., Demoulin, P., Jones, N., Griffith, D. W. T., Smale, D., and Robinson, J.: Ground-based remote sensing of tropospheric water vapour isotopologues within the project MUSICA, Atmos. Meas. Tech., 5, 3007–3027, doi:10.5194/amt-5-3007-2012, 2012.

Schneider, M., Demoulin, P., Sussmann, R., and Notholt, J.: Fourier Transform Infrared Spectrometry, in: Monitoring Atmospheric Water Vapour, edited by Kämpfer, N., vol. 10 of *ISSI Scientific Report Series*, pp. 95–111, Springer, New York, USA, doi: 10.1007/978-1-4614-3909-7_6, 2013.

Schneider, M., González, Y., Dyroff, C., Christner, E., Wiegele, A., Barthlott, S., García, O. E., Sepúlveda, E., Hase, F., Andrey, J., Blumenstock, T., Guirado, C., Ramos, R., and Rodríguez, S.: Empirical validation and proof of added value of MUSICA's tropospheric δD remote sensing products, Atmos. Meas. Tech., 8, 483–503, doi:10.5194/amt-8-483-2015, 2015.

Schneider, M., Wiegele, A., Barthlott, S., González, Y., Christner, E., Dyroff, C., García, O. E., Hase, F., Blumenstock, T., Sepúlveda, E., Mengistu Tsidu, G., Takele Kenea, S., Rodríguez, S., and Andrey, J.: Accomplishments of the MUSICA project to provide accurate, long-term, global and high-resolution observations of tropospheric $\{H_2O,\delta D\}$ pairs – a review, Atmos. Meas. Tech., 9, 2845–2875, doi:10.5194/amt-9-2845-2016, 2016.

Schneider, T., O'Gorman, P. A., and Levine, X. J.: Water vapor and the dynamics of climate change, Rev. Geophys., 48, RG3001, doi:10.1029/2009rg000302, 2010.

Schneising, O., Burrows, J. P., Dickerson, R. R., Buchwitz, M., Reuter, M., and Bovensmann, H.: Remote sensing of fugitive methane emissions from oil and gas production in North American tight geologic formations, Earth's Future, 2, 548–558, doi: 10.1002/2014EF000265, 2014.

Schoell, M.: The hydrogen and carbon isotopic composition of methane from natural gases of various origins, Geochim. Cosmochim. Acta, 44, 649–661, doi:10.1016/0016-7037(80) 90155-6, 1980.

Schuepbach, E., D. Davies, T., Massacand, A. C., and Wernli, H.: Mesoscale modelling of vertical atmospheric transport in the Alps associated with the advection of a tropopause fold – a winter ozone episode, Atmos. Environ., 33, 3613–3626, doi:10.1016/s1352-2310(99) 00103-x, 1999.

Schuur, E. A. G., McGuire, A. D., Schädel, C., Grosse, G., Harden, J. W., Hayes, D. J., Hugelius, G., Koven, C. D., Kuhry, P., Lawrence, D. M., Natali, S. M., Olefeldt, D., Romanovsky, V. E., Schaefer, K., Turetsky, M. R., Treat, C. C., and Vonk, J. E.: Climate change and the permafrost carbon feedback, Nature, 520, 171–179, doi:10.1038/ nature14338, 2015.

Schwietzke, S., Griffin, W. M., Matthews, H. S., and Bruhwiler, L. M. P.: Global Bottom-Up Fossil Fuel Fugitive Methane and Ethane Emissions Inventory for Atmospheric Modeling, ACS Sustain. Chem. Eng., 2, 1992–2001, doi:10.1021/sc500163h, 2014.

Simmonds, P. G., Manning, A. J., Derwent, R. G., Ciais, P., Ramonet, M., Kazan, V., and Ryall, D.: A burning question. Can recent growth rate anomalies in the greenhouse gases be attributed to large-scale biomass burning events?, Atmos. Environ., 39, 2513–2517, doi:10.1016/j.atmosenv.2005.02.018, 2005.

Simmons, A., Fellous, J.-L., Ramaswamy, V., Trenberth, K., Asrar, G., Balmaseda, M., Burrows, J. P., Ciais, P., Drinkwater, M., Friedlingstein, P., Gobron, N., Guilyardi, E., Halpern, D., Heimann, M., Johannessen, J., Levelt, P. F., Lopez-Baeza, E., Penner, J., Scholes, R., and Shepherd, T.: Observation and integrated Earth-system science: A roadmap for 2016–2025, Adv. Space Res., 57, 2037–2103, doi:10.1016/j.asr.2016.03.008, 2016.

Simpson, I. J., Chen, T.-Y., Blake, D. R., and Rowland, F. S.: Implications of the recent fluctuations in the growth rate of tropospheric methane, Geophys. Res. Lett., 29, 1479, doi:10.1029/2001GL014521, 2002.

Simpson, I. J., Rowland, F. S., Meinardi, S., and Blake, D. R.: Influence of biomass burning during recent fluctuations in the slow growth of global tropospheric methane, Geophys. Res. Lett., 33, L22 808, doi:10.1029/2006gl027330, 2006.

Simpson, I. J., Sulbaek Andersen, M. P., Meinardi, S., Bruhwiler, L., Blake, N. J., Helmig, D., Rowland, F. S., and Blake, D. R.: Long-term decline of global atmospheric ethane concentrations and implications for methane, Nature, 488, 490–494, doi:10.1038/nature11342, 2012.

Škerlak, B., Sprenger, M., and Wernli, H.: A global climatology of stratosphere–troposphere exchange using the ERA-Interim data set from 1979 to 2011, Atmos. Chem. Phys., 14, 913–937, doi:10.5194/acp-14-913-2014, 2014.

Solomon, S., Rosenlof, K. H., Portmann, R. W., Daniel, J. S., Davis, S. M., Sanford, T. J., and Plattner, G.-K.: Contributions of Stratospheric Water Vapor to Decadal Changes in the Rate of Global Warming, Science, 327, 1219–1223, doi:10.1126/science.1182488, 2010.

Staudt, A. C., Jacob, D. J., Logan, J. A., Bachiochi, D., Krishnamurti, T. N., and Poisson, N.: Global chemical model analysis of biomass burning and lightning influences over the South Pacific in austral spring, J. Geophys. Res., 107, ACH 11–1–ACH 11–17, doi:10.1029/2000jd000296, 2002.

Steck, T.: Methods for determining regularization for atmospheric retrieval problems, Appl. Opt., 41, 1788–1797, doi:10.1364/AO.41.001788, 2002.

Stein, A. F., Draxler, R. R., Rolph, G. D., Stunder, B. J. B., Cohen, M. D., and Ngan, F.: NOAA's HYSPLIT Atmospheric Transport and Dispersion Modeling System, B. Am. Meteorol. Soc., 96, 2059–2077, doi:10.1175/bams-d-14-00110.1, 2015.

Steinwagner, J., Fueglistaler, S., Stiller, G., von Clarmann, T., Kiefer, M., Borsboom, P.-P., van Delden, A., and Röckmann, T.: Tropical dehydration processes constrained by the seasonality of stratospheric deuterated water, Nat. Geosci., 3, 262–266, doi:10.1038/ngeo822, 2010.

Stephens, G. L., Li, J., Wild, M., Clayson, C. A., Loeb, N., Kato, S., L'Ecuyer, T., Stackhouse, P. W., Lebsock, M., and Andrews, T.: An update on Earth's energy balance

in light of the latest global observations, Nat. Geosci., 5, 691–696, doi:10.1038/ngeo1580, 2012.

Stohl, A.: Computation, accuracy and applications of trajectories–a review and bibliography, Atmos. Environ., 32, 947–966, doi:10.1016/S1352-2310(97)00457-3, 1998.

Stohl, A.: A 1-year Lagrangian "climatology" of airstreams in the northern hemisphere troposphere and lowermost stratosphere, J. Geophys. Res., 106, 7263–7279, doi:10.1029/2000jd900570, 2001.

Stohl, A. and Trickl, T.: A textbook example of long-range transport: Simultaneous observation of ozone maxima of stratospheric and North American origin in the free troposphere over Europe, J. Geophys. Res., 104, 30 445–30 462, doi:10.1029/1999JD900803, 1999.

Stohl, A., Spichtinger-Rakowsky, N., Bonasoni, P., Feldmann, H., Memmesheimer, M., Scheel, H., Trickl, T., Hübener, S., Ringer, W., and Mandl, M.: The influence of stratospheric intrusions on alpine ozone concentrations, Atmos. Environ., 34, 1323–1354, doi:10.1016/s1352-2310(99)00320-9, 2000.

Stohl, A., Eckhardt, S., Forster, C., James, P., and Spichtinger, N.: On the pathways and timescales of intercontinental air pollution transport, J. Geophys. Res., 107, 4684, doi:10.1029/2001jd001396, 2002.

Stohl, A., Bonasoni, P., Cristofanelli, P., Collins, W., Feichter, J., Frank, A., Forster, C., Gerasopoulos, E., Gäggeler, H., James, P., and Kentarchos, T.: Stratosphere-troposphere exchange: A review, and what we have learned from STACCATO, J. Geophys. Res., 108, 8516, doi:10.1029/2002jd002490, 2003.

Strong, M., Sharp, Z. D., and Gutzler, D. S.: Diagnosing moisture transport using D/H ratios of water vapor, Geophys. Res. Lett., 34, L03 404, doi:10.1029/2006gl028307, 2007.

Sussmann, R. and Schäfer, K.: Infrared spectroscopy of tropospheric trace gases: combined analysis of horizontal and vertical column abundances, Appl. Opt., 36, 735–741, doi:10.1364/AO.36.000735, 1997.

Sussmann, R., Borsdorff, T., Rettinger, M., Camy-Peyret, C., Demoulin, P., Duchatelet, P., Mahieu, E., and Servais, C.: Technical Note: Harmonized retrieval of column-integrated atmospheric water vapor from the FTIR network – first examples for long-term records and station trends, Atmos. Chem. Phys., 9, 8987–8999, doi:10.5194/acp-9-8987-2009, 2009.

Sussmann, R., Forster, F., Rettinger, M., and Jones, N.: Strategy for high-accuracy-and-precision retrieval of atmospheric methane from the mid-infrared FTIR network, Atmos. Meas. Tech., 4, 1943–1964, doi:10.5194/amt-4-1943-2011, 2011.

Sussmann, R., Forster, F., Rettinger, M., and Bousquet, P.: Renewed methane increase for five years (2007–2011) observed by solar FTIR spectrometry, Atmos. Chem. Phys., 12, 4885–4891, doi:10.5194/acp-12-4885-2012, 2012.

Sussmann, R., Ostler, A., Forster, F., Rettinger, M., Deutscher, N. M., Griffith, D. W. T., Hannigan, J. W., Jones, N., and Patra, P. K.: First intercalibration of column-averaged methane from the Total Carbon Column Observing Network and the Network for the

Detection of Atmospheric Composition Change, Atmos. Meas. Tech., 6, 397–418, doi: 10.5194/amt-6-397-2013, 2013.

Sutanto, S. J., Hoffmann, G., Scheepmaker, R. A., Worden, J., Houweling, S., Yoshimura, K., Aben, I., and Röckmann, T.: Global-scale remote sensing of water isotopologues in the troposphere: representation of first-order isotope effects, Atmos. Meas. Tech., 8, 999–1019, doi:10.5194/amt-8-999-2015, 2015.

Tans, P. P.: A note on isotopic ratios and the global atmospheric methane budget, Glob. Biogeochem. Cycles, 11, 77–81, doi:10.1029/96GB03940, 1997.

Taylor, S. W., Sherwood Lollar, B., and Wassenaar, I.: Bacteriogenic Ethane in Near-Surface Aquifers: Implications for Leaking Hydrocarbon Well Bores, Environ. Sci. Technol., 34, 4727–4732, doi:10.1021/es001066x, 2000.

TF-HTAP (Task Force on Hemispheric Transport of Air Pollution): Hemispheric Transport of Air Pollution 2010, Part A: Ozone and Particulate Matter, Air Pollution Studies No. 17, edited by: Dentener, F., Keating, T., and Akimoto, H., United Nations, Geneva, Switzerland, 2010.

Tikhonov, A.: On the solution of incorrectly stated problems and a method of regularization, Dokl. Acad. Nauk SSSR, 151, 501–504, 1963.

Trickl, T., Cooper, O. R., Eisele, H., James, P., Mücke, R., and Stohl, A.: Intercontinental transport and its influence on the ozone concentrations over central Europe: Three case studies, J. Geophys. Res., 108, 8530, doi:10.1029/2002jd002735, 2003.

Trickl, T., Feldmann, H., Kanter, H.-J., Scheel, H.-E., Sprenger, M., Stohl, A., and Wernli, H.: Forecasted deep stratospheric intrusions over Central Europe: case studies and climatologies, Atmos. Chem. Phys., 10, 499–524, doi:10.5194/acp-10-499-2010, 2010.

Trickl, T., Bärtsch-Ritter, N., Eisele, H., Furger, M., Mücke, R., Sprenger, M., and Stohl, A.: High-ozone layers in the middle and upper troposphere above Central Europe: potential import from the stratosphere along the subtropical jet stream, Atmos. Chem. Phys., 11, 9343–9366, doi:10.5194/acp-11-9343-2011, 2011.

Trickl, T., Giehl, H., Jäger, H., and Vogelmann, H.: 35 yr of stratospheric aerosol measurements at Garmisch-Partenkirchen: from Fuego to Eyjafjallajökull, and beyond, Atmos. Chem. Phys., 13, 5205–5225, doi:10.5194/acp-13-5205-2013, 2013.

Trickl, T., Vogelmann, H., Giehl, H., Scheel, H.-E., Sprenger, M., and Stohl, A.: How stratospheric are deep stratospheric intrusions?, Atmos. Chem. Phys., 14, 9941–9961, doi:10.5194/acp-14-9941-2014, 2014.

Trickl, T., Vogelmann, H., Flentje, H., and Ries, L.: Stratospheric ozone in boreal fire plumes – the 2013 smoke season over central Europe, Atmos. Chem. Phys., 15, 9631–9649, doi:10.5194/acp-15-9631-2015, 2015.

Trickl, T., Vogelmann, H., Fix, A., Schäfler, A., Wirth, M., Calpini, B., Levrat, G., Romanens, G., Apituley, A., Wilson, K. M., Begbie, R., Reichardt, J., Vömel, H., and Sprenger, M.: How stratospheric are deep stratospheric intrusions? LUAMI 2008, Atmos. Chem. Phys., 16, 8791–8815, doi:10.5194/acp-16-8791-2016, 2016.

Turner, A. J., Jacob, D. J., Wecht, K. J., Maasakkers, J. D., Lundgren, E., Andrews, A. E., Biraud, S. C., Boesch, H., Bowman, K. W., Deutscher, N. M., Dubey, M. K., Griffith, D. W. T., Hase, F., Kuze, A., Notholt, J., Ohyama, H., Parker, R., Payne, V. H., Sussmann, R., Sweeney, C., Velazco, V. A., Warneke, T., Wennberg, P. O., and Wunch, D.: Estimating global and North American methane emissions with high spatial resolution using GOSAT satellite data, Atmos. Chem. Phys., 15, 7049–7069, doi:10.5194/acp-15-7049-2015, 2015.

Turner, A. J., Jacob, D. J., Benmergui, J., Wofsy, S. C., Maasakkers, J. D., Butz, A., Hasekamp, O., and Biraud, S. C.: A large increase in U.S. methane emissions over the past decade inferred from satellite data and surface observations, Geophys. Res. Lett., 43, 2218–2224, doi:10.1002/2016gl067987, 2016.

UNFCCC (United Nations Framework Convention on Climate Change): Status of the Doha Amendment, available at: http://unfccc.int/kyoto_protocol/doha_amendment/items/7362.php (last access: 22 September 2016), 2016.

US Energy Information Administration: Annual Energy Outlook 2014, DOE/EIA-0383(2014), Washington DC, 2014.

US Energy Information Administration: International Energy Statistics, available at: http://www.eia.gov/cfapps/ipdbproject (last access: 19 October 2015), 2015.

van der Werf, G. R., Randerson, J. T., Giglio, L., Collatz, G. J., Mu, M., Kasibhatla, P. S., Morton, D. C., DeFries, R. S., Jin, Y., and van Leeuwen, T. T.: Global fire emissions and the contribution of deforestation, savanna, forest, agricultural, and peat fires (1997–2009), Atmos. Chem. Phys., 10, 11 707–11 735, doi:10.5194/acp-10-11707-2010, 2010.

Vigouroux, C., Stavrakou, T., Whaley, C., Dils, B., Duflot, V., Hermans, C., Kumps, N., Metzger, J.-M., Scolas, F., Vanhaelewyn, G., Müller, J.-F., Jones, D. B. A., Li, Q., and De Mazière, M.: FTIR time-series of biomass burning products (HCN, C_2H_6, C_2H_2, CH_3OH, and HCOOH) at Reunion Island (21°S, 55°E) and comparisons with model data, Atmos. Chem. Phys., 12, 10 367–10 385, doi:10.5194/acp-12-10367-2012, 2012.

Vinciguerra, T., Yao, S., Dadzie, J., Chittams, A., Deskins, T., Ehrman, S., and Dickerson, R. R.: Regional air quality impacts of hydraulic fracturing and shale natural gas activity: Evidence from ambient VOC observations, Atmos. Environ., 110, 144–150, doi:10.1016/j.atmosenv.2015.03.056, 2015.

Vogelmann, H., Sussmann, R., Trickl, T., and Reichert, A.: Spatiotemporal variability of water vapor investigated using lidar and FTIR vertical soundings above the Zugspitze, Atmos. Chem. Phys., 15, 3135–3148, doi:10.5194/acp-15-3135-2015, 2015.

Wallace, J. M. and Hobbs, P. V.: Atmospheric Science: An Introductory Survey, vol. 92 of *International Geophysics Series*, Elsevier, London, UK, 2nd edn., 2006.

Wang, Q., Chen, X., Jha, A. N., and Rogers, H.: Natural gas from shale formation – The evolution, evidences and challenges of shale gas revolution in United States, Renew. Sustain. Energy Rev., 30, 1–28, doi:10.1016/j.rser.2013.08.065, 2014.

Wang, Y. and Zeng, T.: On tracer correlations in the troposphere: The case of ethane and propane, J. Geophys. Res., 109, D24 306, doi:10.1029/2004JD005023, 2004.

Wennberg, P. O., Mui, W., Wunch, D., Kort, E. A., Blake, D. R., Atlas, E. L., Santoni, G. W., Wofsy, S. C., Diskin, G. S., Jeong, S., and Fischer, M. L.: On the Sources of Methane to the Los Angeles Atmosphere, Environ. Sci. Technol., 46, 9282–9289, doi:10.1021/es301138y, 2012.

Wiegele, A., Schneider, M., Hase, F., Barthlott, S., García, O. E., Sepúlveda, E., González, Y., Blumenstock, T., Raffalski, U., Gisi, M., and Kohlhepp, R.: The MUSICA MetOp/IASI H_2O and δD products: characterisation and long-term comparison to NDACC/FTIR data, Atmos. Meas. Tech., 7, 2719–2732, doi:10.5194/amt-7-2719-2014, 2014.

Wild, M., Folini, D., Schär, C., Loeb, N., Dutton, E. G., and König-Langlo, G.: The global energy balance from a surface perspective, Clim. Dyn., 40, 3107–3134, doi:10.1007/s00382-012-1569-8, 2013.

Williams, J. and Koppmann, R.: Volatile Organic Compounds in the Atmosphere: An Overview, in: Volatile Organic Compounds in the Atmosphere, edited by Koppmann, R., pp. 1–32, Blackwell Publishing, Oxford, UK, 2007.

Worden, J., Bowman, K., Noone, D., Beer, R., Clough, S., Eldering, A., Fisher, B., Goldman, A., Gunson, M., Herman, R., Kulawik, S. S., Lampel, M., Luo, M., Osterman, G., Rinsland, C., Rodgers, C., Sander, S., Shephard, M., and Worden, H.: Tropospheric Emission Spectrometer observations of the tropospheric HDO/H_2O ratio: Estimation approach and characterization, J. Geophys. Res., 111, D16 309, doi:10.1029/2005jd006606, 2006.

Worden, J., Noone, D., Bowman, K., Beer, R., Eldering, A., Fisher, B., Gunson, M., Goldman, A., Herman, R., Kulawik, S. S., Lampel, M., Osterman, G., Rinsland, C., Rodgers, C., Sander, S., Shephard, M., Webster, C. R., and Worden, H.: Importance of rain evaporation and continental convection in the tropical water cycle, Nature, 445, 528–532, doi:10.1038/nature05508, 2007.

Wotawa, G., Novelli, P. C., Trainer, M., and Granier, C.: Inter-annual variability of summertime CO concentrations in the Northern Hemisphere explained by boreal forest fires in North America and Russia, Geophys. Res. Lett., 28, 4575–4578, doi:10.1029/2001gl013686, 2001.

Wunch, D., Toon, G. C., Blavier, J.-F. L., Washenfelder, R. A., Notholt, J., Connor, B. J., Griffith, D. W. T., Sherlock, V., and Wennberg, P. O.: The Total Carbon Column Observing Network, Philos. T. Roy. Soc. A, 369, 2087–2112, doi:10.1098/rsta.2010.0240, 2011.

Xiao, Y., Logan, J. A., Jacob, D. J., Hudman, R. C., Yantosca, R., and Blake, D. R.: Global budget of ethane and regional constraints on U.S. sources, J. Geophys. Res., 113, D21 306, doi:10.1029/2007jd009415, 2008.

Yacovitch, T. I., Herndon, S. C., Roscioli, J. R., Floerchinger, C., McGovern, R. M., Agnese, M., Pétron, G., Kofler, J., Sweeney, C., Karion, A., Conley, S. A., Kort, E. A., Nähle, L., Fischer, M., Hildebrandt, L., Koeth, J., McManus, J. B., Nelson, D. D., Zahniser, M. S., and Kolb, C. E.: Demonstration of an Ethane Spectrometer for Methane Source Identification, Environ. Sci. Technol., 48, 8028–8034, doi:10.1021/es501475q, 2014.

Yokelson, R. J., Andreae, M. O., and Akagi, S.: Pitfalls with the use of enhancement ratios or normalized excess mixing ratios measured in plumes to characterize pollution sources and aging, Atmos. Meas. Tech., 6, 2155, doi:10.5194/amt-6-2155-2013, 2013.

Zahn, A., Franz, P., Bechtel, C., Grooß, J.-U., and Röckmann, T.: Modelling the budget of middle atmospheric water vapour isotopes, Atmos. Chem. Phys., 6, 2073–2090, doi:10.5194/acp-6-2073-2006, 2006.

Zahn, A., Christner, E., van Velthoven, P. F. J., Rauthe-Schöch, A., and Brenninkmeijer, C. A. M.: Processes controlling water vapor in the upper troposphere/lowermost stratosphere: An analysis of 8 years of monthly measurements by the IAGOS-CARIBIC observatory, J. Geophys. Res. Atmos., 119, 11,505–11,525, doi:10.1002/2014jd021687, 2014.

Zdunkowski, W., Trautmann, T., and Bott, A.: Radiation in the atmosphere: a course in theoretical meteorology, Cambridge University Press, Cambridge, UK, 2007.

Zeng, G., Wood, S. W., Morgenstern, O., Jones, N. B., Robinson, J., and Smale, D.: Trends and variations in CO, C_2H_6, and HCN in the Southern Hemisphere point to the declining anthropogenic emissions of CO and C_2H_6, Atmos. Chem. Phys., 12, 7543–7555, doi:10.5194/acp-12-7543-2012, 2012.

Glossary

DOFS	Degrees of freedom for signal
DSTI	Deep stratospheric intrusion
EMR	Ethane-to-methane ratio
FTIR	Fourier transform infrared
GFED	Global Fire Emission Database (Giglio et al., 2013)
HITRAN	High-resolution transmission molecular absorption database (Rothman et al., 2013)
HYSPLIT	Hybrid Single-Particle Lagrangian Integrated Trajectory model (Stein et al., 2015)
IHG	Interhemispheric gradient
ILS	Instrumental line shape
IPCC	Intergovernmental Panel on Climate Change (IPCC, 2013)
IWV	Integrated water vapor
LC	Last condensation point
MUSICA	MUlti-platform remote Sensing of Isotopologues for investigating the Cycle of Atmospheric water (Schneider et al., 2012)
NCEP	National Center for Environmental Prediction
NDACC	Network for the Detection of Atmospheric Composition Change (www.ndacc.org)
OPD	Optical path difference
PROFFIT	PROFile Fit (retrieval code; Hase et al., 2004)
RH	Relative humidity

RMS	Root-mean-square residual
SD	Standard deviation
SE	Standard error of the mean
STI	Stratospheric intrusion
sza	Solar zenith angle
TCCON	Total Carbon Column Observing Network (Wunch et al., 2011)
TNA	Intercontinental transport from Northern Africa
toa	Top of atmosphere
TP	Tropopause
TUS	Intercontinental transport from North America (US)
VMR	Volume mixing ratio
WACCM	Whole Atmosphere Community Climate Model (García et al., 2007)
WCB	Warm conveyor belt
XCH_4	Column-averaged dry-air mole fraction of methane
XC_2H_6	Column-averaged dry-air mole fraction of ethane

Publications Petra Hausmann

Peer-Reviewed Journal Publications

Hausmann, P., Sussmann, R., Trickl, T., and Schneider, M.: A decadal time series of water vapor and D/H isotope ratios above Zugspitze: transport patterns to central Europe, Atmos. Chem. Phys., 17, 7635–7651, doi:10.5194/acp-17-7635-2017, 2017.

Bader, W., Bovy, B., Conway, S., Strong, K., Smale, D., Turner, A. J., Blumenstock, T., Boone, C., Collaud Coen, M., Coulon, A., Garcia, O., Griffith, D. W. T., Hase, F., **Hausmann, P.**, Jones, N., Krummel, P., Murata, I., Morino, I., Nakajima, H., O'Doherty, S., Paton-Walsh, C., Robinson, J., Sandrin, R., Schneider, M., Servais, C., Sussmann, R., and Mahieu, E.: The recent increase of atmospheric methane from 10 years of ground-based NDACC FTIR observations since 2005, Atmos. Chem. Phys., 17, 2255–2277, doi:10.5194/acp-17-2255-2017, 2017.

Hausmann, P., Sussmann, R., and Smale, D.: Contribution of oil and natural gas production to renewed increase in atmospheric methane (2007–2014): top–down estimate from ethane and methane column observations, Atmos. Chem. Phys., 16, 3227–3244, doi:10.5194/acp-16-3227-2016, 2016.

Zinner, T., **Hausmann, P**., Ewald, F., Bugliaro, L., Emde, C., and Mayer, B.: Ground-based imaging remote sensing of ice clouds: uncertainties caused by sensor, method and atmosphere, Atmos. Meas. Tech., 9, 4615–4632, doi:10.5194/amt-9-4615-2016, 2016.

Reichert, A., **Hausmann, P.**, and Sussmann, R.: Pointing errors in solar absorption spectrometry – correction scheme and its validation, Atmos. Meas. Tech., 8, 3715–3728, doi:10.5194/amt-8-3715-2015, 2015.

Contributions to International Conferences

Hausmann, P., Sussmann, R., and Smale, D.: Renewed methane increase (2007–2014): contribution of oil and natural gas emissions determined from methane and ethane column observations, Geophysical Research Abstracts Vol. 18, EGU2016-14439, 2016.

Sussmann, R., Ostler, A., and **Hausmann, P.**: Retrieval of methane columns and profiles from mid-infrared FTIR spectrometry and intercalibration to TCCON, International Conference on non-CO_2 Greenhouse Gases, InGOS, Utrecht, The Netherlands, 21–24 September, 2015.

Hausmann, P., Sussmann, R., and Smale, D.: New insight into renewed methane increase: constraints by long-term evolution of ethane interhemispheric gradients, Int. Joint Workshop of the NDACC Infrared Working Group and the TCCON Science Team, Toronto, Canada, 8–12 June, 2015.

Reichert, A., **Hausmann, P.**, and Sussmann, R.: Determination and correction of pointing errors in solar FTIR spectrometry, Int. Joint Workshop of the NDACC Infrared Working Group and the TCCON Science Team, Toronto, Canada, 8–12 June, 2015.

Hausmann, P. and Sussmann, R.: Retrieval of atmospheric methane from mid-infrared FTIR spectrometry optimized for profile information content and minimal cross-sensitivity to water vapor, Verhandl. DPG (VI) 50, UP2.12, 2015.

Sussmann, R., Rettinger, M., **Hausmann, P.**, Ostler, A., and Reichert, A.: Garmisch (TCCON) and Zugspitze (NDACC) site news, Int. Joint Workshop of the NDACC Infrared Working Group and the TCCON Science Team, Bad Sulza, Germany, 12–15 May, 2014.

Hausmann, P., Zinner, T., Emde, C., and Mayer, B.: Ground-based remote sensing of optically thin ice clouds, International Radiation Symposium, Berlin, Germany, IRS2012-384, 2012.

Acknowledgments

First of all, I would like to thank my supervisor PD Dr. Ralf Sussmann for offering me the opportunity to work on this exciting topic in his working group. Beside an excellent technical infrastructure he provided during my time as doctoral candidate, I could substantially benefit from his guidance and expertise in establishing collaborations, preparing scientific publications, as well as contributing to international conferences. His constant support, enthusiasm, and commitment significantly contributed to this work. In critical and fruitful discussions important ideas and new challenges evolved which always took my investigations a step forward.

Likewise, I would like to thank Prof. Dr. Jucundus Jacobeit for welcoming me at Augsburg University and for his kind assistance in all academic matters regarding my dissertation and grant application. Moreover, I am very grateful for his willingness to review this thesis as co-examiner.

Furthermore, I appreciate the friendly reception by Prof. Dr. Hans Peter Schmid at KIT/IMK-IFU in Garmisch-Partenkirchen. In addition, I would like to thank Prof. Dr. Harald Kunstmann for his assistance and positive encouragement.

My special thanks go to the whole working group "Atmospheric Variability and Trends" at KIT/IMK-IFU for the friendly and motivating working atmosphere. Especially, I thank Markus Rettinger for his competent and unhesitating help in technical issues but also for his good company while sharing an office with me. I would also like to thank Andreas Reichert, Thomas Trickl, and Andreas Ostler for the excellent cooperation and their readiness to help with any question I came up with. Furthermore, I very much appreciate excellent support by Frank Hase and Matthias Schneider at KIT/IMK-ASF. Likewise, I would like to thank Dan Smale (NIWA) for his helpfulness and our good collaboration. This dissertation was funded by the Bavarian State Ministry of the Environment and Consumer Protection (contracts TLK01U-49581 and VAO-II TP I/01), which is gratefully acknowledged.

I am going to miss all the good conversations with Elisabeth Eckart and Janina Klatt who accompanied me through the ups and downs during the last years. I very much appreciate their friendship. Also, I want to thank Elija and Conni for the good times we spent together. I enjoyed discussing with you and pushing our ideas forward. Moreover, I would like to thank all members of our IFU band – Stefanie Vogl, Hannes Vogelmann, Johannes Werhahn, and Joachim Fallmann – for playing good music together and getting my mind free.

Finally, I would like to thank my dear mother for her love and for teaching me to believe in myself and my qualities. My deepest gratitude goes to my partner Frank who was always willing to listen, found the right words of encouragement, and gave me the strength to successfully finish this work.